Kagome and honeycomb flat bands in moiré graphene

Michael G. Scheer● and Biao Lian●

Department of Physics, Princeton University, Princeton, New Jersey 08544, USA

We propose a class of graphene-based moiré systems hosting flat bands on kagome and honeycomb moiré superlattices. These systems are formed by stacking a graphene layer on a 2D substrate with lattice constant approximately $\sqrt{3}$ times that of graphene. When the moiré potentials are induced by a 2D irreducible corepresentation in the substrate, the model shows a rich phase diagram of low-energy bands including eigenvalue fragile phases as well as kagome and honeycomb flat bands. Spin-orbit coupling in the substrate can lift symmetry-protected degeneracies and create spin Chern bands, and we observe spin Chern numbers up to three. We additionally propose a moiré system formed by stacking two graphene-like layers with similar lattice constants and Fermi energies but with Dirac Fermi velocities of opposite sign. This system exhibits multiple kagome and honeycomb flat bands simultaneously. Both models we propose resemble the hypermagic model of [Scheer *et al.*, Phys. Rev. B **106**, 115418 (2022)] and may provide ideal platforms for the realization of strongly correlated topological phases.

I. INTRODUCTION

Since the discovery of the fractional quantum Hall effect, nontrivial flat bands in two dimensions have become a dominant paradigm for strongly correlated topological phases of matter. In recent years, moiré systems such as twisted bilayer graphene (TBG) [1] have been predicted to host nontrivial flat bands [2–5] and experiments have revealed remarkable strongly interacting phenomena such as unconventional superconductivity and correlated insulation [6–12]. Another way to realize nontrivial flat bands is to construct tight-binding models that exhibit destructive wavefunction interference [13–15]. For example, a nearest-neighbor tight-binding model with one symmetric orbital per site on a kagome lattice has one exactly flat band [16,17]. Interacting systems based on this tight-binding model have long been investigated as candidates for strongly correlated phases such as Mott insulators or spin liquids [18,19]. Similarly, a nearest-neighbor tight-binding model with p_x and p_y orbitals on each site of a honeycomb lattice has two exactly flat bands when certain parameters are neglected [20]. For completeness, we review these flat band tight-binding models in Appendices K and L. Despite extensive searches for crystalline materials realizing such nontrivial flat bands, they remain quite rare. Additionally, it is often difficult to tune the Fermi level into a flat band [19,21–23].

A natural question is whether kagome or honeycomb flat-band tight-binding models can be realized in moiré materials, which generally enjoy highly tunable Fermi levels. Recent studies on moiré models for twisted crystalline materials with triangular Bravais lattices and low-energy physics near the $\mathbf{\Gamma}$ point have found kagome and honeycomb flat bands. These so-called $\mathbf{\Gamma}$-valley models have been derived for transition metal dichalcogenides (TMDs) [25,26], interfaces between topological insulators and ferromagnetic insulators [27], and semiconductors [28]. Kagome and honeycomb moiré superlattices have been observed with scanning tunneling microscopy in twisted bilayer WSe$_2$,

although the orbitals from which they emerge remain obscure [29].

In this paper, we introduce a graphene-based moiré model that realizes kagome and honeycomb lattice flat bands. We consider a graphene layer stacked on a two-dimensional crystalline substrate with a triangular Bravais lattice and a lattice constant approximately $\sqrt{3}$ times that of graphene. At a twist angle near 30°, the two layers are nearly commensurate and produce a moiré pattern as shown in Fig. 1(c). The $\mathbf{K}$ and $-\mathbf{K}$ graphene valleys are both folded close to the $\mathbf{\Gamma}$ point of the substrate, and are thus coupled by van der Waals interactions. Assuming the substrate states near the $\mathbf{\Gamma}$ point are gapped at the graphene Fermi energy, the low-energy physics in the graphene layer can be described by a continuum model consisting of two Dirac cones with intervalley and intravalley moiré potentials. We refer to this model as the *coupled-valley graphene model*. When the substrate has maximal symmetry and the interlayer twist angle is exactly 30°, the model respects the magnetic space group $P6mm1'$ (No. 183.186 in the BNS setting [30]). A particularly interesting limit is that in which the moiré potentials are produced entirely by substrate states occupying a two-dimensional (2D) spinless irreducible corepresentation (coirrep) [31]. Without spin-orbit coupling (SOC), we find a rich phase diagram of low-energy bands including eigenvalue fragile phases [32] and magic parameters with kagome or honeycomb flat bands near charge neutrality. With SOC in the substrate, the z component of spin is approximately conserved. We find moiré bands with spin Chern numbers up to three, allowing realization of the quantum spin Hall effect [33,34].

We note that commensurate bilayers with exactly $\sqrt{3}$ lattice constant ratio and perfect 30° alignment have been studied using density-functional theory [35,36]. Moiré materials near this configuration have also been studied theoretically and experimentally [37–40]. However, these studies did not consider the case in which the moiré potentials are produced
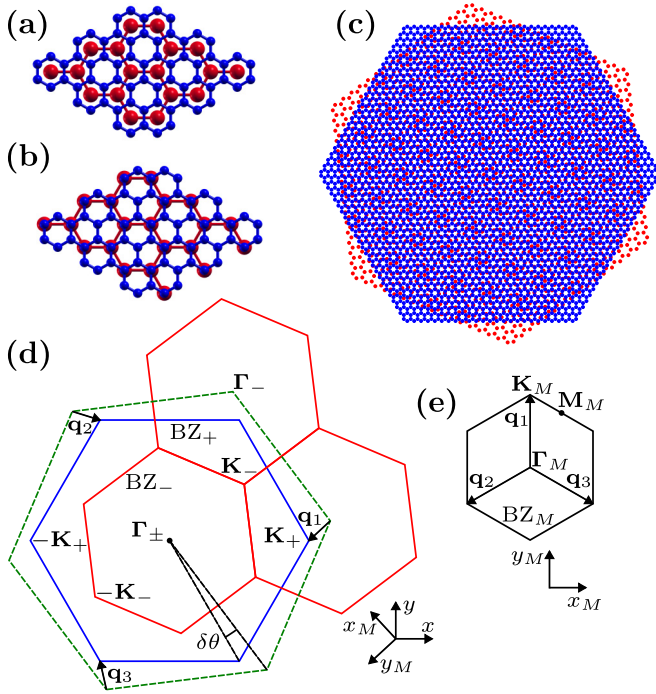
FIG. 1. Illustration of the coupled-valley graphene model. [(a),(b)] Real-space commensurate stacking configurations described by Eq. (2) for two honeycomb lattice materials (made with [24]). (c) The moiré pattern of two honeycomb lattices described by Eqs. (1) and (2) with $\delta\epsilon = -0.15$ and $\delta\theta = 7°$. (d) A momentum-space diagram illustrating the moiré vectors $\mathbf{q}_j$, the graphene coordinate system (x, y), and the moiré coordinate system (x_M, y_M). The graphene and substrate BZs are shown in blue and red, respectively. The green dashed hexagon is formed from substrate $\mathbf{\Gamma}_-$ points and coincides with the graphene BZ when $\delta\epsilon = \delta\theta = 0$. (e) The moiré BZ and high-symmetry moiré quasimomenta in the moiré coordinate system (x_M, y_M). This diagram pertains to both the coupled-valley graphene and opposite-velocity models.

by a 2D spinless coirrep in the layer with a larger lattice constant, nor did they report kagome or honeycomb moiré flat bands.

We additionally propose a moiré model consisting of two stacked graphene-like materials with nearly equal lattice constants, both of which have Dirac cones at $\mathbf{K}$ and $-\mathbf{K}$. We show that if the two layers have nearly opposite Dirac Fermi velocities and nearly equal Fermi energies, the system may have multiple kagome and honeycomb moiré flat bands simultaneously near charge neutrality. We refer to this model as the *opposite-velocity model*. Both models we propose bear strong mathematical resemblance to the hypermagic model of Ref. [41].

II. COUPLED-VALLEY GRAPHENE MODEL

We consider a system consisting of a graphene layer stacked on top of a 2D crystalline substrate with a triangular Bravais lattice. The lattice constants of graphene and the substrate are $a \approx 0.246$ nm and $e^\epsilon a$, respectively, for some real number ϵ. Additionally, the substrate Bravais lattice has a counterclockwise rotation of angle θ relative to that of the

graphene layer. In order to create a moiré pattern, we take

$$\epsilon = \epsilon_0 + \delta\epsilon, \quad \theta = \theta_0 + \delta\theta, \quad |\delta\epsilon|, |\delta\theta| \ll 1, \quad (1)$$

where ϵ_0 and θ_0 describe some commensurate configuration [42]. For the coupled-valley graphene model, we take

$$\epsilon_0 = \ln\sqrt{3}, \quad \theta_0 = 30°. \quad (2)$$

Hereafter, we use $+$ and $-$ subscripts to denote momenta in the top (graphene) and bottom (substrate) layers, respectively. As illustrated in Fig. 1(d), when $\delta\epsilon = \delta\theta = 0$ the momentum $\mathbf{K}_+$ is an element of the commensurate reciprocal lattice. As a result, when $\delta\epsilon$ and $\delta\theta$ are not both zero, graphene states near $\mathbf{K}_+$, $-\mathbf{K}_+$, and $\mathbf{\Gamma}_+$ are van der Waals coupled to substrate states near $\mathbf{\Gamma}_-$, yielding a moiré Brillouin zone (BZ) as shown in Fig. 1(e). The graphene states near $\mathbf{\Gamma}_+$ are far from the graphene Fermi energy and can be ignored. Assuming the substrate states around $\mathbf{\Gamma}_-$ are also highly detuned, we can use Schrieffer-Wolff perturbation theory to project out the substrate states and derive a moiré model within the graphene layer involving only states near $\mathbf{K}_+$ and $-\mathbf{K}_+$. The result is the *coupled-valley graphene model*, which is derived in detail in Appendices F and G, and which we now present.

We assume that SOC is present only in the substrate and not in the interlayer hoppings. Due to the high symmetry of the $\mathbf{\Gamma}_-$ point, the z component of electron spin is conserved. As a result, we can describe the system with a moiré Hamiltonian H_s for electrons of each spin $s \in \{\uparrow, \downarrow\}$. In a convenient real-space basis, this Hamiltonian takes the form

$$H_s = \begin{pmatrix} S_{s,+}(\mathbf{r}) - i\hbar v_F \boldsymbol{\sigma}_M \cdot \nabla & T_s(\mathbf{r}) \\ T_s^\dagger(\mathbf{r}) & S_{s,-}(\mathbf{r}) - i\hbar v_F \boldsymbol{\sigma}_M \cdot \nabla \end{pmatrix} \quad (3)$$

where $T_s(\mathbf{r})$ and $S_{s,\eta}(\mathbf{r})$ are intervalley and intravalley moiré potentials, $\eta \in \{+, -\}$ stands for graphene valley, $v_F \approx 10^6$ ms^{-1} is the graphene Fermi velocity, $\boldsymbol{\sigma}_M = \sigma_x \hat{\mathbf{x}}_M + \sigma_y \hat{\mathbf{y}}_M$ is a vector of Pauli matrices, and $\hat{\mathbf{x}}_M, \hat{\mathbf{y}}_M$ are axis unit vectors for the moiré coordinate system in Figs. 1(d) and 1(e). We choose the zero-energy point to be the graphene Fermi energy. As explained in Appendices F and G, we have chosen a basis in which the two Dirac cones in Eq. (3) have the same form even though they originate from opposite graphene valleys.

To leading order, $T_s(\mathbf{r})$ and $S_{s,\eta}(\mathbf{r})$ originate from second-order hopping processes among the valleys, namely $\eta\mathbf{K}_+ \rightarrow \mathbf{\Gamma}_- \rightarrow -\eta\mathbf{K}_+$, and $\eta\mathbf{K}_+ \rightarrow \mathbf{\Gamma}_- \rightarrow \eta\mathbf{K}_+$, respectively. They can be expanded as

$$T_s(\mathbf{r}) = \sum_{j=1}^{3} \sum_{m=1,-2} T_{s,m\mathbf{q}_j} e^{im\mathbf{q}_j \cdot \mathbf{r}},$$

$$S_{s,\eta}(\mathbf{r}) = S_{s,\eta,\mathbf{0}} + \sum_{j=1}^{3} \sum_{\gamma=\pm} S_{s,\eta,\gamma(\mathbf{q}_{1+j}-\mathbf{q}_{2+j})} e^{i\gamma(\mathbf{q}_{1+j}-\mathbf{q}_{2+j})\cdot\mathbf{r}}, \quad (4)$$

for 2×2 complex matrices $T_{s,\mathbf{q}}$ and $S_{s,\eta,\mathbf{q}}$. The $\mathbf{q}_j$ vectors are defined by

$$\mathbf{q}_j = R_{\zeta_j}\mathbf{K}_M = |\mathbf{K}_M| R_{\zeta_j} \hat{\mathbf{y}}_M \quad (5)$$

where

$$\mathbf{K}_M = (1 - e^{-\delta\epsilon} R_{\delta\theta})\mathbf{K}_+, \quad |\mathbf{K}_M| \approx \sqrt{\delta\epsilon^2 + \delta\theta^2}|\mathbf{K}_+|. \quad (6)$$

TABLE I. (a) Coefficients for expansions of $T_{s,\mathbf{q}}$ and $S_{s,\eta,\mathbf{q}}$ in Eq. (4) with respect to the matrices shown in the column titles. The parameters $w_{m,\mu}$ and $\tilde{w}_{m,\mu}$ are real and have energy units, and $\tilde{w}_{m,\mu} = 0$ in the absence of SOC. The angle ϕ_1 is defined in Eq. (7), $\zeta_j = \frac{2\pi}{3}(j-1)$, $\hat{\mathbf{n}}_\phi = R_\phi\hat{\mathbf{x}}$, and $\boldsymbol{\sigma} = \sigma_x\hat{\mathbf{x}} + \sigma_y\hat{\mathbf{y}}$. The index values are $j \in \{1, 2, 3\}$, $m \in \{1, -2\}$, and $\gamma \in \{1, -1\}$. (b) Expressions for $w_{m,\mu}$ in terms of E_0 and v for a 1D spinless coirrep. (c) Expressions for $w_{m,\mu}$ in terms of E_0, v_0, and v_x for a 2D spinless coirrep. (d) Expressions for $\tilde{w}_{m,\mu}$ in terms of E_0, λ, v_0, and v_x for a 2D spinless coirrep with SOC.

(a) $T_{s,\mathbf{q}}$ and $S_{s,\eta,\mathbf{q}}$	σ_0	$\boldsymbol{\sigma}\cdot\hat{\mathbf{n}}_{\zeta_j+\phi_1-\pi/2}$	$\boldsymbol{\sigma}\cdot\hat{\mathbf{n}}_{\zeta_j+\phi_1}$	σ_z
$T_{s,m\mathbf{q}_j}$	$is\tilde{w}_{|m|,0}$	0	$w_{|m|,y}$	$iw_{|m|,z}$
$S_{s,\eta,\mathbf{0}}$	$w_{0,0}$	0	0	$s\tilde{w}_{0,z}$
$S_{s,\eta,\gamma(\mathbf{q}_{1+j}-\mathbf{q}_{2+j})}$	$w_{\sqrt{3},0} + is\eta\gamma\tilde{w}_{\sqrt{3},0}$	$\eta w_{\sqrt{3},x} + is\gamma\tilde{w}_{\sqrt{3},x}$	0	$s\tilde{w}_{\sqrt{3},z} + i\eta\gamma w_{\sqrt{3},z}$
(b) 1D coirrep	0	x	y	z
$E_0 w_{0,\mu}$	$-3|v|^2$	0	0	0
$E_0 w_{1,\mu}$	0	0	$-2v^2$	$M_{y,-}v^2$
$E_0 w_{2,\mu}$	0	0	$-v^2$	$-M_{y,-}v^2$
$E_0 w_{\sqrt{3},\mu}$	$\frac{1}{2}|v|^2$	$-M_{y,-}|v|^2$	0	$-\frac{\sqrt{3}}{2}|v|^2$
(c) 2D coirrep	0	x	y	z
$E_0 w_{0,\mu}$	$-3(|v_0|^2 + |v_x|^2)$	0	0	0
$E_0 w_{1,\mu}$	0	0	$2v_0 v_x$	$v_0^2 - 2v_x^2$
$E_0 w_{2,\mu}$	0	0	$-2v_0 v_x$	$-(v_0^2 + v_x^2)$
$E_0 w_{\sqrt{3},\mu}$	$\frac{1}{2}(|v_0|^2 - 2|v_x|^2)$	$\frac{1}{2}(v_0 v_x^* + v_0^* v_x)$	0	$\frac{\sqrt{3}}{2}|v_0|^2$
(d) 2D coirrep (SOC)	0	x	y	z
$E_0 \tilde{w}_{0,\mu}$	0	0	0	$3\lambda(-|v_0|^2 + |v_x|^2)$
$E_0 \tilde{w}_{1,\mu}$	$\lambda(v_0^2 + 2v_x^2)$	0	0	0
$E_0 \tilde{w}_{2,\mu}$	$\lambda(-v_0^2 + v_x^2)$	0	0	0
$E_0 \tilde{w}_{\sqrt{3},\mu}$	$\frac{\lambda\sqrt{3}}{2}|v_0|^2$	$-\frac{\lambda\sqrt{3}}{2}(v_0 v_x^* + v_0^* v_x)$	0	$\frac{\lambda}{2}(|v_0|^2 + 2|v_x|^2)$

Here, R_ϕ denotes rotation by angle ϕ about $\hat{\mathbf{z}}$ and $\zeta_j = \frac{2\pi}{3}(j-1)$. The $\mathbf{q}_j$ vectors, moiré coordinate system, moiré BZ, and high-symmetry moiré quasimomenta are illustrated in Figs. 1(d) and 1(e).

The graphene electronic states carry a corepresentation (corep) of the magnetic space group $P6mm1'$, which is generated by Bravais lattice translations, C_{6z} (rotation by $\pi/3$ about $\hat{\mathbf{z}}$), M_y (reflection through the xz plane), and $\mathcal{T}$ (spinful time-reversal). We assume that the substrate states also carry a corep of $P6mm1'$. When $\delta\theta = 0$, the moiré model in Eq. (3) then also carries a corep of $P6mm1'$. In this case, the symmetries constrain the moiré potentials to the form in Table I(a), where the parameters $w_{m,\mu}$ and $\tilde{w}_{m,\mu}$ are real and have energy units, the $\tilde{w}_{m,\mu}$ parameters vanish in the absence of SOC, and

$$\phi_1 = \arg(e^{-\delta\epsilon - i\delta\theta} - 1) \approx \arg(-\delta\epsilon - i\delta\theta). \qquad (7)$$

When $\delta\theta$ is nonzero but small, the M_y symmetry is weakly broken. The moiré potentials may then gain small symmetry-breaking perturbations on the order of $\delta\theta$, but these are typically negligible. See Sec. III of Ref. [41] for a discussion of a similar symmetry-breaking term in the model for TBG near a commensurate twist angle.

We first examine the case without SOC. The moiré potentials are then spin independent and are determined by the spinless interlayer coupling and substrate Hamiltonian $\mathcal{H}_-$ at $\boldsymbol{\Gamma}_-$. $\mathcal{H}_-$ carries a spinless corep ρ_- of the magnetic point group $6mm1'$ (see Appendix I). By Schur's lemma, one can diagonalize $\mathcal{H}_-$ while also decomposing ρ_- into coirreps. As a result, we can expand the moiré potentials in Eq. (4) as a sum of contributions of coirreps in ρ_-.

The spinless coirreps of $6mm1'$ all have dimension 1 or 2 (see Table III). The moiré potential contribution from a 1D spinless coirrep depends on its energy E_0 in $\mathcal{H}_-$ (measured relative to the graphene Fermi energy) and an interlayer hopping parameter v, while the contribution from a 2D spinless coirrep depends on its energy E_0 and two interlayer hopping parameters, v_0 and v_x. The parameter v is either real or imaginary, depending on the coirrep. Likewise, v_0 and v_x are either both real or both imaginary. The $w_{m,\mu}$ parameters are given in terms of E_0, v, v_0, and v_x in Table I [(b) and (c)].

We now suppose that the substrate has SOC, and note that any effect of SOC on the interlayer couplings can be neglected at leading order. Since all spinful coirreps of $6mm1'$ have dimension 2 (see Table III), the inclusion of spin maps 1D spinless coirreps to 2D spinful coirreps and 2D spinless coirreps to 4D spinful reducible coreps. As a result, SOC can only modify contributions arising from 2D spinless coirreps, and in this case it simply splits the 4D spinful corep into two spinful coirreps with energies E_1 and E_2. We define

$$E_0 = \frac{2}{E_1^{-1} + E_2^{-1}}, \quad \lambda = \frac{E_1^{-1} - E_2^{-1}}{E_1^{-1} + E_2^{-1}}, \qquad (8)$$

where λ characterizes the SOC strength. The parameters $w_{m,\mu}$ and $\tilde{w}_{m,\mu}$ for a 2D spinless coirrep with SOC are given in Table I [(c) and (d)] in terms of E_0, λ, v_0, and v_x.

Since $w_{m,\mu}$ and $\tilde{w}_{m,\mu}$ for a single coirrep vary inversely with E_0, the moiré potentials will typically be dominated by coirreps near the graphene Fermi energy. We consider now the intriguing limit in which the moiré potentials arise entirely from a single 2D spinless coirrep. Without loss of generality, we assume $v_0, v_x \in \mathbb{R}$ (see Appendix J). In this case, the

model can be parameterized by the dimensionless quantities

$$\alpha = \frac{|v_0|^2 + |v_x|^2}{|E_0|\hbar v_F |\mathbf{K}_M|}, \quad \varphi = \arg(v_0 + iv_x), \quad (9)$$

λ, ϕ_1, and the sign of E_0. The parameter α resembles the parameter of the same name in the BM model [1] in that larger α corresponds to stronger interlayer coupling and larger moiré lattice constant.

We focus on the case with $\delta\theta = 0$ and $\delta\epsilon \neq 0$. Without loss of generality, we choose $\delta\epsilon < 0$, $\phi_1 = 0$, and $E_0 < 0$ (see Appendix J). We then explore the moiré band structure without SOC as a function of $\alpha \in (0, \infty)$ and $\varphi \in [0, \pi)$. For each set of parameters, we identify a low-energy band structure, by which we mean a minimal set of bands containing the first valence and conduction bands such that the symmetry coirreps at high-symmetry points (i.e., Γ_M, $\mathbf{K}_M$, and $\mathbf{M}_M$) are well defined and satisfy the momentum-space compatibility relations for $P6mm1'$ from magnetic topological quantum chemistry [43,45–47]. We then define the phases by identifying an integer linear combination of elementary band representations (EBRs) with a minimal sum for the negative coefficients compatible with each low-energy band structure. Figure 2(b) shows all phases for which the low-energy band structure has at most four bands and Fig. 2(c) tabulates the EBR decompositions for the nine largest such phases. The full list of EBRs for each magnetic space group can be found on the Bilbao Crystallographic Server [43,44]. Example band structures are shown with solid lines in Figs. 3(a)–3(d) and Figs. 5(a)–5(e). The low (high)-energy bands are shown in red (black).

Remarkably, phase 1 is compatible with the EBR for the honeycomb lattice flat-band model [20] (see Appendix K 3), while phases 7 and 8 are compatible with EBRs for the kagome lattice flat-band model [16,17] (see Appendix K 2). Moreover, the linear combinations of EBRs for phases 4, 6, and 9 include a subtraction, implying that these phases have at least a fragile topology when the low-energy bands are isolated [32,48–51]. Real-space charge density distributions corresponding to the low-energy band structures are shown in Figs. 3(e)–3(h) and Figs. 5(f)–5(j). Triangular, honeycomb, and kagome lattice patterns are clearly visible for phases 2, 1, and 8, respectively, in agreement with Fig. 2(c).

In addition to identifying phases, it is also important to search for flat bands. The dark regions in Fig. 2(a) indicate parameters for which there is a flat band among the first three valence and first three conduction bands. We see that several phases admit flat bands, and the parameters for Figs. 3(a), 3(c), and 3(d) were chosen to exhibit extremely flat bands near charge neutrality.

With SOC, the symmetry-protected degeneracies are generically split and the bands gain spin Chern numbers $C_\uparrow$ and $C_\downarrow = -C_\uparrow$. The dashed lines in Figs. 3(a)–3(d) and 5(a)–5(e) show moiré band structures with SOC. For example, Fig. 3(d) has a band with $C_\uparrow = 3$. We note that the spin Chern numbers with fixed λ are not necessarily constant within each spinless phase.
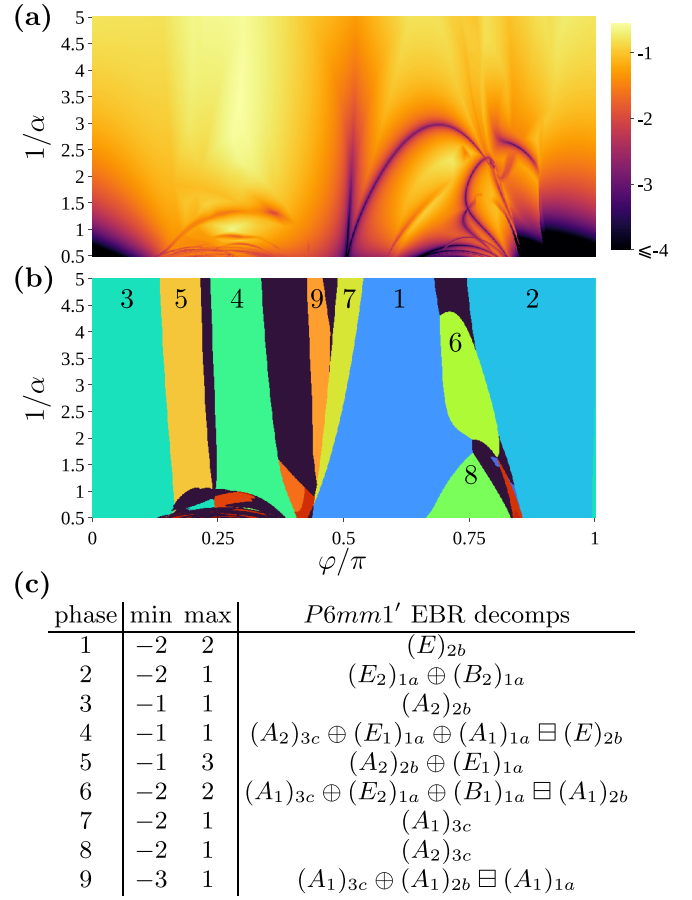

FIG. 2. Low-energy bandwidths and phase diagram of low-energy bands for the coupled-valley graphene model without SOC and with moiré potentials arising from a 2D spinless coirrep at Γ_-. We take $\delta\theta = 0$, $\delta\epsilon < 0$, $\phi_1 = 0$, $v_0, v_x \in \mathbb{R}$, $\lambda = 0$, and $E_0 < 0$. (a) The base 10 logarithm of the narrowest bandwidth (in units of $\hbar v_F |\mathbf{K}_M|$) among the first three valence bands and first three conduction bands at charge neutrality. The bandwidth is computed with moiré quasimomenta Γ_M, $\mathbf{K}_M$, $\mathbf{M}_M$, $\mathbf{K}_M/2$, and $\mathbf{M}_M/2$. (b) Phase diagram of low-energy bands. All parameters for which the low-energy band structure has more than four bands are shown in black. (c) For each of the nine largest phases in (b), we show the band indices and a linear combination of EBRs of $P6mm1'$ for the low-energy band structure. The nth conduction (valence) band has index n ($-n$). The symbols $\oplus$ and $\boxminus$ indicate sum and difference of EBRs, respectively. The full list of EBRs for $P6mm1'$ can be found on the Bilbao Crystallographic Server [43,44].

phase	min	max	$P6mm1'$ EBR decomps
1	-2	2	$(E)_{2b}$
2	-2	1	$(E_2)_{1a} \oplus (B_2)_{1a}$
3	-1	1	$(A_2)_{2b}$
4	-1	1	$(A_2)_{3c} \oplus (E_1)_{1a} \oplus (A_1)_{1a} \boxminus (E)_{2b}$
5	-1	3	$(A_2)_{2b} \oplus (E_1)_{1a}$
6	-2	2	$(A_1)_{3c} \oplus (E_2)_{1a} \oplus (B_1)_{1a} \boxminus (A_1)_{2b}$
7	-2	1	$(A_1)_{3c}$
8	-2	1	$(A_2)_{3c}$
9	-3	1	$(A_1)_{3c} \oplus (A_1)_{2b} \boxminus (A_1)_{1a}$

III. OPPOSITE-VELOCITY MODEL

We now introduce another moiré construction yielding kagome and honeycomb flat bands (see Appendix H for a detailed derivation). We consider a stack of two 2D materials with triangular Bravais lattices and $P6mm1'$ symmetry. We assume that both layers have Dirac cones at their $\mathbf{K}$ and $-\mathbf{K}$ points centered at their Fermi energies, carrying the same coreps of $P6mm1'$ as that of graphene. The bottom layer to top layer lattice constant ratio e^ϵ and counterclockwise twist angle θ satisfy Eq. (1) with
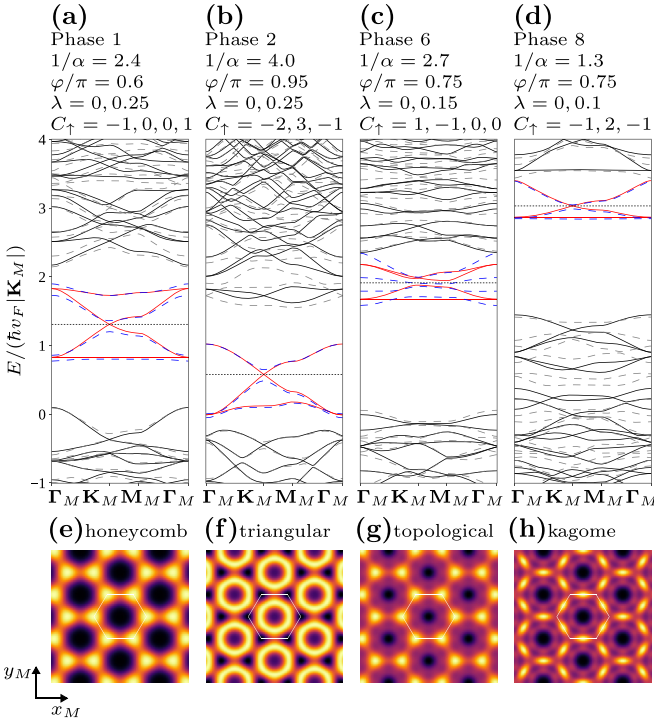
$$\epsilon_0 = 0, \quad \theta_0 = 0, \quad (10)$$

FIG. 3. [(a)–(d)] Moiré band structures of the coupled-valley model in Eq. (3) for phases 1, 2, 6, and 8 of Fig. 2(b), with parameters written above the panels. Band structures without (with) SOC are shown with solid (dashed) lines. The black dotted lines indicate charge neutrality. The low (high)-energy bands are shown without SOC in red (black) and with SOC in blue (gray). The spin Chern numbers are written in increasing order of energy above the panels. [(e)–(h)] Real-space charge density distributions from fully filling only the low-energy spinless bands shown in red in (a)–(d). Lighter colors indicate higher charge densities. A moiré unit cell is shown as a white hexagon. A description of the EBR decomposition given in Fig. 2(c) is written above each panel. The low-energy spinless bands illustrated in (c) and (g) have at least a fragile topology and therefore do not admit exponentially localized symmetric Wannier functions [32,48,49,51]. The highest two spinless valence bands in (c) are compatible with the EBR decomposition $(A_1)_{3c} \oplus (B_1)_{1a} \boxminus (A_1)_{2b}$ while the lowest two spinless conduction bands are compatible with $(E_2)_{1a}$. Figure 5 contains similar plots for the other phases tabulated in Fig. 2(c).

so that

$$\epsilon = \delta\epsilon, \quad \theta = \delta\theta, \quad |\epsilon|, |\theta| \ll 1. \tag{11}$$

We study only the case without SOC for simplicity. The system is illustrated in Figs. 4(a) and 4(b).

As in the BM model for TBG, the two valleys $\mathbf{K}_\pm$ and $-\mathbf{K}_\pm$ are nearly decoupled and are related by time-reversal. In a convenient real-space basis, the Hamiltonian for the $\mathbf{K}_\pm$ valley takes the form

$$H = \begin{pmatrix} S_+(\mathbf{r}) - i\hbar v_+ \boldsymbol{\sigma}_M \cdot \nabla & T(\mathbf{r}) \\ T^\dagger(\mathbf{r}) & S_-(\mathbf{r}) + i\hbar v_- \boldsymbol{\sigma}_M \cdot \nabla \end{pmatrix} \tag{12}$$

where $T(\mathbf{r})$ and $S_l(\mathbf{r})$ are interlayer and intralayer moiré potentials, $l \in \{+, -\}$ indicates layer, v_l is the Dirac cone Fermi velocity for layer l, $\boldsymbol{\sigma}_M = \sigma_x \hat{\mathbf{x}}_M + \sigma_y \hat{\mathbf{y}}_M$ is a vector
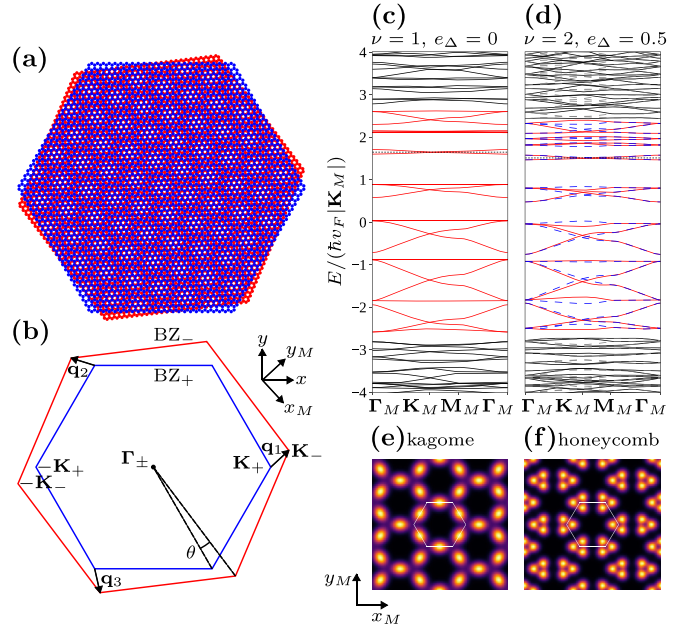

FIG. 4. Illustration of the opposite-velocity model. (a) A moiré pattern for two honeycomb lattices with $\epsilon = -0.15$ and $\theta = 7°$. (b) A momentum-space diagram illustrating the $\mathbf{q}_j$ moiré vectors, the top layer coordinate system (x, y), and the moiré coordinate system (x_M, y_M). The top (bottom) layer BZ is shown in blue (red). [(c),(d)] Moiré band structures with $w_0/|w_1| = 0.8$, $\phi_1 \in \{0, \pi\}$, $w_1 \cos \phi_1 > 0$, and $1/\alpha = 0.5$, with ν and e_Δ given above each panel. The black dotted lines indicate charge neutrality. The parameters for (c) realize the hypermagic model and have an emergent C_{2z} symmetry. In (d), the solid lines show bands along $\boldsymbol{\Gamma}_M \to \mathbf{K}_M \to \mathbf{M}_M \to \boldsymbol{\Gamma}_M$ while the dashed lines shown bands along $\boldsymbol{\Gamma}_M \to -\mathbf{K}_M \to -\mathbf{M}_M \to \boldsymbol{\Gamma}_M$. These bands differ because the emergent C_{2z} symmetry is absent. (e) The real-space charge density distribution from fully filling only bands -4 to -2 in (c), which forms a kagome lattice pattern. (f) The real-space charge density distribution from fully filling only bands -1 and 1 in (c), which forms a honeycomb lattice pattern. Here, the nth conduction (valence) band has index n $(-n)$. See Fig. 6 for charge density distributions for the other red bands in (c) as well as EBR decompositions for the red bands in (c) and the red and blue bands in (d).

of Pauli matrices, and $\hat{\mathbf{x}}_M, \hat{\mathbf{y}}_M$ are axis unit vectors for the moiré coordinate system in Figs. 4(b) and 1(e). As explained in Appendix H, we have chosen a basis in which the sign for the bottom layer Dirac cone is negated.

To leading order, the moiré potentials can be expanded as

$$T(\mathbf{r}) = \sum_{j=1}^{3} T_{\mathbf{q}_j} e^{i\mathbf{r}\cdot\mathbf{q}_j}, \quad S_l(\mathbf{r}) = S_{l,\mathbf{0}}, \tag{13}$$

for 2×2 complex matrices $T_\mathbf{q}$ and $S_{l,\mathbf{q}}$. The $\mathbf{q}_j$ vectors are defined by Eq. (5) with

$$\mathbf{K}_M = (e^{-\epsilon} R_\theta - 1)\mathbf{K}_+, \quad |\mathbf{K}_M| \approx \sqrt{\epsilon^2 + \theta^2} |\mathbf{K}_+|. \tag{14}$$

The $\mathbf{q}_j$ vectors, moiré coordinate system, moiré BZ, and high-symmetry moiré quasimomenta are illustrated in Figs. 4(b) and 1(e).

When $\theta = 0$, the moiré model in Eq. (12) inherits all valley preserving symmetries from the spinless coreps of $P6mm1'$

on the two layers. Since C_{2z} (rotation by π about $\hat{\mathbf{z}}$) and $\mathcal{T}$ reverse valley, the moiré model carries a spinless corep of the magnetic space group $P6'm'm$ (No. 183.187 in the BNS setting [30]), which is generated by Bravais lattice translations, C_{3z} (rotation by $2\pi/3$ about $\hat{\mathbf{z}}$), $C_{2z}\mathcal{T}$, and M_y. In this case, the symmetries imply

$$T_{\mathbf{q}_j} = w_1\boldsymbol{\sigma} \cdot \hat{\mathbf{n}}_{\zeta_j + \phi_1} + iw_0\sigma_z,$$
$$S_{l,\mathbf{0}} = \left(E_F + \frac{lE_\Delta}{2}\right)\sigma_0, \quad (15)$$

for real parameters w_0, w_1, E_F, and E_Δ. Here, $\hat{\mathbf{n}}_\phi = R_\phi\hat{\mathbf{x}}$, $\boldsymbol{\sigma} = \sigma_x\hat{\mathbf{x}} + \sigma_y\hat{\mathbf{y}}$, and

$$\phi_1 = \arg(1 - e^{-\epsilon - i\theta}) \approx \arg(\epsilon + i\theta). \quad (16)$$

Without loss of generality, we set $E_F = 0$. When θ is nonzero but small, the M_y symmetry is weakly broken. The moiré potentials may then gain small perturbations on the order of θ, but these are typically negligible. For simplicity, we assume $\theta = 0$ and $\epsilon \neq 0$ hereafter, in which case $\phi_1 \in \{0, \pi\}$.

We refer to this model in the regime $v_-v_+ < 0$ as the *opposite-velocity model*. If both layers are graphene-like honeycomb lattices, this requires their in-plane nearest-neighbor hoppings to have opposite signs [52]. We parametrize the model by the dimensionless quantities

$$v = -\frac{v_+}{v_-}, \quad \alpha = \frac{|w_1|}{\hbar v_F|\mathbf{K}_M|}, \quad e_\Delta = \frac{E_\Delta}{\hbar v_F|\mathbf{K}_M|}, \quad (17)$$

$w_0/|w_1|$, and the sign of $w_1\cos\phi_1$, where $v_F = \sqrt{|v_+v_-|}$. In particular, when $v = 1$ and $e_\Delta = 0$ (i.e., the two layers have opposite Dirac Fermi velocities and equal Fermi energies), the Hamiltonian gains an emergent effective C_{2z} symmetry that sends $\mathbf{r} \mapsto -\mathbf{r}$ and interchanges the layers, and the space group is enriched to $P6mm1'$. In this case, the Hamiltonian in Eq. (12) has the same form as the hypermagic model given in Eqs. (71), (74), and (75) of Ref. [41] with $|\phi_0| = \pi/2$, and the $T_{\mathbf{q}_j}$, $S_{l,\mathbf{0}}$ matrices have the same form as the $T_{s,\mathbf{q}_j}$, $S_{s,\eta,\mathbf{0}}$ matrices in Table I(a) with $\tilde{w}_{m,\mu} = 0$. This happens because the coreps of $P6mm1'$ in the coupled-valley graphene model without SOC in Eq. (3) and the hypermagic model are the same.

Figure 4(c) shows an example band structure with $v = 1$ and $e_\Delta = 0$, which simultaneously exhibits at least eight flat bands. All the low-energy bands in red are compatible with EBRs of $P6mm1'$ supported on honeycomb or kagome lattices. The EBR for each group of bands is shown in Fig. 6(f). In particular, four (two) groups of connected bands correspond to kagome (honeycomb) lattice flat-band models (see Appendix K), which can be observed in the real-space charge density distributions in Figs. 4(e) and 4(f) and Figs. 6(a)–6(e).

Figure 4(d) shows an example band structure identical to that in Fig. 4(c), except that $v = 2$ and $e_\Delta = 0.5$ so the emergent C_{2z} symmetry is absent. Interestingly, all of the flat bands in Fig. 4(a) remain quite flat in Fig. 4(b). The main change is that the EBR of $P6mm1'$ corresponding to the honeycomb lattice flat-band model becomes a composite band representation of $P6'm'm$, and one of the two groups of bands with this EBR splits into two disconnected groups. The groups of bands supported on kagome lattices remain connected. The EBR decomposition for each group of bands is shown in Fig. 6(g).

IV. DISCUSSION

A considerable number of 2D materials (e.g., germanene and CdS) are known to have lattice constant approximately $\sqrt{3}$ times that of graphene [37,39]. These materials can be considered candidate substrates for the coupled-valley graphene model in Eq. (3). In addition to the appropriate lattice constant, a substrate material must have a 2D spinless coirrep at the $\boldsymbol{\Gamma}$ point near the graphene Fermi energy in order to realize the phases in Fig. 2(b). In order to find such materials, *ab initio* studies are needed.

We note that for a given substrate, the moiré potentials may be tuned with pressure (which modulates interlayer hopping) and out-of-plane displacement field (which modulates the relative energies of states in the two layers). Additionally, if the substrate material is placed both above and below the graphene layer, the moiré potentials will be enhanced by a factor of two. This is similar to the case of symmetric twisted trilayer graphene [53,54].

In comparison to $\boldsymbol{\Gamma}$-valley models, which also have kagome or honeycomb moiré flat bands [25–28], the coupled-valley graphene model has the advantage that the electrons are localized within graphene, which is a clean and theoretically well-understood material. Additionally, our model shows a rich phase diagram of low-energy bands including eigenvalue fragile phases in addition to flat bands.

It is less clear how to realize the opposite-velocity model in Eq. (12). However, this model can host many kagome or honeycomb flat bands simultaneously, so a realization could provide a variety of interacting phases within a single sample. It is worth noting additionally that both models we propose could potentially be realized with metamaterials [55].

APPENDIX A: ADDITIONAL FIGURES

Figures 5 and 6 are continuations of Figs. 3 and 4, respectively.

APPENDIX B: NOTATIONS

Throughout this paper we consider bilayer structures formed from two crystalline materials with triangular Bravais lattices. We use $l = +$ and $l = -$ to denote the top and bottom layers, respectively. The top layer has lattice constant a and the bottom layer has lattice constant $e^\epsilon a$ for some real number ϵ. Additionally, the bottom layer is rotated counterclockwise by angle θ relative to the top layer. We denote the Bravais lattice, reciprocal lattice, primitive unit cell, and Brillouin zone of layer $l \in \{+, -\}$ by L_l, P_l, Ω_l, and BZ_l, respectively. We use $\hat{\mathbf{x}}$, $\hat{\mathbf{y}}$, and $\hat{\mathbf{z}}$ for unit vectors in $\mathbb{R}^3$ and use primitive
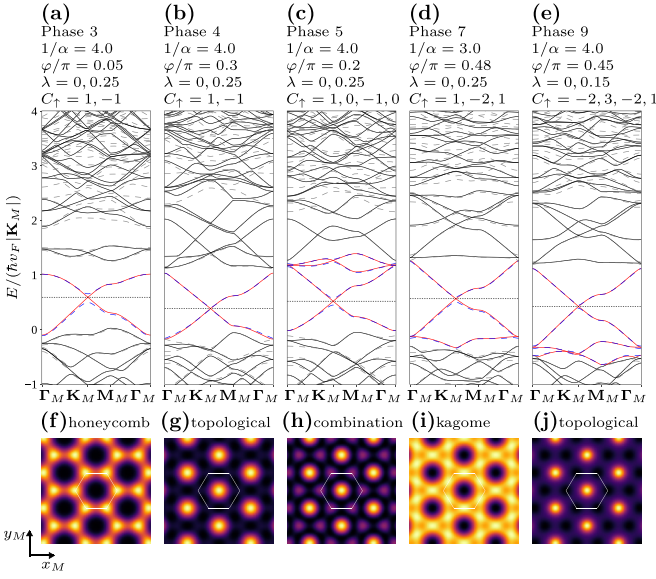
FIG. 5. Continuation of Fig. 3 for phases 3, 4, 5, 7, and 9. See the caption of Fig. 3 for more information.

vectors

$$\mathbf{a}_1 = a\hat{\mathbf{x}}, \quad \mathbf{a}_2 = R_{-\pi/3}\mathbf{a}_1, \tag{B1}$$

for L_+ and

$$\mathbf{b}_1 = R_{2\pi/3}\mathbf{b}_2, \quad \mathbf{b}_2 = -4\pi\hat{\mathbf{y}}/(a\sqrt{3}), \tag{B2}$$

for P_+. We define high-symmetry crystal momenta

$$\mathbf{\Gamma}_+ = \mathbf{0}, \quad \mathbf{K}_+ = \tfrac{2}{3}\mathbf{b}_1 + \tfrac{1}{3}\mathbf{b}_2, \quad \mathbf{M}_+ = \tfrac{1}{2}\mathbf{b}_1 + \tfrac{1}{2}\mathbf{b}_2, \tag{B3}$$

for the top layer and

$$\mathbf{\Gamma}_- = \mathbf{0}, \quad \mathbf{K}_- = e^{-\epsilon}R_\theta\mathbf{K}_+, \quad \mathbf{M}_- = e^{-\epsilon}R_\theta\mathbf{M}_+, \tag{B4}$$

for the bottom layer. We write $|S|$ for the area of a region $S \subset \mathbb{R}^2$ such as BZ_l or Ω_l. R_ϕ denotes rotation by angle ϕ about
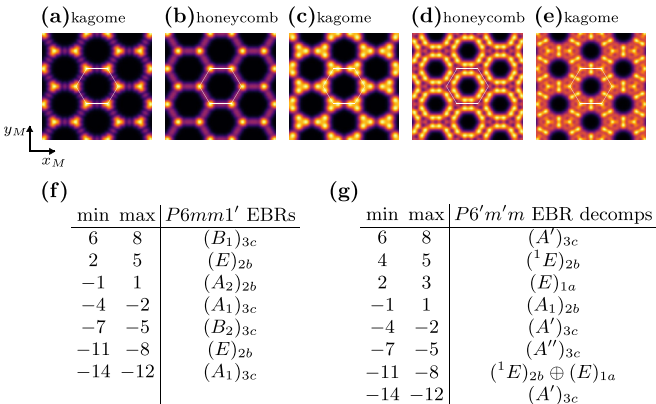

FIG. 6. Continuation of Fig. 4. [(a)–(e)] Real-space charge density distributions for bands -14 to -12, -11 to -8, -7 to -5, 2 to 5, and 6 to 8, respectively in Fig. 4(c). (f) $P6mm1'$ EBRs for the bands shown in red in Fig. 4(c). (g) $P6'm'm$ EBR decompositions for the bands shown in red and blue in Fig. 4(d). The nth conduction (valence) band has index n ($-n$). The symbol $\oplus$ indicates sum of EBRs. The full list of EBRs for $P6mm1'$ and $P6'm'm$ can be found on the Bilbao Crystallographic Server [43,44].

$\hat{\mathbf{z}}$ and $\mathcal{R}_{\hat{\mathbf{n}}}$ denotes reflection through the plane orthogonal to the vector $\hat{\mathbf{n}} \in \mathbb{R}^3$. If V, V_1, and V_2 are sets of vectors, $\mathbf{u}$ is a vector, and r is a real number, we define

$$V_1 + V_2 = \{\mathbf{v}_1 + \mathbf{v}_2 | \mathbf{v}_1 \in V_1, \mathbf{v}_2 \in V_2\},$$
$$\mathbf{u} + V = \{\mathbf{u} + \mathbf{v} | \mathbf{v} \in V\}, \quad rV = \{r\mathbf{v} | \mathbf{v} \in V\}. \tag{B5}$$

Finally, we denote the Pauli matrices by σ_x, σ_y, and σ_z, we denote the 2×2 identity matrix by σ_0, and we use the vectors of Pauli matrices $\boldsymbol{\sigma} = \sigma_x\hat{\mathbf{x}} + \sigma_y\hat{\mathbf{y}}$ and $\boldsymbol{\sigma}^* = \sigma_x\hat{\mathbf{x}} - \sigma_y\hat{\mathbf{y}}$.

APPENDIX C: COMMENSURATE CONFIGURATIONS

In the following subsections we enumerate all commensurate configurations, explain some of their properties, and classify them into four types.

1. Conditions for commensuration

We say that two Bravais lattices are commensurate if they share a nonzero element. If the triangular Bravais lattices L_- and L_+ defined in Appendix B are commensurate then their intersection $L_c = L_- \cap L_+$ is another triangular Bravais lattice called the commensuration superlattice. In this section, we derive all values of ϵ and θ such that L_- and L_+ are commensurate. Our approach is similar to that of Appendix D in Ref. [41], which covers the case in which $\epsilon = 0$.

Let $\tilde{a}$ and $\tilde{b}$ be matrices with columns $(\mathbf{a}_1, \mathbf{a}_2)$ and $(\mathbf{b}_1, \mathbf{b}_2)$, respectively. Then every element of L_+ takes the form $\tilde{a}\mathbf{u}_+$ for some integer vector $\mathbf{u}_+$ and every element of L_- takes the form $e^\epsilon R_\theta\tilde{a}\mathbf{u}_-$ for some integer vector $\mathbf{u}_-$. It follows that L_- and L_+ are commensurate if and only if

$$\mathbf{u}_+ = e^\epsilon \tilde{a}^{-1}R_\theta\tilde{a}\mathbf{u}_- \tag{C1}$$

is satisfied by some nonzero integer vectors $\mathbf{u}_-$ and $\mathbf{u}_+$, or equivalently if all matrix elements of $e^\epsilon \tilde{a}^{-1}R_\theta\tilde{a}$ are rational. One can compute

$$e^\epsilon \tilde{a}^{-1}R_\theta\tilde{a} = \begin{pmatrix} x_0 + y_0 & 2y_0 \\ -2y_0 & x_0 - y_0 \end{pmatrix} \tag{C2}$$

where $e^{\epsilon+i\theta} = x_0 + y_0 i\sqrt{3}$. It follows that L_- and L_+ are commensurate if and only if x_0 and y_0 are both rational.

Applying the same argument to the reciprocal lattices, we see that P_- and P_+ are commensurate if and only if all matrix elements of $e^{-\epsilon}\tilde{b}^{-1}R_\theta\tilde{b}$ are rational. Since

$$e^{-\epsilon}\tilde{b}^{-1}R_\theta\tilde{b} = e^{-2\epsilon}\begin{pmatrix} x_0 - y_0 & 2y_0 \\ -2y_0 & x_0 + y_0 \end{pmatrix} \tag{C3}$$

we see that P_- and P_+ are commensurate if and only if L_- and L_+ are commensurate.

For commensurate L_- and L_+, we can write

$$e^{-l(\epsilon+i\theta)} = \frac{\mu_l + \nu_l i\sqrt{3}}{\rho_l} \tag{C4}$$

for $l \in \{+, -\}$ and integers μ_l, ν_l, ρ_l with $\rho_l \geqslant 1$ and $\gcd(\mu_l, \nu_l, \rho_l) = 1$. Any commensurate configuration is equivalent up to an isometry to one with

$$\epsilon \geqslant 0 \quad \text{and} \quad 0 \leqslant \theta \leqslant \pi/6. \tag{C5}$$

Table II shows the parameters for several commensurate configurations satisfying Eq. (C5).

TABLE II. Parameters for all commensurate configurations satisfying Eq. (C5) and $N_- N_+ \leqslant 49$ in increasing order of $N_- N_+$. The parameters μ_+, ν_+, ρ_+, μ_-, ν_-, ρ_-, and θ are defined in Appendix C 1 while N_+ and N_- are defined by Eq. (C26). By Eq. (C27), $e^\epsilon = \sqrt{N_+/N_-}$. The four types of commensurate configuration (I+, I−, II+, and II−) are described in Appendix C 5. The values shown for θ are rounded to four significant figures.

#	Type	μ_+	ν_+	ρ_+	μ_-	ν_-	ρ_-	θ	N_+	N_-
1	I+	1	0	1	1	0	1	0.0°	1	1
2	II+	3	−1	6	3	1	2	30.0°	3	1
3	I−	1	0	2	2	0	1	0.0°	4	1
4	I+	5	−1	14	5	1	2	19.11°	7	1
5	II+	1	0	3	3	0	1	0.0°	9	1
6	II−	3	−1	4	3	1	3	30.0°	4	3
7	II+	3	−1	12	3	1	1	30.0°	12	1
8	I−	7	−1	26	7	1	2	13.9°	13	1
9	I+	1	0	4	4	0	1	0.0°	16	1
10	I+	4	−1	19	4	1	1	23.41°	19	1
11	II−	9	−1	14	9	1	6	10.89°	7	3
12	II+	9	−1	42	9	1	2	10.89°	21	1
13	I−	1	0	5	5	0	1	0.0°	25	1
14	II+	3	−1	18	9	3	2	30.0°	27	1
15	I−	5	−1	7	5	1	4	19.11°	7	4
16	I−	5	−1	28	5	1	1	19.11°	28	1
17	I+	11	−1	62	11	1	2	8.948°	31	1
18	II+	2	0	3	3	0	2	0.0°	9	4
19	II+	1	0	6	6	0	1	0.0°	36	1
20	I+	11	−3	74	11	3	2	25.28°	37	1
21	II−	6	−1	13	6	1	3	16.1°	13	3
22	II+	6	−1	39	6	1	1	16.1°	39	1
23	I−	13	−1	86	13	1	2	7.589°	43	1
24	II−	3	−1	8	6	2	3	30.0°	16	3
25	II+	3	−1	24	6	2	1	30.0°	48	1
26	I+	1	0	7	7	0	1	0.0°	49	1
27	I−	13	−3	14	13	3	14	21.79°	7	7
28	I−	13	−3	98	13	3	2	21.79°	49	1

2. Primitive vectors of L_c

We will now derive the primitive vectors of L_c when L_- and L_+ are commensurate. To do so, we first compute the primitive vectors $\mathbf{u}_l^1$ and $\mathbf{u}_l^2$ of the Bravais lattice consisting of all integer vectors $\mathbf{u}_l$ such that

$$e^{-l\epsilon} \tilde{a}^{-1} R_{-l\theta} \tilde{a} \mathbf{u}_l \in \mathbb{Z}^2. \tag{C6}$$

The primitive vectors of L_c will then be $\tilde{a}\mathbf{u}_+^1$ and $\tilde{a}\mathbf{u}_+^2$, or alternatively $e^\epsilon R_\theta \tilde{a}\mathbf{u}_-^1$ and $e^\epsilon R_\theta \tilde{a}\mathbf{u}_-^2$.

By Eqs. (C2) and (C4), we have

$$e^{-l\epsilon} \tilde{a}^{-1} R_{-l\theta} \tilde{a} = \frac{1}{\rho_l} \begin{pmatrix} \mu_l + \nu_l & 2\nu_l \\ -2\nu_l & \mu_l - \nu_l \end{pmatrix}. \tag{C7}$$

Taking $\mathbf{u}_l = x\hat{\mathbf{x}} + y\hat{\mathbf{y}}$, Eq. (C6) becomes a congruence

$$\begin{pmatrix} \mu_l + \nu_l & 2\nu_l \\ -2\nu_l & \mu_l - \nu_l \end{pmatrix} \begin{pmatrix} x \\ y \end{pmatrix} \equiv \begin{pmatrix} 0 \\ 0 \end{pmatrix} \pmod{\rho_l}. \tag{C8}$$

Multiplying by the adjugate gives $\rho_l | (\mu_l^2 + 3\nu_l^2)x$ and $\rho_l | (\mu_l^2 + 3\nu_l^2)y$. Defining $d_l = \gcd(\rho_l, \mu_l^2 + 3\nu_l^2)$, we then

have $(\rho_l/d_l)|x$ and $(\rho_l/d_l)|y$. Eq. (C8) is then equivalent to

$$\begin{pmatrix} \mu_l + \nu_l & 2\nu_l \\ -2\nu_l & \mu_l - \nu_l \end{pmatrix} \begin{pmatrix} x' \\ y' \end{pmatrix} \equiv \begin{pmatrix} 0 \\ 0 \end{pmatrix} \pmod{d_l} \tag{C9}$$

where $x = (\rho_l/d_l)x'$ and $y = (\rho_l/d_l)y'$. Since $d_l | (\mu_l^2 + 3\nu_l^2)$ and $d_l | \rho_l$, any common prime factor of d_l and ν_l also divides μ_l and ρ_l, which is not possible. This implies $\gcd(d_l, \nu_l) = 1$, and we choose ν_l^{-1} to be an inverse of ν_l modulo d_l. We now consider several cases.

(1) $d_l \equiv 1 \pmod 2$. In this case, either ρ_l is odd or ρ_l is even and $\mu_l + \nu_l$ is odd. Since

$$(\mu_l - \nu_l)(\mu_l + \nu_l) + 4\nu_l^2 \equiv 0 \pmod{d_l}, \tag{C10}$$

we have $\gcd(d_l, \mu_l - \nu_l) = \gcd(d_l, \mu_l + \nu_l) = \gcd(d_l, 2\nu_l) = 1$. It follows that the two congruences in Eq. (C9) are redundant, so we only need to solve

$$(\mu_l + \nu_l)x' + 2\nu_l y' \equiv 0 \pmod{d_l}. \tag{C11}$$

We solve this as $y' \equiv -2^{-1}\nu_l^{-1}(\mu_l + \nu_l)x' \pmod{d_l}$ where 2^{-1} is an inverse of 2 modulo d_l. The two primitive vectors for Eq. (C6) are then

$$\mathbf{u}_l^1 = (\rho_l/d_l)\big(\hat{\mathbf{x}} - 2^{-1}\nu_l^{-1}(\mu_l + \nu_l)\hat{\mathbf{y}}\big),$$
$$\mathbf{u}_l^2 = \rho_l \hat{\mathbf{y}}. \tag{C12}$$

(2) $d_l \equiv 2 \pmod 4$. In this case, $\rho_l \equiv 2 \pmod 4$ and μ_l and ν_l are both odd. Eq. (C9) simplifies to

$$\begin{pmatrix} (\mu_l + \nu_l)/2 & \nu_l \\ -\nu_l & (\mu_l - \nu_l)/2 \end{pmatrix} \begin{pmatrix} x' \\ y' \end{pmatrix} \equiv \begin{pmatrix} 0 \\ 0 \end{pmatrix} \pmod{d_l/2}. \tag{C13}$$

Since

$$(\mu_l - \nu_l)(\mu_l + \nu_l)/2 + 2\nu_l^2 \equiv 0 \pmod{d_l/2}, \tag{C14}$$

we have $\gcd(d_l/2, (\mu_l - \nu_l)/2) = \gcd(d_l/2, (\mu_l + \nu_l)/2) = \gcd(d_l/2, \nu_l) = 1$. It follows that the two congruences in Eq. (C13) are redundant, so we only need to solve

$$(\mu_l + \nu_l)x'/2 + \nu_l y' \equiv 0 \pmod{d_l/2}. \tag{C15}$$

We solve this as $y' = -\nu_l^{-1}(\mu_l + \nu_l)x'/2 \pmod{d_l/2}$. The two primitive vectors for Eq. (C6) are then

$$\mathbf{u}_l^1 = (\rho_l/d_l)\big(\hat{\mathbf{x}} - \nu_l^{-1}(\mu_l + \nu_l)\hat{\mathbf{y}}/2\big),$$
$$\mathbf{u}_l^2 = (\rho_l/2)\hat{\mathbf{y}}. \tag{C16}$$

(3) $d_l \equiv 4 \pmod 8$. In this case, $\rho_l \equiv 0 \pmod 4$ and μ_l and ν_l are both odd. Eq. (C13) holds in this case as well. Since $d_l/2$ is even and $(\mu_l + \nu_l)/2 + (\mu_l - \nu_l)/2 \equiv 1 \pmod 2$, Eq. (C13) implies that x' and y' are both even. Equation (C13) then further simplifies to

$$\begin{pmatrix} (\mu_l + \nu_l)/2 & \nu_l \\ -\nu_l & (\mu_l - \nu_l)/2 \end{pmatrix} \begin{pmatrix} x'' \\ y'' \end{pmatrix} \equiv \begin{pmatrix} 0 \\ 0 \end{pmatrix} \pmod{d_l/4} \tag{C17}$$

where $x' = 2x''$ and $y' = 2y''$. Since

$$(\mu_l - \nu_l)(\mu_l + \nu_l)/4 + \nu_l^2 \equiv 0 \pmod{d_l/4} \tag{C18}$$

we have $\gcd(d_l/4, (\mu_l - \nu_l)/2) = \gcd(d_l/4, (\mu_l + \nu_l)/2) = \gcd(d_l/4, \nu_l) = 1$. It follows that the two congruences in

Eq. (C17) are redundant and we only need to solve

$$(\mu_l + \nu_l)x''/2 + \nu_l y'' \equiv 0 \quad (\text{mod } d_l/4). \tag{C19}$$

We solve this as $y'' = -\nu_l^{-1}(\mu_l + \nu_l)x''/2 \ (\text{mod } d_l/4)$. The two primitive vectors are then

$$\mathbf{u}_l^1 = 2(\rho_l/d_l)\big(\hat{\mathbf{x}} - \nu_l^{-1}(\mu_l + \nu_l)\hat{\mathbf{y}}/2\big),$$
$$\mathbf{u}_l^2 = (\rho_l/2)\hat{\mathbf{y}}. \tag{C20}$$

Note that $\mu_l^2 + 3\nu_l^2 \not\equiv 0 \ (\text{mod } 8)$ if at least one of μ_l and ν_l is odd, so these are all the possible cases.

To summarize, $\mathbf{u}_l^1$ and $\mathbf{u}_l^2$ can be written in the form

$$\mathbf{u}_l^1 = f_l(\rho_l/d_l)(\hat{\mathbf{x}} - h_l\hat{\mathbf{y}}),$$
$$\mathbf{u}_l^2 = g_l(\rho_l/2)\hat{\mathbf{y}}, \tag{C21}$$

where

$$f_l = \begin{cases} 1 & \text{when } 4 \nmid d_l \\ 2 & \text{when } 4 | d_l \end{cases}, $$
$$g_l = \begin{cases} 1 & \text{when } 2 | d_l \\ 2 & \text{when } 2 \nmid d_l \end{cases}, \tag{C22}$$

and where h_l satisfies

$$2\nu_l h_l \equiv \mu_l + \nu_l \quad (\text{mod } d_l). \tag{C23}$$

Since $\tilde{a}\mathbf{u}_+^1$ and $\tilde{a}\mathbf{u}_+^2$ are primitive vectors for L_c, the area of the primitive unit cell Ω_c of L_c is

$$|\Omega_c| = \frac{f_+ g_+ \rho_+^2}{2d_+}|\Omega_+|. \tag{C24}$$

Similarly, since $e^\epsilon R_\theta \tilde{a}\mathbf{u}_-^1$ and $e^\epsilon R_\theta \tilde{a}\mathbf{u}_-^2$ are primitive vectors for L_c, we have

$$|\Omega_c| = \frac{f_- g_- \rho_-^2}{2d_-}|\Omega_-|. \tag{C25}$$

It follows that Ω_c contains N_l elements of L_l where

$$N_l = \frac{|\Omega_c|}{|\Omega_l|} = \frac{f_l g_l \rho_l^2}{2d_l} \tag{C26}$$

is a positive integer. Additionally,

$$\frac{N_+}{N_-} = \frac{|\Omega_-|}{|\Omega_+|} = \frac{|\text{BZ}_+|}{|\text{BZ}_-|} = e^{2\epsilon}. \tag{C27}$$

3. Primitive vectors of $P_- \cap P_+$

We will now derive the primitive vectors of $P_- \cap P_+$ when P_- and P_+ are commensurate. As in Appendix C2 we first compute the primitive vectors $\mathbf{v}_l^1$ and $\mathbf{v}_l^2$ of the Bravais lattice consisting of all integer vectors $\mathbf{v}_l$ such that

$$e^{l\epsilon}\tilde{b}^{-1}R_{-l\theta}\tilde{b}\mathbf{v}_l \in \mathbb{Z}^2. \tag{C28}$$

The primitive vectors of $P_- \cap P_+$ will then be $\tilde{b}\mathbf{v}_+^1$ and $\tilde{b}\mathbf{v}_+^2$, or alternatively $e^{-\epsilon}R_\theta \tilde{b}\mathbf{v}_-^1$ and $e^{-\epsilon}R_\theta \tilde{b}\mathbf{v}_-^2$.

Since

$$e^{l(\epsilon - i\theta)} = \frac{\mu_{-l} - \nu_{-l}i\sqrt{3}}{\rho_{-l}}, \tag{C29}$$

Eq. (C3) implies

$$e^{l\epsilon}\tilde{b}^{-1}R_{-l\theta}\tilde{b} = \frac{1}{\rho_{-l}}\begin{pmatrix} \mu_{-l} + \nu_{-l} & -2\nu_{-l} \\ 2\nu_{-l} & \mu_{-l} - \nu_{-l} \end{pmatrix}. \tag{C30}$$

By an argument similar to that in Appendix C2, we find

$$\mathbf{v}_l^1 = \mathcal{R}_{\hat{\mathbf{y}}}\mathbf{u}_{-l}^1, \quad \mathbf{v}_l^2 = \mathbf{u}_{-l}^2. \tag{C31}$$

Furthermore, each primitive unit cell of $P_- \cap P_+$ contains N_{-l} elements of P_l.

4. Commensuration reciprocal lattice

Suppose that L_- and L_+ are commensurate and let P_c be the reciprocal lattice of L_c. Since L_c is a triangular Bravais lattice, P_c is as well. Clearly, P_- and P_+ are both subsets of P_c. It follows that P_c also contains the Bravais lattice $P_- + P_+$. However, since the reciprocal lattice of $P_- + P_+$ is a subset of L_c, it follows that $P_c = P_- + P_+$. We call P_c the commensuration reciprocal lattice and we denote the Brillouin zone of P_c by BZ_c.

We can write the primitive vectors for P_c corresponding to $\tilde{a}\mathbf{u}_+^1$ and $\tilde{a}\mathbf{u}_+^2$ in the form $\tilde{b}\mathbf{u}_{c,+}^1$ and $\tilde{b}\mathbf{u}_{c,+}^2$. Similarly, we can write the primitive vectors for P_c corresponding to $e^\epsilon R_\theta \tilde{a}\mathbf{u}_-^1$ and $e^\epsilon R_\theta \tilde{a}\mathbf{u}_-^2$ in the form $e^{-\epsilon}R_\theta \tilde{b}\mathbf{u}_{c,-}^1$ and $e^{-\epsilon}R_\theta \tilde{b}\mathbf{u}_{c,-}^2$. A simple calculation shows

$$\mathbf{u}_{c,l}^1 = \frac{d_l}{f_l \rho_l}\hat{\mathbf{x}}, \quad \mathbf{u}_{c,l}^2 = \frac{2(h_l\hat{\mathbf{x}} + \hat{\mathbf{y}})}{g_l \rho_l}. \tag{C32}$$

Additionally,

$$|\text{BZ}_c| = |\text{BZ}_l|/N_l \tag{C33}$$

for $l \in \{+, -\}$.

5. Equivalence class of $\mathbf{K}_l$ modulo P_c

Note that the equivalence class of $\mathbf{K}_l$ modulo P_c is invariant under rotations by $2\pi/3$ about $\hat{\mathbf{z}}$. It follows that $\mathbf{K}_l$ is either in P_c or is equivalent to one of the two distinct corners of BZ_c. We first find the conditions under which $\mathbf{K}_l \in P_c$.

Since $\mathbf{K}_+ = \tilde{b}(2\hat{\mathbf{x}} + \hat{\mathbf{y}})/3$ and $\mathbf{K}_- = e^{-\epsilon}R_\theta \tilde{b}(2\hat{\mathbf{x}} + \hat{\mathbf{y}})/3$, it follows that $\mathbf{K}_l \in P_c$ if and only if

$$\frac{2}{3}\hat{\mathbf{x}} + \frac{1}{3}\hat{\mathbf{y}} = n_1 \mathbf{u}_{c,l}^1 + n_2 \mathbf{u}_{c,l}^2 \tag{C34}$$

for some integers n_1 and n_2. This equation can be solved for rational n_1 and n_2 as

$$n_1 = \frac{f_l \rho_l}{3d_l}(2 - h_l), \quad n_2 = \frac{g_l \rho_l}{6}. \tag{C35}$$

Since $g_l \rho_l$ is always even, $n_2 \in \mathbb{Z}$ is equivalent to $3|\rho_l$. Now suppose $3|\rho_l$ and we will show that $n_1 \in \mathbb{Z}$. If $3 \nmid d_l$ then $(3d_l)|\rho_l$ so that $n_1 \in \mathbb{Z}$. On the other hand, if $3|d_l$ then we must have $3|\mu_l$ and $3 \nmid \nu_l$. If we reduce Eq. (C23) modulo 3, we find $2\nu_l h_l \equiv \nu_l \ (\text{mod } 3)$ or $h_l \equiv 2 \ (\text{mod } 3)$. In this case we again have $n_1 \in \mathbb{Z}$. We conclude $\mathbf{K}_l \in P_c$ if and only if $3|\rho_l$.

Next, we will show that at most one of ρ_- and ρ_+ is divisible by 3. We have

$$\frac{\mu_l + \nu_l i\sqrt{3}}{\rho_l} = \left(\frac{\mu_{-l} + \nu_{-l}i\sqrt{3}}{\rho_{-l}}\right)^{-1}$$
$$= \frac{\rho_{-l}\mu_{-l} - \rho_{-l}\nu_{-l}i\sqrt{3}}{\mu_{-l}^2 + 3\nu_{-l}^2} \tag{C36}$$

and suppose that $3|\rho_{-l}$. If $3 \nmid \mu_{-l}$ then $3 \nmid (\mu_{-l}^2 + 3\nu_{-l}^2)$ and so $3 \nmid \rho_l$. On the other hand if $3|\mu_{-l}$ then $3 \nmid \nu_{-l}$ so that $9 \nmid (\mu_{-l}^2 + 3\nu_{-l}^2)$. The single factor of 3 in $\mu_{-l}^2 + 3\nu_{-l}^2$ is then canceled by that in ρ_{-l} so that again $3 \nmid \rho_l$.

Finally, we consider the case in which $3 \nmid \rho_-\rho_+$ so that $\mathbf{K}_-, \mathbf{K}_+ \notin P_c$. Since $\mathbf{K}_-$ and $\mathbf{K}_+$ are both equivalent to corners of BZ_c, we must have $\mathbf{K}_- - t\mathbf{K}_+ \in P_c$ for some $t \in \{+, -\}$, which we will now find. Using Eq. (C30), we can write

$$\mathbf{K}_- = \tilde{b}(e^{-\epsilon}\tilde{b}^{-1}R_\theta\tilde{b})(2\hat{\mathbf{x}} + \hat{\mathbf{y}})/3$$
$$= \tilde{b}(2\mu_+\hat{\mathbf{x}} + (\mu_+ + 3\nu_+)\hat{\mathbf{y}})/(3\rho_+). \quad \text{(C37)}$$

It follows that

$$\frac{2(\mu_+ - t\rho_+)}{3\rho_+}\hat{\mathbf{x}} + \frac{\mu_+ + 3\nu_+ - t\rho_+}{3\rho_+}\hat{\mathbf{y}} = n_1\mathbf{u}_{c,+}^1 + n_2\mathbf{u}_{c,+}^2 \quad \text{(C38)}$$

for some integers n_1 and n_2. Solving for n_2 gives

$$n_2 = \frac{g_+}{6}(\mu_+ + 3\nu_+ - t\rho_+). \quad \text{(C39)}$$

In particular, this implies $3|(\mu_+ - t\rho_+)$ or equivalently

$$t \equiv \mu_+\rho_+ \pmod 3. \quad \text{(C40)}$$

Note that Eq. (C36) implies that $3 \nmid \mu_+$ whenever $3 \nmid \rho_-\rho_+$, so Eq. (C40) indeed determines a valid value for t. Additionally, we can see from Eq. (C36) that

$$\mu_-\rho_- \equiv \mu_+\rho_+ \pmod 3 \quad \text{(C41)}$$

whenever $3 \nmid \rho_-\rho_+$.

We summarize the results of this section by enumerating the four possible types of commensurate configuration with regard to the equivalence classes of $\mathbf{K}_-$ and $\mathbf{K}_+$ modulo P_c.

    I+.$3 \nmid \rho_-\rho_+$ and $\mu_-\rho_- \equiv \mu_+\rho_+ \equiv 1 \pmod 3$. In this case, $\mathbf{K}_-, \mathbf{K}_+ \notin P_c$ but $\mathbf{K}_- - \mathbf{K}_+ \in P_c$.

    I−. $3 \nmid \rho_-\rho_+$ and $\mu_-\rho_- \equiv \mu_+\rho_+ \equiv -1 \pmod 3$. In this case, $\mathbf{K}_-, \mathbf{K}_+ \notin P_c$ but $\mathbf{K}_- + \mathbf{K}_+ \in P_c$.

    II+. $3 \nmid \rho_-$ and $3|\rho_+$. In this case, $\mathbf{K}_- \notin P_c$ and $\mathbf{K}_+ \in P_c$.

    II−. $3|\rho_-$ and $3 \nmid \rho_+$. In this case, $\mathbf{K}_- \in P_c$ and $\mathbf{K}_+ \notin P_c$.

APPENDIX D: MOIRÉ MODELS FOR EACH TYPE OF COMMENSURATE CONFIGURATION

In this section, we derive moiré models for each of the four types of commensurate configuration in Appendix C5. The arguments given in this section are a simple generalization of those in Ref. [41], which considered the case of TBG twisted near an arbitrary commensurate angle. See also Appendices F to H for detailed derivations of the moiré models near the configurations $\epsilon_0 = \ln\sqrt{3}$, $\theta_0 = 30°$ and $\epsilon_0 = 0$, $\theta_0 = 0$.

We consider a bilayer structure consisting of two 2D crystalline materials with triangular Bravais lattices. For simplicity, we assume that the top layer is graphene, although the following arguments apply also to other similar materials. The interatomic spacing of graphene is $a_0 \approx 0.142$ nm and the lattice constant of graphene is $a = a_0\sqrt{3} \approx 0.246$ nm. For simplicity, we choose the chemical potential so that we can regard the graphene Fermi energy as 0. As in Appendix B, the bottom layer has lattice constant $e^\epsilon a$ and is rotated counterclockwise by angle θ relative to the top layer. We take ϵ

and θ as in Eq. (1) where ϵ_0 and θ_0 are parameters for a commensurate configuration, as described in Appendix C1. We write $P_-^0 = e^{\delta\epsilon}R_{-\delta\theta}P_-$ and $\text{BZ}_-^0 = e^{\delta\epsilon}R_{-\delta\theta}\text{BZ}_-$ for the bottom layer reciprocal lattice and Brillouin zone in the commensurate case. The commensurate reciprocal lattice is $P_c = P_-^0 + P_+$ and Eq. (C33) implies

$$|\text{BZ}_c| = |\text{BZ}_+|/N_+ = |\text{BZ}_-^0|/N_- \quad \text{(D1)}$$

where BZ_c is the Brillouin zone for P_c.

We are interested in the low-energy sector of the bilayer Hamiltonian that originates from the graphene Dirac cones at the $\mathbf{K}_+$ and $-\mathbf{K}_+$ points. We assume there is some effective Slater-Koster model that describes this low-energy physics [56]. For simplicity, we neglect spin degrees of freedom for now and consider them in Appendix D5. We use Wannier functions $|\mathbf{r}, l, \alpha\rangle$ for $l \in \{+, -\}$, $\mathbf{r} \in L_l$, and $\alpha \in \mathcal{O}_l$ as a basis for our model, where $\mathcal{O}_l$ is the set of orbitals on layer l. The Wannier function $|\mathbf{r}, l, \alpha\rangle$ is localized at position $\mathbf{r} + \boldsymbol{\tau}_\alpha^l$ in the xy plane. The most important orbitals in $\mathcal{O}_+$ are the carbon p_z orbitals located on the two graphene sublattices, since these orbitals give rise to the Dirac cones [57]. We denote these orbitals by A and B and take

$$\boldsymbol{\tau}_A^+ = a_0\hat{\mathbf{y}}, \quad \boldsymbol{\tau}_B^+ = -a_0\hat{\mathbf{y}} \quad \text{(D2)}$$

following the convention in Appendix K1.

The Slater-Koster Hamiltonian takes the form

$$\langle\mathbf{r}', l', \alpha'|H_{\text{SK}}|\mathbf{r}, l, \alpha\rangle = t_{l', \alpha', l, \alpha}(\mathbf{r}' + \boldsymbol{\tau}_{\alpha'}^{l'} - \mathbf{r} - \boldsymbol{\tau}_\alpha^l) \quad \text{(D3)}$$

for some complex-valued functions $t_{l', \alpha', l, \alpha}$. We transform to momentum space by defining Bloch states

$$|\mathbf{k}, l, \alpha\rangle = \frac{1}{\sqrt{|\text{BZ}_l|}}\sum_{\mathbf{r} \in L_l} e^{i\mathbf{k}\cdot(\mathbf{r}+\boldsymbol{\tau}_\alpha^l)}|\mathbf{r}, l, \alpha\rangle. \quad \text{(D4)}$$

The interlayer coupling can then be written

$$\langle\mathbf{k}', -l, \alpha'|H_{\text{SK}}|\mathbf{k}, l, \alpha\rangle$$
$$= \sum_{\mathbf{G}_- \in P_-}\sum_{\mathbf{G}_+ \in P_+} \frac{\hat{t}_{-l, \alpha', l, \alpha}(\mathbf{k} + \mathbf{G}_l)}{\sqrt{|\Omega_-||\Omega_+|}} e^{i\boldsymbol{\tau}_{\alpha'}^{-l}\cdot\mathbf{G}_{-l}}$$
$$\times e^{-i\boldsymbol{\tau}_\alpha^l\cdot\mathbf{G}_l}\delta^2(\mathbf{k} + \mathbf{G}_l - \mathbf{k}' - \mathbf{G}_{-l}) \quad \text{(D5)}$$

where $\hat{t}_{l', \alpha', l, \alpha}$ is the Fourier transform of $t_{l', \alpha', l, \alpha}$. Note that Eq. (D5) generalizes Eq. (9) in Ref. [41].

We assume that $\hat{t}_{l', \alpha', l, \alpha}(\mathbf{Q})$ depends only on $|\mathbf{Q}|$ and decreases rapidly as $|\mathbf{Q}|$ grows. This implies that the magnitude of a term in Eq. (D5) is large when $|\mathbf{k} + \mathbf{G}_l|$ is small. By a simple generalization of the arguments in Secs. C and D of Ref. [41], H_{SK} generates a significant coupling between states at momentum $\eta\mathbf{K}_+ + \mathbf{p}$ with small $|\mathbf{p}|$ in layer $+$ and momentum $\mathbf{k}$ in layer l if one of the following two statements holds.

(1) $l = +$ and $\mathbf{k} = \eta\mathbf{k}_0 + \mathbf{p} - (e^{-\delta\epsilon}R_{\delta\theta} - 1)\eta\mathbf{Q}$ for some $\mathbf{k}_0 \in \mathbf{K}_+ + P_c$ and

$$\mathbf{Q} \in (\mathbf{K}_+ - \mathbf{k}_0 + P_+) \cap P_-^0 \quad \text{(D6)}$$

with small $|\mathbf{Q}|$.

(2) $l = -$ and $\mathbf{k} = e^{-\delta\epsilon}R_{\delta\theta}\eta\mathbf{k}_0 + \mathbf{p} - (e^{-\delta\epsilon}R_{\delta\theta} - 1)\eta\mathbf{Q}$ for some $\mathbf{k}_0 \in \mathbf{K}_+ + P_c$ and

$$\mathbf{Q} \in (\mathbf{K}_+ + P_+) \cap (\mathbf{k}_0 + P_-^0) \tag{D7}$$

with small $|\mathbf{Q}|$.

We define

$$\mathcal{S}_+ = (\mathbf{K}_+ + P_c) \cap \mathrm{BZ}_+, \quad \mathcal{S}_- = (\mathbf{K}_+ + P_c) \cap \mathrm{BZ}_-^0 \tag{D8}$$

and note that $\mathcal{S}_l$ contains N_l elements by Eq. (D1). All states in layer l relevant to the physics originating with the graphene Dirac cones have momentum near an element of $\mathcal{S}_l$.

Next, we will apply these results to derive the form of the moiré model in three cases. In each case, we will show that the Hamiltonian can be written as a direct sum of Hamiltonians of a certain canonical form. We first present this form and then proceed to the three cases.

1. Two Dirac cone moiré Hamiltonian

The canonical form for a moiré Hamiltonian with two Dirac cones is

$$H = \int d^2\mathbf{r}|\mathbf{r}\rangle\mathcal{H}(\mathbf{r})\langle\mathbf{r}|,$$

$$\mathcal{H}(\mathbf{r}) = \begin{pmatrix} S_+(\mathbf{r}) - i\hbar v_+\boldsymbol{\sigma}\cdot\nabla & T(\mathbf{r}) \\ T^\dagger(\mathbf{r}) & S_-(\mathbf{r}) - i\hbar v_-\boldsymbol{\sigma}\cdot\nabla \end{pmatrix}. \tag{D9}$$

Here, $|\mathbf{r}\rangle$ is a four-dimensional row vector of states located at position $\mathbf{r}$, $T(\mathbf{r})$ and $S_\pm(\mathbf{r})$ are 2×2 spatially varying moiré potentials, and $v_\pm$ are Fermi velocities for the two Dirac cones. The potentials can be expanded as

$$T(\mathbf{r}) = \sum_{\mathbf{q}\in P_M^+} T_\mathbf{q}e^{i\mathbf{r}\cdot\mathbf{q}}, \quad S_\pm(\mathbf{r}) = \sum_{\mathbf{q}\in P_M} S_{\pm,\mathbf{q}}e^{i\mathbf{r}\cdot\mathbf{q}}, \tag{D10}$$

for 2×2 complex matrices $T_\mathbf{q}$ and $S_{\pm,\mathbf{q}}$ with $S_{\pm,\mathbf{q}}^\dagger = S_{\pm,-\mathbf{q}}$. The moiré reciprocal lattice P_M is given by

$$P_M = \{n_1\mathbf{q}_1 + n_2\mathbf{q}_2 + n_3\mathbf{q}_3 | n_1, n_2, n_3 \in \mathbb{Z}, n_1 + n_2 + n_3 = 0\}, \tag{D11}$$

and

$$P_M^+ = \mathbf{q}_1 + P_M = \mathbf{q}_2 + P_M = \mathbf{q}_3 + P_M. \tag{D12}$$

The $\mathbf{q}_1$, $\mathbf{q}_2$, and $\mathbf{q}_3$ vectors are defined by

$$\mathbf{q}_j = (e^{-\delta\epsilon}R_{\delta\theta} - 1)R_{\xi_0+\zeta_j}\sqrt{N_-}\mathbf{K}_+ \tag{D13}$$

where $\zeta_j = \frac{2\pi}{3}(j - 1)$, ξ_0 is an angle, and N_- is the number of bottom layer Bravais lattice sites in each commensurate unit cell for the configuration with parameters ϵ_0 and θ_0 (see Appendix C 2). The magnitudes of the $T_\mathbf{q}$ and $S_{\pm,\mathbf{q}}$ matrices typically decay rapidly with $|\mathbf{q}|$, which allows us to truncate the infinite sums in Eq. (D10). We use a straightforward generalization of the method described in Appendix M of Ref. [41] to compute band structures of H in the moiré Brillouin zone BZ_M, which is defined as the Wigner-Seitz unit cell of P_M.

2. Type I± with bottom layer Dirac cones

We first suppose that the commensurate configuration with parameters ϵ_0 and θ_0 is of type Ix for $x \in \{+, -\}$. We define $\mathbf{K}_-^0 = e^{\delta\epsilon}R_{-\delta\theta}\mathbf{K}_-$ so that $x\mathbf{K}_-^0 \in \mathcal{S}_-$. Note that the graphene layer has a Dirac cone at $\mathbf{K}_+$ at 0 energy and a large gap around 0 at all other momenta in $\mathcal{S}_+$. We assume that the bottom layer has a Dirac cone at $x\mathbf{K}_-$ near 0 energy and a large gap around 0 at all other momenta in $e^{-\delta\epsilon}R_{\delta\theta}\mathcal{S}_-$. The low-energy physics associated with the graphene Dirac cones is then described by an effective continuum model involving only top layer momenta near $\mathbf{K}_+$ and $-\mathbf{K}_+$ and bottom layer momenta near $\mathbf{K}_-$ and $-\mathbf{K}_-$. Furthermore, the model has two decoupled valleys, one of which contains $\mathbf{K}_+$ and $x\mathbf{K}_-$ and the other of which contains $-\mathbf{K}_+$ and $-x\mathbf{K}_-$. For simplicity, we focus on the valley containing $\mathbf{K}_+$ and $x\mathbf{K}_-$.

We introduce continuum states $|\mathbf{p}, l, \alpha\rangle$ for $\mathbf{p} \in \mathbb{R}^2$, $l \in \{+, -\}$, and $\alpha \in \{A, B\}$, which satisfy the normalization condition

$$\langle\mathbf{p}', l', \alpha'|\mathbf{p}, l, \alpha\rangle = \delta^2(\mathbf{p}' - \mathbf{p})\delta_{l',l}\delta_{\alpha',\alpha}. \tag{D14}$$

The continuum state $|\mathbf{p}, +, \alpha\rangle$ represents the Bloch state $|\mathbf{K}_+ + \mathbf{p}, +, \alpha\rangle$ so that the Dirac cone at $\mathbf{K}_+$ takes the form

$$\int d^2\mathbf{p}(|\mathbf{p}, +, A\rangle \quad |\mathbf{p}, +, B\rangle)(\hbar v_+\boldsymbol{\sigma}\cdot\mathbf{p})\begin{pmatrix}\langle\mathbf{p}, +, A| \\ \langle\mathbf{p}, +, B|\end{pmatrix} \tag{D15}$$

where v_+ is the graphene Fermi velocity. The continuum states $|\mathbf{p}, -, A\rangle$ and $|\mathbf{p}, -, B\rangle$ represent appropriate linear combinations of bottom layer Bloch states with momenta $x\mathbf{K}_- + \mathbf{p}$ such that the Dirac cone at $x\mathbf{K}_-$ takes the form

$$\int d^2\mathbf{p}(|\mathbf{p}, -, A\rangle \quad |\mathbf{p}, -, B\rangle)(E_- + \hbar v_-\boldsymbol{\sigma}\cdot\mathbf{p})\begin{pmatrix}\langle\mathbf{p}, -, A| \\ \langle\mathbf{p}, -, B|\end{pmatrix} \tag{D16}$$

where v_- is the bottom layer Fermi velocity and E_- is a small energy offset. Note that a Dirac cone in two dimensions with any rotation angle or helicity is related to one of the form $\hbar v\boldsymbol{\sigma}\cdot\mathbf{p}$ by a unitary transformation, so one can always choose $|\mathbf{p}, -, A\rangle$ and $|\mathbf{p}, -, B\rangle$ to satisfy this requirement.

If we group the continuum states with momentum $\mathbf{p}$ into a row vector

$$|\mathbf{p}\rangle = (|\mathbf{p}, +, A\rangle|\mathbf{p}, +, B\rangle \quad |\mathbf{p}, -, A\rangle|\mathbf{p}, -, B\rangle), \tag{D17}$$

the effective Hamiltonian can be written in the form

$$H = \int d^2\mathbf{p}'d^2\mathbf{p}|\mathbf{p}'\rangle\mathcal{H}(\mathbf{p}', \mathbf{p})\langle\mathbf{p}|$$

$$\mathcal{H}(\mathbf{p}', \mathbf{p}) = \begin{pmatrix}\hbar v_+\boldsymbol{\sigma}\cdot\mathbf{p} & 0 \\ 0 & \hbar v_-\boldsymbol{\sigma}\cdot\mathbf{p}\end{pmatrix}\delta^2(\mathbf{p}' - \mathbf{p})$$

$$+ \sum_{\mathbf{q}\in P_M^+}\begin{pmatrix}0 & T_\mathbf{q} \\ 0 & 0\end{pmatrix}\delta^2(\mathbf{p}' - \mathbf{p} - \mathbf{q})$$

$$+ \sum_{\mathbf{q}\in P_M^+}\begin{pmatrix}0 & 0 \\ T_\mathbf{q}^\dagger & 0\end{pmatrix}\delta^2(\mathbf{p}' - \mathbf{p} + \mathbf{q})$$

$$+ \sum_{\mathbf{q}\in P_M}\begin{pmatrix}S_{+,\mathbf{q}} & 0 \\ 0 & S_{-,\mathbf{q}}\end{pmatrix}\delta^2(\mathbf{p}' - \mathbf{p} - \mathbf{q}) \tag{D18}$$

where

$$P_M = (e^{-\delta\epsilon}R_{\delta\theta} - 1)(P_+ \cap P_-^0), \tag{D19}$$

$$P_M^+ = (e^{-\delta\epsilon}R_{\delta\theta} - 1)((\mathbf{K}_+ + P_+) \cap (x\mathbf{K}_-^0 + P_-^0)). \tag{D20}$$

$T_{\mathbf{q}}$ and $S_{\mathbf{q}}^{\pm}$ denote complex 2×2 matrices with norms that generally decrease as $|\mathbf{q}|$ increases. The values of these matrices include contributions from states with momenta near values in $\mathcal{S}_+$ or $e^{-\delta\epsilon}R_{\delta\theta}\mathcal{S}_-$, which are not explicitly included in the effective Hamiltonian.

By the results of Appendix C 3, $P_+ \cap P_-^0$ is a triangular Bravais lattice with a unit cell N_- times larger than that of P_+. Furthermore, $(\mathbf{K}_+ + P_+) \cap (x\mathbf{K}_-^0 + P_-^0)$ can be written in the form $\mathbf{v} + P_+ \cap P_-^0$ for some nonzero vector $\mathbf{v}$ such that $R_{2\pi/3}\mathbf{v} - \mathbf{v} \in P_+ \cap P_-^0$. It follows that there is some angle ξ_0 such that

$$P_+ \cap P_-^0 = R_{\xi_0}\sqrt{N_-}P_+,$$

$$(\mathbf{K}_+ + P_+) \cap (x\mathbf{K}_-^0 + P_-^0) = R_{\xi_0}\sqrt{N_-}(\mathbf{K}_+ + P_+). \tag{D21}$$

We then have

$$P_M = (e^{-\delta\epsilon}R_{\delta\theta} - 1)R_{\xi_0}\sqrt{N_-}P_+,$$

$$P_M^+ = (e^{-\delta\epsilon}R_{\delta\theta} - 1)R_{\xi_0}\sqrt{N_-}(\mathbf{K}_+ + P_+), \tag{D22}$$

which is equivalent to Eqs. (D11) to (D13). As an example, when $\epsilon_0 = 0$, $\theta_0 = 0$ we have $N_- = 1$ and one can take $\xi_0 = 0$. This particular case will be discussed further in Appendix H.

Finally, we introduce real-space continuum states

$$|\mathbf{r}, l, \alpha\rangle = \frac{1}{2\pi} \int d^2\mathbf{p}\, e^{-i\mathbf{p}\cdot\mathbf{r}}|\mathbf{p}, l, \alpha\rangle, \tag{D23}$$

which satisfy the normalization condition

$$\langle\mathbf{r}', l', \alpha'|\mathbf{r}, l, \alpha\rangle = \delta^2(\mathbf{r}' - \mathbf{r})\delta_{l',l}\delta_{\alpha',\alpha}. \tag{D24}$$

If we group the continuum states with position $\mathbf{r}$ into a row vector

$$|\mathbf{r}\rangle = (|\mathbf{r}, +, A\rangle|\mathbf{r}, +, B\rangle \quad |\mathbf{r}, -, A\rangle|\mathbf{r}, -, B\rangle), \tag{D25}$$

the Hamiltonian takes the form of Eq. (D9) with $T(\mathbf{r})$ and $S_{\pm}(\mathbf{r})$ potentials given by Eq. (D10).

We conclude that the moiré model for the valley containing $\mathbf{K}_+$ and $x\mathbf{K}_-$ is of the form in Appendix D 1 with the two Dirac cones coming from opposite layers. By a similar argument, the Hamiltonian for the valley containing $-\mathbf{K}_+$ and $-x\mathbf{K}_-$ also takes this form, although the ξ_0 angles for the two valleys differ by π.

3. Type I± or II− with gapped bottom layer

Next, suppose that the commensurate configuration with parameters ϵ_0 and θ_0 is of type I+, I−, or II−. This is equivalent to the requirement that $\mathbf{K}_+ \notin P_c$. In contrast to Appendix D 2, we assume that the bottom layer has a large gap around 0 at all momenta in $e^{-\delta\epsilon}R_{\delta\theta}\mathcal{S}_-$. In this case, the low-energy physics associated with the graphene Dirac cones is described by an effective continuum model involving only top layer momenta near $\mathbf{K}_+$ and $-\mathbf{K}_+$. Furthermore, the model has two decoupled valleys, one of which contains $\mathbf{K}_+$ and the other of which contains $-\mathbf{K}_+$. Following a similar argument

to that in Appendix D 2, we find that the moiré model for both valleys can be written in the form described in Appendix D 1 with $T(\mathbf{r}) = 0$. In this case, the two Dirac cones correspond to the two graphene valleys, $v_+ = v_-$, and the angle ξ_0 is constrained only by

$$P_+ \cap P_-^0 = R_{\xi_0}\sqrt{N_-}P_+. \tag{D26}$$

4. Type II+ with gapped bottom layer

Finally, suppose that the commensurate configuration with parameters ϵ_0 and θ_0 is of type II+ so that $-\mathbf{K}_+ \in \mathcal{S}_+$. As in Appendix D 3, we assume that the bottom layer has a large gap around 0 at all momenta in $e^{-\delta\epsilon}R_{\delta\theta}\mathcal{S}_-$. In this case, the low-energy physics associated with the graphene Dirac cones is described by an effective continuum model involving only top layer momenta near $\mathbf{K}_+$ and $-\mathbf{K}_+$. In contrast to Appendices D 2 and D 3, the model has only one valley so there is no degree of freedom associated with valley. Following a similar argument to that in Appendix D 2, we find that the moiré model can be written in the form described in Appendix D 1. In this case, the two Dirac cones correspond to the two graphene valleys so that $v_+ = v_-$. Additionally, although Eq. (D19) still holds, Eq. (D20) is modified to

$$P_M^+ = (e^{-\delta\epsilon}R_{\delta\theta} - 1)((\mathbf{K}_+ - (-\mathbf{K}_+) + P_+) \cap P_-^0)$$

$$= (e^{-\delta\epsilon}R_{\delta\theta} - 1)((-\mathbf{K}_+ + P_+) \cap P_-^0). \tag{D27}$$

As a result, the angle ξ_0 is now constrained by

$$P_+ \cap P_-^0 = R_{\xi_0}\sqrt{N_-}P_+,$$

$$(-\mathbf{K}_+ + P_+) \cap P_-^0 = R_{\xi_0}\sqrt{N_-}(\mathbf{K}_+ + P_+). \tag{D28}$$

As an example, when $\epsilon_0 = \ln\sqrt{3}$, $\theta_0 = 30°$ we have $N_- = 1$ and one can take $\xi_0 = \pi$. This particular case will be discussed further in Appendices F and G.

5. Including spin

So far in Appendix D we have neglected spin degrees of freedom. In each case, if both layers have negligible spin-orbit coupling, the system can be described as a direct sum of two copies of the spinless model, one for spin $\uparrow$ and the other for spin $\downarrow$. If there is significant spin-orbit coupling (but the Dirac cones remain unchanged), the two spinless models can have different parameters and can be coupled together. In this paper, we will focus on cases in which the z component of spin is preserved. In that case, the two spinless models can have different parameters but will not be coupled. If the system has time-reversal symmetry, the Hamiltonians for the two spins will be related by time-reversal. This is explained in more detail in Appendix G for the case in which $\epsilon_0 = \ln\sqrt{3}$, $\theta_0 = 30°$.

APPENDIX E: MOIRÉ COORDINATE SYSTEM

In order to make the Hamiltonian in Appendix D 1 more closely resemble the BM model for small angle TBG, we will define a coordinate system x_M, y_M in which $\mathbf{q}_1$ is on the positive y_M axis. Let

$$\xi = \arg(e^{-\delta\epsilon+i\delta\theta} - 1) + \xi_0 - \pi/2 \tag{E1}$$

and

$$\hat{\mathbf{x}}_M = R_\xi \hat{\mathbf{x}}, \quad \hat{\mathbf{y}}_M = R_\xi \hat{\mathbf{y}}. \tag{E2}$$

Note that $\mathbf{q}_1 = |\mathbf{q}_1|\hat{\mathbf{y}}_M$ and $\hat{\mathbf{x}}_M \times \hat{\mathbf{y}}_M = \hat{\mathbf{z}}$. We refer to the coordinate system x_M, y_M defined by $\hat{\mathbf{x}}_M$ and $\hat{\mathbf{y}}_M$ as the moiré coordinate system and illustrate it in Figs. 1(d) and 1(e).

Note that

$$\boldsymbol{\sigma} = e^{-i(\xi/2)\sigma_z} \boldsymbol{\sigma}_M e^{i(\xi/2)\sigma_z} \tag{E3}$$

where $\boldsymbol{\sigma}_M = \sigma_x \hat{\mathbf{x}}_M + \sigma_y \hat{\mathbf{y}}_M$. Applying the unitary change of basis

$$|\mathbf{r}\rangle_\xi = |\mathbf{r}\rangle \sigma_0 \otimes e^{-i(\xi/2)\sigma_z}, \tag{E4}$$

Eq. (D9) can be rewritten

$$H = \int d^2\mathbf{r}|\mathbf{r}\rangle_\xi \mathcal{H}_\xi(\mathbf{r})\langle\mathbf{r}|_\xi,$$

$$\mathcal{H}_\xi(\mathbf{r}) = (\sigma_0 \otimes e^{i(\xi/2)\sigma_z})\mathcal{H}(\mathbf{r})(\sigma_0 \otimes e^{-i(\xi/2)\sigma_z})$$

$$= \begin{pmatrix} S_{\xi,+}(\mathbf{r}) - i\hbar v_+ \boldsymbol{\sigma}_M \cdot \nabla & T_\xi(\mathbf{r}) \\ T_\xi^\dagger(\mathbf{r}) & S_{\xi,-}(\mathbf{r}) - i\hbar v_- \boldsymbol{\sigma}_M \cdot \nabla \end{pmatrix}. \tag{E5}$$

The $T_\xi(\mathbf{r})$ and $S_\xi^\pm(\mathbf{r})$ potentials are given by

$$T_\xi(\mathbf{r}) = e^{i(\xi/2)\sigma_z}T(\mathbf{r})e^{-i(\xi/2)\sigma_z} = \sum_{\mathbf{q}\in P_M^+} T_{\xi,\mathbf{q}}e^{i\mathbf{r}\cdot\mathbf{q}},$$

$$S_{\xi,\pm}(\mathbf{r}) = e^{i(\xi/2)\sigma_z}S_\pm(\mathbf{r})e^{-i(\xi/2)\sigma_z} = \sum_{\mathbf{q}\in P_M} S_{\xi,\pm,\mathbf{q}}e^{i\mathbf{r}\cdot\mathbf{q}}, \tag{E6}$$

with

$$T_{\xi,\mathbf{q}} = e^{i(\xi/2)\sigma_z}T_\mathbf{q}e^{-i(\xi/2)\sigma_z},$$

$$S_{\xi,\pm,\mathbf{q}} = e^{i(\xi/2)\sigma_z}S_{\pm,\mathbf{q}}e^{-i(\xi/2)\sigma_z}. \tag{E7}$$

We have now expressed the Hamiltonian in the moiré coordinate system. All models and figures in the main text use this transformation.

APPENDIX F: COUPLED-VALLEY GRAPHENE MODEL WITHOUT SPIN

We follow the construction of Appendix D for a bilayer structure in which the top layer is graphene and the bottom layer is some other 2D crystalline material with a triangular Bravais lattice. In this section, we focus on moiré patterns near the second commensurate configuration in Table II, which is type II+ and has $\epsilon_0 = \ln\sqrt{3}, \theta_0 = 30°$. For this configuration, we have $N_+ = 3$ and $N_- = 1$, so that the sets $\mathcal{S}_\pm$ defined in Eq. (D8) are given by

$$\mathcal{S}_+ = \{\mathbf{K}_+, -\mathbf{K}_+, \mathbf{\Gamma}_+\}, \quad \mathcal{S}_- = \{\mathbf{\Gamma}_-\}. \tag{F1}$$

As in Appendix D 4, we assume that the bottom layer has a gap around 0 at $\mathbf{\Gamma}_-$ so that the low-energy physics is described by a moiré model of the form in Appendix D 1 where the two Dirac cones correspond to the two graphene valleys. In this Appendix, we start with a moiré model involving degrees of freedom in both layers. We then use second-order Schrieffer-Wolff perturbation theory [58,59] to find an explicit form for

the graphene moiré model. Finally, we use symmetry and corepresentation theory to constrain the model parameters. We neglect spin degrees of freedom in this section and consider them in Appendix G.

1. Continuum Hamiltonian

When $\delta\epsilon = \delta\theta = 0$, the delta function in Eq. (D5) ensures that the only bottom layer momentum that is coupled to $\mathbf{k} = \eta\mathbf{K}_+ + \mathbf{p}$ is $\mathbf{k}' = \mathbf{\Gamma}_- + \mathbf{p}$, where $\eta \in \{+, -\}$ denotes the two graphene valleys. However, when $\delta\epsilon$ and $\delta\theta$ are not both zero, it is possible to couple a top layer state with momentum $\mathbf{k} = \eta\mathbf{K}_+ + \mathbf{p}$ to a bottom layer state with momentum $\mathbf{k}' = \mathbf{\Gamma}_- + \mathbf{p}'$ as long as

$$\mathbf{k} + \mathbf{G}_+ = \mathbf{k}' + \mathbf{G}_- \tag{F2}$$

for some $\mathbf{G}_- \in P_-$ and $\mathbf{G}_+ \in P_+$. As in Appendix D, we assume that $\hat{t}_{l',\alpha',l,\alpha}(\mathbf{Q})$ depends only on $|\mathbf{Q}|$ and decays rapidly as $|\mathbf{Q}|$ grows. It is then sufficient to consider only terms in Eq. (D5) for which $|\mathbf{k} + \mathbf{G}_+|$ is small. For small $|\mathbf{p}|$, the dominant terms are those with

$$\mathbf{G}_+ = \eta(R_{\zeta_j} - 1)\mathbf{K}_+,$$

$$e^{\delta\epsilon}R_{-\delta\theta}\mathbf{G}_- = \eta R_{\zeta_j}\mathbf{K}_+, \tag{F3}$$

where $\zeta_j = \frac{2\pi}{3}(j - 1)$. For these terms, we have

$$\mathbf{p}' = \mathbf{p} + \eta\mathbf{q}_j, \quad \mathbf{q}_j = R_{\zeta_j}(1 - e^{-\delta\epsilon}R_{\delta\theta})\mathbf{K}_+. \tag{F4}$$

Recall from Appendix D 4 that for $\epsilon_0 = \ln\sqrt{3}, \theta_0 = 30°$ we can take $\xi_0 = \pi$. Since additionally we have $N_- = 1$, the definition of $\mathbf{q}_j$ in Eq. (F4) is consistent with Eq. (D13).

With this motivation, we now introduce a continuum model that describes the low-energy physics of the bilayer system associated with the graphene Dirac cones. We define continuum states $|\mathbf{p}, \eta, \alpha\rangle_c$ for $\mathbf{p} \in \mathbb{R}^2$, $\eta \in \{+, 0, -\}$, and $\alpha \in \mathcal{O}_l$ where $l = +$ when $\eta \in \{+, -\}$ and $l = -$ when $\eta = 0$. The state $|\mathbf{p}, \eta, \alpha\rangle_c$ represents the Bloch state $|\eta\mathbf{K}_+ + \mathbf{p}, l, \alpha\rangle$ for small $\mathbf{p}$, and the continuum states satisfy the normalization condition

$$\langle\mathbf{p}', \eta', \alpha'|_c\mathbf{p}, \eta, \alpha\rangle_c = \delta^2(\mathbf{p}' - \mathbf{p})\delta_{\eta',\eta}\delta_{\alpha',\alpha}. \tag{F5}$$

We group the continuum states with momentum $\mathbf{p}$ into a row vector

$$|\mathbf{p}\rangle_c = (|\mathbf{p}, +, A\rangle_c \quad |\mathbf{p}, +, B\rangle_c \quad |\mathbf{p}, -, A\rangle_c \quad |\mathbf{p}, -, B\rangle_c$$

$$\times |\mathbf{p}, 0, \alpha_1\rangle_c \quad \cdots \quad |\mathbf{p}, 0, \alpha_n\rangle_c) \tag{F6}$$

where $\mathcal{O}_- = \{\alpha_1, \ldots, \alpha_n\}$ is an index set for the orbitals on the bottom layer. The continuum Hamiltonian then takes the form

$$H_c = \int d^2\mathbf{p}'d^2\mathbf{p}|\mathbf{p}'\rangle_c\mathcal{H}_c(\mathbf{p}', \mathbf{p})\langle\mathbf{p}|_c,$$

$$\mathcal{H}_c(\mathbf{p}', \mathbf{p}) = \begin{pmatrix} \hbar v_F\boldsymbol{\sigma}\cdot\mathbf{p} & 0 & 0 \\ 0 & -\hbar v_F\boldsymbol{\sigma}^*\cdot\mathbf{p} & 0 \\ 0 & 0 & \mathcal{H}_- \end{pmatrix}\delta^2(\mathbf{p}' - \mathbf{p})$$

$$+ \sum_{j=1}^3 \begin{pmatrix} 0 & 0 & 0 \\ 0 & 0 & T_{-,\mathbf{q}_j} \\ T_{+,\mathbf{q}_j}^\dagger & 0 & 0 \end{pmatrix}\delta^2(\mathbf{p}' - \mathbf{p} - \mathbf{q}_j)$$

$$+ \sum_{j=1}^{3} \begin{pmatrix} 0 & 0 & T_{+,\mathbf{q}_j} \\ 0 & 0 & 0 \\ 0 & T_{-,\mathbf{q}_j}^{\dagger} & 0 \end{pmatrix} \delta^2(\mathbf{p}' - \mathbf{p} + \mathbf{q}_j).$$

$$\text{(F7)}$$

Here, v_F is the graphene Fermi velocity and $\mathcal{H}_-$ is the $n \times n$ Hamiltonian for the bottom layer at the $\mathbf{\Gamma}_-$ point, which we approximate as independent of momentum. The $T_{\eta,\mathbf{q}_j}$ are $2 \times n$ complex matrices describing the coupling between valley η of graphene and $\mathcal{H}_-$.

We can write the continuum Hamiltonian in a simpler form by transforming to real space. We define real-space continuum states

$$|\mathbf{r}, \eta, \alpha\rangle_c = \frac{1}{2\pi} \int d^2\mathbf{p} \, e^{-i\mathbf{p}\cdot\mathbf{r}} |\mathbf{p}, \eta, \alpha\rangle_c, \qquad \text{(F8)}$$

which satisfy

$$\langle \mathbf{r}', \eta', \alpha' |_c \mathbf{r}, \eta, \alpha \rangle = \delta^2(\mathbf{r}' - \mathbf{r})\delta_{\eta',\eta}\delta_{\alpha',\alpha} \qquad \text{(F9)}$$

and group them into a row vector

$$|\mathbf{r}\rangle_c = (|\mathbf{r}, +, A\rangle_c \quad |\mathbf{r}, +, B\rangle_c \quad |\mathbf{r}, -, A\rangle_c \quad |\mathbf{r}, -, B\rangle_c$$
$$\times |\mathbf{r}, 0, \alpha_1\rangle_c \quad \cdots \quad |\mathbf{r}, 0, \alpha_n\rangle_c). \qquad \text{(F10)}$$

The continuum Hamiltonian then becomes

$$H_c = \int d^2\mathbf{r} |\mathbf{r}\rangle_c \mathcal{H}_c(\mathbf{r}) \langle \mathbf{r}|_c$$

$$\mathcal{H}_c(\mathbf{r}) = \begin{pmatrix} -i\hbar v_F \boldsymbol{\sigma} \cdot \nabla & 0 & T_+(\mathbf{r}) \\ 0 & i\hbar v_F \boldsymbol{\sigma}^* \cdot \nabla & T_-(\mathbf{r}) \\ T_+^{\dagger}(\mathbf{r}) & T_-^{\dagger}(\mathbf{r}) & \mathcal{H}_- \end{pmatrix}$$

$$T_\eta(\mathbf{r}) = \sum_{j=1}^{3} T_{\eta,\mathbf{q}_j} e^{-i\eta \mathbf{r} \cdot \mathbf{q}_j}. \qquad \text{(F11)}$$

Assuming that the spectrum of $\mathcal{H}_-$ has a sufficiently large gap around 0, we can treat the bottom layer states perturbatively. Applying Schrieffer-Wolff perturbation theory [58,59] to second order in the interlayer couplings and neglecting the graphene energies, we find the effective Hamiltonian for the graphene degrees of freedom

$$H_g = \int d^2\mathbf{r} |\mathbf{r}\rangle_g \mathcal{H}_g(\mathbf{r}) \langle \mathbf{r}|_g$$

$$\mathcal{H}_g(\mathbf{r}) = \begin{pmatrix} -i\hbar v_F \boldsymbol{\sigma} \cdot \nabla & 0 \\ 0 & i\hbar v_F \boldsymbol{\sigma}^* \cdot \nabla \end{pmatrix}$$
$$- \begin{pmatrix} T_+(\mathbf{r}) \\ T_-(\mathbf{r}) \end{pmatrix} \mathcal{H}_-^{-1} (T_+^{\dagger}(\mathbf{r}) \quad T_-^{\dagger}(\mathbf{r}))$$

$$|\mathbf{r}\rangle_g = (|\mathbf{r}, +, A\rangle_c \quad |\mathbf{r}, +, B\rangle_c \quad |\mathbf{r}, -, A\rangle_c \quad |\mathbf{r}, -, B\rangle_c).$$

$$\text{(F12)}$$

Finally, we take a unitary change of basis to bring the model into a form with two Dirac cones of the same helicity. To do so, we define new states $|\mathbf{r}\rangle$ by applying a σ_y transformation to the sublattice degree of freedom in the $\eta = -$ valley. Specifically, we take

$$|\mathbf{r}\rangle = |\mathbf{r}\rangle_g U_0 \quad \text{where } U_0 = \begin{pmatrix} \sigma_0 & 0 \\ 0 & \sigma_y \end{pmatrix}. \qquad \text{(F13)}$$

We then have

$$H_g = \int d^2\mathbf{r} |\mathbf{r}\rangle \mathcal{H}(\mathbf{r}) \langle \mathbf{r}|$$

$$\mathcal{H}(\mathbf{r}) = \begin{pmatrix} S_+(\mathbf{r}) - i\hbar v_F \boldsymbol{\sigma} \cdot \nabla & T(\mathbf{r}) \\ T^{\dagger}(\mathbf{r}) & S_-(\mathbf{r}) - i\hbar v_F \boldsymbol{\sigma} \cdot \nabla \end{pmatrix} \quad \text{(F14)}$$

which is of the form in Eq. (D9) with $v_+ = v_- = v_F$. The $T(\mathbf{r})$ and $S_\eta(\mathbf{r})$ potentials are given by

$$T(\mathbf{r}) = -T_+(\mathbf{r})\mathcal{H}_-^{-1}T_-^{\dagger}(\mathbf{r})\sigma_y,$$
$$S_+(\mathbf{r}) = -T_+(\mathbf{r})\mathcal{H}_-^{-1}T_+^{\dagger}(\mathbf{r}),$$
$$S_-(\mathbf{r}) = -\sigma_y T_-(\mathbf{r})\mathcal{H}_-^{-1}T_-^{\dagger}(\mathbf{r})\sigma_y. \qquad \text{(F15)}$$

Note that these potentials can be expanded in the form given by Eq. (D10). However, in this case all $T_\mathbf{q}$ and $S_{\pm,\mathbf{q}}$ matrices vanish except for those of the form

$$T_{\mathbf{q}_j}, \quad T_{-2\mathbf{q}_j}, \quad S_{\pm,\mathbf{q}_j - \mathbf{q}_k}. \qquad \text{(F16)}$$

Finally, it is worth noting that bottom layer states near $\mathbf{\Gamma}_-$ are coupled to top layer states near $\mathbf{\Gamma}_+$ in addition to top layer states near $\mathbf{K}_+$ and $-\mathbf{K}_+$. This is clear from Eq. (D5) as well as from Eq. (F1). As a result, in principle one should also include top layer states near $\mathbf{\Gamma}_+$ in Eq. (F7). However, since these states all have large energies and are not directly coupled to the graphene Dirac cones, they make no contribution to a low-energy model derived using second-order Schrieffer-Wolff perturbation theory. For this reason, we only consider top layer states near $\mathbf{K}_+$ and $-\mathbf{K}_+$ and bottom layer states near $\mathbf{\Gamma}_-$.

2. Symmetry constraints

We now consider the nontranslational symmetries of the Hamiltonian in Eq. (F14). The possible crystalline symmetry generators are C_{3z} (rotation by angle $2\pi/3$ about $\hat{\mathbf{z}}$), C_{2z} (rotation by angle π about $\hat{\mathbf{z}}$), M_x (reflection through the yz plane), and M_y (reflection through the xz plane). Additionally, we consider the antiunitary time-reversal symmetry $\mathcal{T}$, which satisfies $\mathcal{T}^2 = 1$. By considering the action of these symmetries on the graphene Wannier functions and Bloch states, we can deduce the appropriate definitions for the symmetry operators on the states $|\mathbf{r}\rangle_g$ in Eq. (F12). We define

$$C_{3z}|\mathbf{r}\rangle_g = |R_{2\pi/3}\mathbf{r}\rangle_g e^{i(2\pi/3)\sigma_z \otimes \sigma_z},$$
$$C_{2z}|\mathbf{r}\rangle_g = |-\mathbf{r}\rangle_g \sigma_x \otimes \sigma_x,$$
$$M_x|\mathbf{r}\rangle_g = |\mathcal{R}_{\hat{\mathbf{x}}}\mathbf{r}\rangle_g \sigma_x \otimes \sigma_0,$$
$$M_y|\mathbf{r}\rangle_g = |\mathcal{R}_{\hat{\mathbf{y}}}\mathbf{r}\rangle_g \sigma_0 \otimes \sigma_x,$$
$$\mathcal{T}|\mathbf{r}\rangle_g = |\mathbf{r}\rangle_g \sigma_x \otimes \sigma_0. \qquad \text{(F17)}$$

Here, the first (second) Pauli matrix in each tensor product acts on valley (sublattice). These operators can also be written in terms of the $|\mathbf{r}\rangle$ states in Eq. (F13) as

$$C_{3z}|\mathbf{r}\rangle = |R_{2\pi/3}\mathbf{r}\rangle \sigma_0 \otimes e^{i(2\pi/3)\sigma_z},$$
$$C_{2z}|\mathbf{r}\rangle = -|-\mathbf{r}\rangle \sigma_y \otimes \sigma_z,$$
$$M_x|\mathbf{r}\rangle = |\mathcal{R}_{\hat{\mathbf{x}}}\mathbf{r}\rangle \sigma_x \otimes \sigma_y,$$

$$M_y|\mathbf{r}\rangle = |\mathcal{R}_{\hat{\mathbf{y}}}\mathbf{r}\rangle\sigma_z \otimes \sigma_x,$$
$$\mathcal{T}|\mathbf{r}\rangle = -i|\mathbf{r}\rangle\sigma_y \otimes \sigma_y. \qquad (F18)$$

Suppose that U is a unitary or antiunitary symmetry, which acts as $U|\mathbf{r}\rangle = |\mathcal{O}\mathbf{r}\rangle M$ for an orthogonal matrix $\mathcal{O}$ and a unitary matrix M. Then $[U, H_g] = 0$ is equivalent to $\mathcal{H}(\mathcal{O}\mathbf{r}) = M\mathcal{H}(\mathbf{r})M^\dagger$ in the unitary case and $\mathcal{H}(\mathcal{O}\mathbf{r}) = M\mathcal{H}^*(\mathbf{r})M^\dagger$ in the antiunitary case. Applying this to the symmetry generators gives the following constraints on the $T_\mathbf{q}$ and $S_\mathbf{q}^\eta$ matrices defined by Eq. (D10):

$$[C_{3z}, H_g] = 0 \iff T_{R_{2\pi/3}\mathbf{q}} = e^{i(2\pi/3)\sigma_z}T_\mathbf{q}e^{-i(2\pi/3)\sigma_z} \quad \text{and}$$
$$S_{\eta, R_{2\pi/3}\mathbf{q}} = e^{i(2\pi/3)\sigma_z}S_{\eta,\mathbf{q}}e^{-i(2\pi/3)\sigma_z},$$
$$[C_{2z}, H_g] = 0 \iff T_\mathbf{q} = -\sigma_z T_\mathbf{q}^\dagger\sigma_z \quad \text{and}$$
$$S_{+,-\mathbf{q}} = \sigma_z S_{-,\mathbf{q}}\sigma_z,$$
$$[M_x, H_g] = 0 \iff T_{\mathcal{R}_{\hat{\mathbf{y}}}\mathbf{q}} = \sigma_y T_\mathbf{q}^\dagger\sigma_y \quad \text{and}$$
$$S_{+,\mathcal{R}_{\hat{\mathbf{y}}}\mathbf{q}} = \sigma_y S_{-,-\mathbf{q}}\sigma_y,$$
$$[M_y, H_g] = 0 \iff T_{\mathcal{R}_{\hat{\mathbf{y}}}\mathbf{q}} = -\sigma_x T_\mathbf{q}\sigma_x \quad \text{and}$$
$$S_{\eta, \mathcal{R}_{\hat{\mathbf{y}}}\mathbf{q}} = \sigma_x S_{\eta,\mathbf{q}}\sigma_x,$$
$$[\mathcal{T}, H_g] = 0 \iff T_\mathbf{q} = -\sigma_y T_\mathbf{q}^T\sigma_y \quad \text{and}$$
$$S_{+,\mathbf{q}} = \sigma_y S_{-,-\mathbf{q}}^*\sigma_y. \qquad (F19)$$

We will always make the assumption that C_{3z} and $\mathcal{T}$ symmetries are preserved. By Eq. (F19), $\mathcal{T}$ symmetry implies

$$S_-(\mathbf{r}) = \sigma_y S_+^*(\mathbf{r})\sigma_y \qquad (F20)$$

so it suffices to characterize $T(\mathbf{r})$ and $S_+(\mathbf{r})$. Keeping only the terms in Eq. (F16), we can use C_{3z}, $\mathcal{T}$, and Hermiticity to write

$$T_{\mathbf{q}_j} = u_{1,x}\boldsymbol{\sigma}\cdot\hat{\mathbf{n}}_{\zeta_j} + u_{1,y}\boldsymbol{\sigma}\cdot\hat{\mathbf{n}}_{\zeta_j+\pi/2} + u_{1,z}\sigma_z,$$
$$T_{-2\mathbf{q}_j} = u_{2,x}\boldsymbol{\sigma}\cdot\hat{\mathbf{n}}_{\zeta_j} + u_{2,y}\boldsymbol{\sigma}\cdot\hat{\mathbf{n}}_{\zeta_j+\pi/2} + u_{2,z}\sigma_z,$$
$$S_{+,\mathbf{0}} = u_{0,0}\sigma_0 + u_{0,z}\sigma_z,$$
$$S_{+,\mathbf{q}_{1+j}-\mathbf{q}_{2+j}} = u_{\sqrt{3},0}\sigma_0 + u_{\sqrt{3},x}\boldsymbol{\sigma}\cdot\hat{\mathbf{n}}_{\zeta_j}$$
$$+ u_{\sqrt{3},y}\boldsymbol{\sigma}\cdot\hat{\mathbf{n}}_{\zeta_j+\pi/2} + u_{\sqrt{3},z}\sigma_z,$$
$$S_{+,\mathbf{q}_{2+j}-\mathbf{q}_{1+j}} = S_{+,\mathbf{q}_{1+j}-\mathbf{q}_{2+j}}^\dagger, \qquad (F21)$$

where $u_{0,0}$ and $u_{0,z}$ are real parameters and all of the other u parameters are in general complex. We now consider the symmetry constraints in several cases.

(1) The symmetry group is generated by C_{3z} and $\mathcal{T}$. In this case,

$$u_{0,0}, u_{0,z} \in \mathbb{R}. \qquad (F22)$$

(2) The symmetry group is generated by C_{3z}, $\mathcal{T}$, and C_{2z}. In this case,

$$u_{0,0}, u_{1,x}, u_{1,y}, u_{2,x}, u_{2,y}, u_{\sqrt{3},0}, u_{\sqrt{3},x}, u_{\sqrt{3},y} \in \mathbb{R},$$
$$u_{1,z}, u_{2,z}, u_{\sqrt{3},z} \in i\mathbb{R},$$
$$u_{0,z} = 0. \qquad (F23)$$

(3) The symmetry group is generated by C_{3z}, $\mathcal{T}$, and M_x. In this case,

$$u_{0,0}, u_{0,z}, u_{1,y}, u_{2,y} \in \mathbb{R},$$
$$u_{1,x}, u_{1,z}, u_{2,x}, u_{2,z} \in i\mathbb{R},$$
$$u_{\sqrt{3},y} = 0. \qquad (F24)$$

(4) The symmetry group is generated by C_{3z}, $\mathcal{T}$, and M_y. In this case,

$$u_{0,0}, u_{\sqrt{3},0}, u_{\sqrt{3},x} \in \mathbb{R},$$
$$u_{\sqrt{3},y}, u_{\sqrt{3},z} \in i\mathbb{R},$$
$$u_{0,z} = u_{1,x} = u_{2,x} = 0. \qquad (F25)$$

(5) The symmetry group is generated by C_{3z}, $\mathcal{T}$, C_{2z}, M_x, and M_y. In this case,

$$u_{0,0}, u_{1,y}, u_{2,y}, u_{\sqrt{3},0}, u_{\sqrt{3},x} \in \mathbb{R},$$
$$u_{1,z}, u_{2,z}, u_{\sqrt{3},z} \in i\mathbb{R},$$
$$u_{0,z} = u_{1,x} = u_{2,x} = u_{\sqrt{3},y} = 0. \qquad (F26)$$

In this case, we summarize Eq. (F21) as

$$T_{m\mathbf{q}_j} = w_{|m|,y}\boldsymbol{\sigma}\cdot\hat{\mathbf{n}}_{\zeta_j+\pi/2} + w_{|m|,z}i\sigma_z,$$
$$S_{+,\mathbf{0}} = w_{0,0}\sigma_0,$$
$$S_{+,\gamma(\mathbf{q}_{1+j}-\mathbf{q}_{2+j})} = w_{\sqrt{3},0}\sigma_0 + w_{\sqrt{3},x}\boldsymbol{\sigma}\cdot\hat{\mathbf{n}}_{\zeta_j}$$
$$+ \gamma w_{\sqrt{3},z}i\sigma_z, \qquad (F27)$$

for $m \in \{1, -2\}$ and $\gamma \in \{+, -\}$, where the real w parameters are defined by

$$w_{1,y} = u_{1,y}, \quad w_{1,z} = -iu_{1,z}, \quad w_{2,y} = u_{2,y},$$
$$w_{2,z} = -iu_{2,z}, \quad w_{0,0} = u_{0,0},$$
$$w_{\sqrt{3},0} = u_{\sqrt{3},0}, \quad w_{\sqrt{3},x} = u_{\sqrt{3},x}, \quad w_{\sqrt{3},z} = -iu_{\sqrt{3},z}. \qquad (F28)$$

Note that $C_{2z} = M_x M_y$ so that this is a full enumeration of the cases with C_{3z} and $\mathcal{T}$ symmetries. See Appendix I for a discussion of these symmetry groups and Table III for their character tables.

3. Transformation to the moiré coordinate system

We now translate these results into the moiré coordinate system defined in Sec. E. Equations (F20) and (F21) become

$$S_{\xi,-}(\mathbf{r}) = \sigma_y S_{\xi,+}^*(\mathbf{r})\sigma_y \qquad (F29)$$

and

$$T_{\xi,\mathbf{q}_j} = u_{1,x}\boldsymbol{\sigma}\cdot\hat{\mathbf{n}}_{\zeta_j-\xi} + u_{1,y}\boldsymbol{\sigma}\cdot\hat{\mathbf{n}}_{\zeta_j+\pi/2-\xi} + u_{1,z}\sigma_z,$$
$$T_{\xi,-2\mathbf{q}_j} = u_{2,x}\boldsymbol{\sigma}\cdot\hat{\mathbf{n}}_{\zeta_j-\xi} + u_{2,y}\boldsymbol{\sigma}\cdot\hat{\mathbf{n}}_{\zeta_j+\pi/2-\xi} + u_{2,z}\sigma_z,$$
$$S_{\xi,+,\mathbf{0}} = u_{0,0}\sigma_0 + u_{0,z}\sigma_z,$$
$$S_{\xi,+,\mathbf{q}_{1+j}-\mathbf{q}_{2+j}} = u_{\sqrt{3},0}\sigma_0 + u_{\sqrt{3},x}\boldsymbol{\sigma}\cdot\hat{\mathbf{n}}_{\zeta_j-\xi} + u_{\sqrt{3},y}\boldsymbol{\sigma}\cdot\hat{\mathbf{n}}_{\zeta_j+\pi/2-\xi}$$
$$+ u_{\sqrt{3},z}\sigma_z,$$
$$S_{\xi,+,\mathbf{q}_{2+j}-\mathbf{q}_{1+j}} = S_{\xi,+,\mathbf{q}_{1+j}-\mathbf{q}_{2+j}}^\dagger. \qquad (F30)$$

TABLE III. Character tables enumerating the coirreps of the spinful magnetic point groups $31'$, $61'$, $mm21'$, $3m1'$, and $6mm1'$ described in Appendix I. Each column represents a corepresentation conjugacy class [31], and for brevity we do not include columns for conjugacy classes which are -1 times a shown conjugacy class, other than the class -1. As explained in Appendix I, the rows in each table for which the entry corresponding to -1 is positive (i.e., the spinless coirreps) also form the character tables for the spinless magnetic point groups $31'_0$, $61'_0$, $mm21'_0$, $3m1'_0$, and $6mm1'_0$. These tables can be found on the Bilbao Crystallographic Server [30,43,44,60,61].

$31'$	1	C_{3z}	C_{3z}^{-1}	-1			
A_1	1	1	1	1			
$^2E^1E$	2	-1	-1	2			
$\overline{E}\,\overline{E}$	2	-2	-2	-2			
$^1\overline{E}\,^2\overline{E}$	2	1	1	-2			

$61'$	1	C_{3z}	C_{3z}^{-1}	C_{2z}	C_{6z}^{-1}	C_{6z}	-1
A	1	1	1	1	1	1	1
B	1	1	1	-1	-1	-1	1
$^2E_1\,^1E_1$	2	-1	-1	2	-1	-1	2
$^2E_2\,^1E_2$	2	-1	-1	-2	1	1	2
$^2\overline{E}_1\,^1\overline{E}_1$	2	-2	-2	0	0	0	-2
$^1\overline{E}_3\,^2\overline{E}_3$	2	1	1	0	$\sqrt{3}$	$\sqrt{3}$	-2
$^1\overline{E}_2\,^2\overline{E}_2$	2	1	1	0	$-\sqrt{3}$	$-\sqrt{3}$	-2

$mm21'$	1	C_{2z}	M_x	M_y	-1		
A_1	1	1	1	1	1		
A_2	1	1	-1	-1	1		
B_1	1	-1	-1	1	1		
B_2	1	-1	1	-1	1		
$\overline{E}$	2	0	0	0	-2		

$3m1'$	1	C_{3z}	M	-1			
A_1	1	1	1	1			
A_2	1	1	-1	1			
E	2	-1	0	2			
$^2\overline{E}\,^1E$	2	-2	0	-2			
$\overline{E}_1$	2	1	0	-2			

$6mm1'$	1	C_{3z}	C_{2z}	C_{6z}	M_x	M_y	-1
A_1	1	1	1	1	1	1	1
A_2	1	1	1	1	-1	-1	1
B_2	1	1	-1	-1	-1	1	1
B_1	1	1	-1	-1	1	-1	1
E_2	2	-1	2	-1	0	0	2
E_1	2	-1	-2	1	0	0	2
$\overline{E}_3$	2	-2	0	0	0	0	-2
$\overline{E}_2$	2	1	0	$-\sqrt{3}$	0	0	-2
$\overline{E}_1$	2	1	0	$\sqrt{3}$	0	0	-2

Additionally, Eq. (F27) becomes

$$T_{\xi,m\mathbf{q}_j} = w_{|m|,y}\boldsymbol{\sigma}\cdot\hat{\mathbf{n}}_{\zeta_j+\phi_1} + w_{|m|,z}i\sigma_z,$$

$$S_{\xi,+,\mathbf{0}} = w_{0,0}\sigma_0,$$

$$S_{\xi,+,\gamma(\mathbf{q}_{1+j}-\mathbf{q}_{2+j})} = w_{\sqrt{3},0}\sigma_0 + w_{\sqrt{3},x}\boldsymbol{\sigma}\cdot\hat{\mathbf{n}}_{\zeta_j+\phi_1-\pi/2}$$
$$+ i\gamma\, w_{\sqrt{3},z}\sigma_z, \tag{F31}$$

for $m \in \{1, -2\}$ and $\gamma \in \{+, -\}$, where

$$\phi_1 = \pi/2 - \xi = \arg(e^{-\delta\epsilon-i\delta\theta} - 1) \tag{F32}$$

since $\xi_0 = \pi$.

4. Coirrep decomposition for the bottom layer

In this section, we show that the $T(\mathbf{r})$ and $S_+(\mathbf{r})$ potentials can be written as a sum over the irreducible corepresentations (coirreps) of the symmetry group at the $\boldsymbol{\Gamma}_-$ point in the bottom layer. To do so, we analyze the nontranslational symmetries of the bilayer continuum Hamiltonian in Eq. (F11). Generalizing Eq. (F17), the relevant symmetry generators take the form

$$C_{3z}|\mathbf{r}\rangle_g = |R_{2\pi/3}\mathbf{r}\rangle_g e^{i(2\pi/3)\sigma_z\otimes\sigma_z} \oplus C_{3z,-},$$

$$C_{2z}|\mathbf{r}\rangle_g = |-\mathbf{r}\rangle_g(\sigma_x\otimes\sigma_x) \oplus C_{2z,-},$$

$$M_x|\mathbf{r}\rangle_g = |\mathcal{R}_{\hat{\mathbf{x}}}\mathbf{r}\rangle_g(\sigma_x\otimes\sigma_0) \oplus M_{x,-},$$

$$M_y|\mathbf{r}\rangle_g = |\mathcal{R}_{\hat{\mathbf{y}}}\mathbf{r}\rangle_g(\sigma_0\otimes\sigma_x) \oplus M_{y,-},$$

$$\mathcal{T}|\mathbf{r}\rangle_g = |\mathbf{r}\rangle_g(\sigma_x\otimes\sigma_0) \oplus \mathcal{T}_-, \tag{F33}$$

for some unitary matrices $C_{3z,-}$, $C_{2z,-}$, $M_{x,-}$, $M_{y,-}$, and $\mathcal{T}_-$, which act on the bottom layer. In a manner similar to that in Appendix F 2, one can derive the following constraints on the $T_{\eta,\mathbf{q}_j}$ matrices arising from the commutation of each symmetry with H_c;

$$[C_{3z}, H_c] = 0 \iff T_{\eta,\mathbf{q}_{j+1}} = e^{i\eta(2\pi/3)\sigma_z}T_{\eta,\mathbf{q}_j}C_{3z,-}^\dagger,$$

$$[C_{2z}, H_c] = 0 \iff T_{\eta,\mathbf{q}_j} = \sigma_x T_{-\eta,\mathbf{q}_j}C_{2z,-}^\dagger,$$

$$[M_x, H_c] = 0 \iff T_{\eta,\mathbf{q}_1} = T_{-\eta,\mathbf{q}_1}M_{x,-}^\dagger$$

$$T_{\eta,\mathbf{q}_2} = T_{-\eta,\mathbf{q}_3}M_{x,-}^\dagger\,T_{\eta,\mathbf{q}_3} = T_{-\eta,\mathbf{q}_2}M_{x,-}^\dagger,$$

$$[M_y, H_c] = 0 \iff T_{\eta,\mathbf{q}_1} = \sigma_x T_{\eta,\mathbf{q}_1}M_{y,-}^\dagger$$

$$T_{\eta,\mathbf{q}_2} = \sigma_x T_{\eta,\mathbf{q}_3}M_{y,-}^\dagger\,T_{\eta,\mathbf{q}_3} = \sigma_x T_{\eta,\mathbf{q}_2}M_{y,-}^\dagger,$$

$$[\mathcal{T}, H_c] = 0 \iff T_{\eta,\mathbf{q}_j} = T_{-\eta,\mathbf{q}_j}^*\mathcal{T}_-^\dagger. \tag{F34}$$

In the presence of C_{3z} and $\mathcal{T}$ symmetries, all of the $T_{\eta,\mathbf{q}_j}$ matrices are determined by $T_{+,\mathbf{q}_1}$. Specifically, we have

$$T_{\eta,\mathbf{q}_j} = e^{i\eta\zeta_j\sigma_z}T_{\eta,\mathbf{q}_1}C_{3z,-}^{1-j},$$

$$T_{-,\mathbf{q}_1} = T_{+,\mathbf{q}_1}^*\mathcal{T}_-^\dagger. \tag{F35}$$

Any additional symmetries then imply constraints on $T_{+,\mathbf{q}_1}$. Specifically,

$$[C_{2z}, H_c] = 0 \Rightarrow T_{+,\mathbf{q}_1} = \sigma_x T_{+,\mathbf{q}_1}^*(C_{2z,-}\mathcal{T}_-)^\dagger, \tag{F36}$$

$$[M_x, H_c] = 0 \Rightarrow T_{+,\mathbf{q}_1} = T_{+,\mathbf{q}_1}^*(M_{x,-}\mathcal{T}_-)^\dagger, \tag{F37}$$

$$[M_y, H_c] = 0 \Rightarrow T_{+,\mathbf{q}_1} = \sigma_x T_{+,\mathbf{q}_1}M_{y,-}^\dagger. \tag{F38}$$

By Eqs. (F11) and (F15), we have

$$T(\mathbf{r}) = -\sum_{j,k=1}^3 T_{+,\mathbf{q}_j}\mathcal{H}_-^{-1}T_{-,\mathbf{q}_k}^\dagger\sigma_y e^{-i\mathbf{r}\cdot(\mathbf{q}_k+\mathbf{q}_j)} \tag{F39}$$

$$= -\sum_{j,k=1}^3 e^{i\zeta_j\sigma_z}T_{+,\mathbf{q}_1}C_{3z,-}^{1-j}\mathcal{H}_-^{-1}C_{3z,-}^{k-1}\mathcal{T}_-T_{+,\mathbf{q}_1}^T$$

$$\times \sigma_y e^{-i\zeta_k\sigma_z}e^{-i\mathbf{r}\cdot(\mathbf{q}_k+\mathbf{q}_j)}, \tag{F40}$$

$$S_+(\mathbf{r}) = -\sum_{j,k=1}^{3} T_{+,\mathbf{q}_j} \mathcal{H}_-^{-1} T_{+,\mathbf{q}_k}^{\dagger} e^{i\mathbf{r}\cdot(\mathbf{q}_k - \mathbf{q}_j)} \tag{F41}$$

$$= -\sum_{j,k=1}^{3} e^{i\zeta_j\sigma_z} T_{+,\mathbf{q}_1} C_{3z,-}^{1-j} \mathcal{H}_-^{-1} C_{3z,-}^{k-1} T_{+,\mathbf{q}_1}^{\dagger} e^{-i\zeta_k\sigma_z} e^{i\mathbf{r}\cdot(\mathbf{q}_k - \mathbf{q}_j)}. \tag{F42}$$

It follows that we can compute the $T(\mathbf{r})$ and $S_+(\mathbf{r})$ potentials from $T_{+,\mathbf{q}_1}$ along with $\mathcal{H}_-$ and the symmetry corepresentation on the bottom layer.

By Schur's lemma for corepresentation theory, there is a unitary change of basis for the bottom layer subspace that diagonalizes $\mathcal{H}_-$ while also block diagonalizing the symmetry corepresentation on the bottom layer into coirreps [31]. The contributions to $T(\mathbf{r})$ and $S_+(\mathbf{r})$ in Eqs. (F40) and (F42) from each coirrep simply add. We can therefore consider the form for $T(\mathbf{r})$ and $S_+(\mathbf{r})$ independently for each coirrep. In the following sections, we explicitly find the form for the u parameters in Eq. (F21) for each coirrep of each possible symmetry group that contains C_{3z} and $\mathcal{T}$.

a. The symmetry group is generated by C_{3z} and $\mathcal{T}$

In this case, the symmetry group is isomorphic to the spinless magnetic point group $31'_0$ defined in Appendix I. We see from Table III that there are two coirreps, namely A_1 and $^2E^1E$.

(1) For A_1, we take $C_{3z,-} = 1$, $\mathcal{T}_- = 1$, and

$$T_{+,\mathbf{q}_1} = \begin{pmatrix} v_1 \\ v_2 \end{pmatrix} \tag{F43}$$

for complex parameters v_1 and v_2. Taking $\mathcal{H}_- = E_0$, Eqs. (F40) and (F42) imply that $T(\mathbf{r})$ and $S_\eta(\mathbf{r})$ take the form of Eq. (F21) with

$$u_{1,x} = \frac{i}{E_0}(v_1^2 - v_2^2), \quad u_{1,y} = -\frac{1}{E_0}(v_1^2 + v_2^2),$$

$$u_{1,z} = \frac{i}{E_0}v_1 v_2,$$

$$u_{2,x} = \frac{i}{2E_0}(v_1^2 - v_2^2), \quad u_{2,y} = -\frac{1}{2E_0}(v_1^2 + v_2^2),$$

$$u_{2,z} = -\frac{i}{E_0}v_1 v_2,$$

$$u_{0,0} = -\frac{3}{2E_0}(|v_1|^2 + |v_2|^2), \quad u_{0,z} = -\frac{3}{2E_0}(|v_1|^2 - |v_2|^2),$$

$$u_{\sqrt{3},0} = \frac{1 - i\sqrt{3}}{4E_0}|v_1|^2 + \frac{1 + i\sqrt{3}}{4E_0}|v_2|^2,$$

$$u_{\sqrt{3},x} = -\frac{1}{2E_0}(v_1 v_2^* + v_1^* v_2),$$

$$u_{\sqrt{3},y} = -\frac{i}{2E_0}(v_1 v_2^* - v_1^* v_2),$$

$$u_{\sqrt{3},z} = \frac{1 - i\sqrt{3}}{4E_0}|v_1|^2 - \frac{1 + i\sqrt{3}}{4E_0}|v_2|^2. \tag{F44}$$

(2) For $^2E^1E$, we take $C_{3z,-} = e^{-i(2\pi/3)\sigma_z}$, $\mathcal{T}_- = \sigma_x$, and

$$T_{+,\mathbf{q}_1} = v_0\sigma_0 + v_x\sigma_x + v_y\sigma_y + v_z\sigma_z \tag{F45}$$

for complex parameters v_0, v_x, v_y, and v_z. Taking $\mathcal{H}_- = E_0\sigma_0$, Eqs. (F40) and (F42) imply that $T(\mathbf{r})$ and $S_\eta(\mathbf{r})$ take the form of Eq. (F21) with

$$u_{1,x} = -\frac{2}{E_0}(v_0 v_y + i v_x v_z), \quad u_{1,y} = \frac{2}{E_0}(v_0 v_x - i v_y v_z), \quad u_{1,z} = \frac{i}{E_0}(v_0^2 - 2v_x^2 - 2v_y^2 - v_z^2),$$

$$u_{2,x} = \frac{2}{E_0}(v_0 v_y + i v_x v_z), \quad u_{2,y} = -\frac{2}{E_0}(v_0 v_x - i v_y v_z), \quad u_{2,z} = -\frac{i}{E_0}(v_0^2 + v_x^2 + v_y^2 - v_z^2),$$

$$u_{0,0} = -\frac{3}{E_0}(|v_0|^2 + |v_x|^2 + |v_y|^2 + |v_z|^2), \quad u_{0,z} = -\frac{3}{E_0}(v_0 v_z^* + v_0^* v_z + i(v_x v_y^* - v_x^* v_y)),$$

$$u_{\sqrt{3},0} = \frac{1}{2E_0}(|v_0|^2 - 2|v_x|^2 - 2|v_y|^2 + |v_z|^2 + i\sqrt{3}(v_0 v_z^* + v_0^* v_z)),$$

$$u_{\sqrt{3},x} = \frac{1}{2E_0}(v_0 v_x^* + v_0^* v_x + i(v_y v_z^* - v_y^* v_z) - \sqrt{3}(v_0 v_y^* - v_0^* v_y) - i\sqrt{3}(v_x v_z^* + v_x^* v_z)),$$

$$u_{\sqrt{3},y} = \frac{1}{2E_0}(v_0 v_y^* + v_0^* v_y - i(v_x v_z^* - v_x^* v_z) + \sqrt{3}(v_0 v_x^* - v_0^* v_x) - i\sqrt{3}(v_y v_z^* + v_y^* v_z)),$$

$$u_{\sqrt{3},z} = \frac{1}{2E_0}(v_0 v_z^* + v_0^* v_z - 2i(v_x v_y^* - v_x^* v_y) + i\sqrt{3}(|v_0|^2 + |v_z|^2)). \tag{F46}$$

b. The symmetry group is generated by C_{3z}, $\mathcal{T}$, and C_{2z}

In this case, the symmetry group is isomorphic to the spinless magnetic point group $61'_0$ defined in Appendix I. We see from Table III that there are four coirreps, namely A, B, $^2E_1{}^1E_1$, and $^2E_2{}^1E_2$.

(1) For A, we take $C_{3z,-} = 1$, $\mathcal{T}_- = 1$, and $C_{2z,-} = 1$. Equations (F43) and (F44) apply, and additionally Eq. (F36) implies

$$v_2 = v_1^*. \tag{F47}$$

(2) For B, we take $C_{3z,-} = 1$, $\mathcal{T}_- = 1$, and $C_{2z,-} = -1$. Equations (F43) and (F44) apply, and additionally Eq. (F36) implies

$$v_2 = -v_1^*. \tag{F48}$$

(3) For ${}^2E_1{}^1E_1$, we take $C_{3z,-} = e^{-i(2\pi/3)\sigma_z}$, $\mathcal{T}_- = \sigma_x$, and $C_{2z,-} = \sigma_0$. Equations (F45) and (F46) apply, and additionally Eq. (F36) implies

$$v_0, v_x, v_y \in \mathbb{R}, \quad v_z \in i\mathbb{R}. \tag{F49}$$

(4) For ${}^2E_2{}^1E_2$, we take $C_{3z,-} = e^{-i(2\pi/3)\sigma_z}$, $\mathcal{T}_- = \sigma_x$, and $C_{2z,-} = -\sigma_0$. Equations (F45) and (F46) apply, and additionally Eq. (F36) implies

$$v_z \in \mathbb{R}, \quad v_0, v_x, v_y \in i\mathbb{R}. \tag{F50}$$

c. The symmetry group is generated by C_{3z}, $\mathcal{T}$, and M_x

In this case, the symmetry group is isomorphic to the spinless magnetic point group $3m1_0'$ defined in Appendix I. We see from Table III that there are three coirreps, namely A_1, A_2, and E.

(1) For A_1, we take $C_{3z,-} = 1$, $\mathcal{T}_- = 1$, and $M_{x,-} = 1$. Equations (F43) and (F44) apply, and additionally Eq. (F37) implies

$$v_1, v_2 \in \mathbb{R}. \tag{F51}$$

(2) For A_2, we take $C_{3z,-} = 1$, $\mathcal{T}_- = 1$, and $M_{x,-} = -1$. Equations (F43) and (F44) apply, and additionally Eq. (F37) implies

$$v_1, v_2 \in i\mathbb{R}. \tag{F52}$$

(3) For E, we take $C_{3z,-} = e^{-i(2\pi/3)\sigma_z}$, $\mathcal{T}_- = \sigma_x$, and $M_{x,-} = -\sigma_x$. Equations (F45) and (F46) apply, and additionally Eq. (F37) implies

$$v_y \in \mathbb{R}, \quad v_0, v_x, v_z \in i\mathbb{R}. \tag{F53}$$

d. The symmetry group is generated by C_{3z}, $\mathcal{T}$, and M_y

In this case, the symmetry group is isomorphic to the spinless magnetic point group $3m1_0'$ defined in Appendix I. We see from Table III that there are three coirreps, namely A_1, A_2, and E.

(1) For A_1, we take $C_{3z,-} = 1$, $\mathcal{T}_- = 1$, and $M_{y,-} = 1$. Equations (F43) and (F44) apply, and additionally Eq. (F38) implies

$$v_2 = v_1. \tag{F54}$$

(2) For A_2, we take $C_{3z,-} = 1$, $\mathcal{T}_- = 1$, and $M_{y,-} = -1$. Equations (F43) and (F44) apply, and additionally Eq. (F38) implies

$$v_2 = -v_1. \tag{F55}$$

(3) For E, we take $C_{3z,-} = e^{-i(2\pi/3)\sigma_z}$, $\mathcal{T}_- = \sigma_x$, and $M_{y,-} = \sigma_x$. Equations (F45) and (F46) apply, and additionally Eq. (F38) implies

$$v_y = v_z = 0. \tag{F56}$$

e. The symmetry group is generated by C_{3z}, $\mathcal{T}$, C_{2z}, M_x, and M_y

In this case, the symmetry group is isomorphic to the spinless magnetic point group $6mm1_0'$ defined in Appendix I. We see from Table III that there are six coirreps, namely A_1, A_2, B_2, B_1, E_2, and E_1.

(1) For A_1, we take $C_{3z,-} = 1$, $\mathcal{T}_- = 1$, $C_{2z,-} = 1$, $M_{x,-} = 1$, and $M_{y,-} = 1$. Equations (F43) and (F44) apply, and additionally Eqs. (F36)–(F38) imply Eqs. (F47), (F51), and (F54).

(2) For A_2, we take $C_{3z,-} = 1$, $\mathcal{T}_- = 1$, $C_{2z,-} = 1$, $M_{x,-} = -1$, and $M_{y,-} = -1$. Equations (F43) and (F44) apply, and additionally Eqs. (F36)–(F38) imply Eqs. (F47), (F52), and (F55).

(3) For B_2, we take $C_{3z,-} = 1$, $\mathcal{T}_- = 1$, $C_{2z,-} = -1$, $M_{x,-} = -1$, and $M_{y,-} = 1$. Equations (F43) and (F44) apply, and additionally Eqs. (F36)–(F38) imply Eqs. (F48), (F52), and (F54).

(4) For B_1, we take $C_{3z,-} = 1$, $\mathcal{T}_- = 1$, $C_{2z,-} = -1$, $M_{x,-} = 1$, and $M_{y,-} = -1$. Equations (F43) and (F44) apply, and additionally Eqs. (F36)–(F38) imply Eqs. (F48), (F51), and (F55).

(5) For E_2, we take $C_{3z,-} = e^{-i(2\pi/3)\sigma_z}$, $\mathcal{T}_- = \sigma_x$, $C_{2z,-} = \sigma_0$, $M_{x,-} = \sigma_x$, and $M_{y,-} = \sigma_x$. Equations (F45) and (F46) apply, and additionally (F36) and (F38) imply (F49) and (F56) while Eq. (F37) implies

$$v_0, v_x, v_z \in \mathbb{R}, \quad v_y \in i\mathbb{R}. \tag{F57}$$

(6) For E_1, we take $C_{3z,-} = e^{-i(2\pi/3)\sigma_z}$, $\mathcal{T}_- = \sigma_x$, $C_{2z,-} = -\sigma_0$, $M_{x,-} = -\sigma_x$, and $M_{y,-} = \sigma_x$. Equations (F45) and (F46) apply, and additionally Eqs. (F36)–(F38) imply Eqs. (F50), (F53), and (F56).

We can summarize the results for this case more succinctly using the w parameters in Eq. (F27). For coirreps A_1, A_2, B_2, and B_1, we have

$$w_{1,y} = -\frac{2v_1^2}{E_0}, \quad w_{1,z} = \frac{M_{y,-}v_1^2}{E_0},$$

$$w_{2,y} = -\frac{v_1^2}{E_0}, \quad w_{2,z} = -\frac{M_{y,-}v_1^2}{E_0},$$

$$w_{0,0} = -\frac{3|v_1|^2}{E_0}, \quad w_{\sqrt{3},0} = \frac{|v_1|^2}{2E_0},$$

$$w_{\sqrt{3},x} = -\frac{M_{y,-}|v_1|^2}{E_0}, \quad w_{\sqrt{3},z} = -\frac{|v_1|^2\sqrt{3}}{2E_0}, \tag{F58}$$

where $v_1 \in \mathbb{R}$ for A_1 and B_1, $v_1 \in i\mathbb{R}$ for A_2 and B_2, $M_{y,-} = 1$ for A_1 and B_2, and $M_{y,-} = -1$ for A_2 and B_1. Likewise, for coirreps E_2 and E_1, we have

$$w_{1,y} = \frac{2v_0 v_x}{E_0}, \quad w_{1,z} = \frac{v_0^2 - 2v_x^2}{E_0}, \quad w_{2,y} = -\frac{2v_0 v_x}{E_0},$$

$$w_{2,z} = -\frac{v_0^2 + v_x^2}{E_0}, \quad w_{0,0} = -\frac{3(|v_0|^2 + |v_x|^2)}{E_0},$$

$$w_{\sqrt{3},0} = \frac{|v_0|^2 - 2|v_x|^2}{2E_0}, \quad w_{\sqrt{3},x} = \frac{v_0 v_x^* + v_0^* v_x}{2E_0},$$

$$w_{\sqrt{3},z} = \frac{|v_0|^2\sqrt{3}}{2E_0}, \tag{F59}$$

where $v_0, v_x \in \mathbb{R}$ for E_2 and $v_0, v_x \in i\mathbb{R}$ for E_1.

APPENDIX G: COUPLED-VALLEY GRAPHENE MODEL WITH SPIN

In Appendix F we ignored the spin degrees of freedom in order to simplify the discussion. In this Appendix, we present the changes necessary to the derivation in Appendix F to include spin and spin-orbit coupling.

1. Continuum model

We use $|\uparrow\rangle$ and $|\downarrow\rangle$ to denote orthonormal spin states in the z direction and define the row vector of states

$$|s_z\rangle = (|\uparrow\rangle \quad |\downarrow\rangle). \tag{G1}$$

Generalizing Eq. (F11), the spinful continuum Hamiltonian is

$$\tilde{H}_c = \int d^2\mathbf{r}(|\mathbf{r}\rangle_c \otimes |s_z\rangle)\tilde{\mathcal{H}}_c(\mathbf{r})((\langle\mathbf{r}|_c \otimes \langle s_z|)$$

$$\tilde{\mathcal{H}}_c(\mathbf{r}) = \begin{pmatrix} -i\hbar v_F \boldsymbol{\sigma} \cdot \nabla \otimes \sigma_0 & 0 & \tilde{T}_+(\mathbf{r}) \\ 0 & i\hbar v_F \boldsymbol{\sigma}^* \cdot \nabla \otimes \sigma_0 & \tilde{T}_-(\mathbf{r}) \\ \tilde{T}_+^\dagger(\mathbf{r}) & \tilde{T}_-^\dagger(\mathbf{r}) & \tilde{\mathcal{H}}_- \end{pmatrix}$$

$$\tilde{T}_\eta(\mathbf{r}) = \sum_{j=1}^{3} \tilde{T}_{\eta,\mathbf{q}_j} e^{-i\eta\mathbf{r}\cdot\mathbf{q}_j}. \tag{G2}$$

Here, the $\tilde{T}_{\eta,\mathbf{q}_j}$ are $4 \times (2n)$ complex matrices and $\tilde{\mathcal{H}}_-$ is the spinful Hamiltonian for the bottom layer at $\boldsymbol{\Gamma}_-$. After applying perturbation theory and a change of basis, we find a spinful continuum Hamiltonian for the graphene degrees of freedom of the form

$$\tilde{H}_g = \int d^2\mathbf{r}(|\mathbf{r}\rangle \otimes |s_z\rangle)\tilde{\mathcal{H}}(\mathbf{r})((\langle\mathbf{r}| \otimes \langle s_z|)$$

$$\tilde{\mathcal{H}}(\mathbf{r}) = \begin{pmatrix} \tilde{S}_+(\mathbf{r}) - i\hbar v_F \boldsymbol{\sigma} \cdot \nabla \otimes \sigma_0 & \tilde{T}(\mathbf{r}) \\ \tilde{T}^\dagger(\mathbf{r}) & \tilde{S}_-(\mathbf{r}) - i\hbar v_F \boldsymbol{\sigma} \cdot \nabla \otimes \sigma_0 \end{pmatrix} \tag{G3}$$

where the $\tilde{T}$ and $\tilde{S}_\eta$ potentials are given by

$$\tilde{T}(\mathbf{r}) = -\tilde{T}_+(\mathbf{r})\tilde{\mathcal{H}}_-^{-1}\tilde{T}_-^\dagger(\mathbf{r})(\sigma_y \otimes \sigma_0), \quad \tilde{S}_+(\mathbf{r}) = -\tilde{T}_+(\mathbf{r})\tilde{\mathcal{H}}_-^{-1}\tilde{T}_+^\dagger(\mathbf{r}),$$

$$\tilde{S}_-(\mathbf{r}) = -(\sigma_y \otimes \sigma_0)\tilde{T}_-(\mathbf{r})\tilde{\mathcal{H}}_-^{-1}\tilde{T}_-^\dagger(\mathbf{r})(\sigma_y \otimes \sigma_0). \tag{G4}$$

We expand the potentials as

$$\tilde{T}(\mathbf{r}) = \sum_{\mathbf{q}\in P_M^+} \tilde{T}_\mathbf{q} e^{i\mathbf{r}\cdot\mathbf{q}}, \quad \tilde{S}_\eta(\mathbf{r}) = \sum_{\mathbf{q}\in P_M} \tilde{S}_{\eta,\mathbf{q}} e^{i\mathbf{r}\cdot\mathbf{q}} \tag{G5}$$

for 4×4 complex matrices $\tilde{T}_\mathbf{q}$ and $\tilde{S}_{\eta,\mathbf{q}}$ with $\tilde{S}_{\eta,\mathbf{q}}^\dagger = \tilde{S}_{\eta,-\mathbf{q}}$.

2. Symmetry constraints

In the presence of spin, we supplement Eqs. (F17) and (F18) with

$$C_{3z}|s_z\rangle = |s_z\rangle e^{-i(\pi/3)\sigma_z}, \quad C_{2z}|s_z\rangle = |s_z\rangle e^{-i(\pi/2)\sigma_z},$$

$$M_x|s_z\rangle = |s_z\rangle e^{-i(\pi/2)\sigma_x}, \quad M_y|s_z\rangle = |s_z\rangle e^{-i(\pi/2)\sigma_y},$$

$$\mathcal{T}|s_z\rangle = |s_z\rangle\sigma_y. \tag{G6}$$

Equation (F19) then generalizes to

$$[C_{3z}, \tilde{H}_g] = 0 \iff \tilde{T}_{R_{2\pi/3}\mathbf{q}} = (e^{i(2\pi/3)\sigma_z} \otimes e^{i(2\pi/3)\sigma_z})\tilde{T}_\mathbf{q}(e^{-i(2\pi/3)\sigma_z} \otimes e^{-i(2\pi/3)\sigma_z}) \quad \text{and}$$

$$\tilde{S}_{\eta,R_{2\pi/3}\mathbf{q}} = (e^{i(2\pi/3)\sigma_z} \otimes e^{i(2\pi/3)\sigma_z})\tilde{S}_{\eta,\mathbf{q}}(e^{-i(2\pi/3)\sigma_z} \otimes e^{-i(2\pi/3)\sigma_z}),$$

$$[C_{2z}, \tilde{H}_g] = 0 \iff \tilde{T}_\mathbf{q} = -(\sigma_z \otimes \sigma_z)\tilde{T}_\mathbf{q}^\dagger(\sigma_z \otimes \sigma_z) \quad \text{and} \quad \tilde{S}_{+,-\mathbf{q}} = (\sigma_z \otimes \sigma_z)\tilde{S}_{-,\mathbf{q}}(\sigma_z \otimes \sigma_z),$$

$$[M_x, \tilde{H}_g] = 0 \iff \tilde{T}_{\mathcal{R}_{\hat{y}}\mathbf{q}} = (\sigma_y \otimes \sigma_x)\tilde{T}_\mathbf{q}^\dagger(\sigma_y \otimes \sigma_x) \quad \text{and} \quad \tilde{S}_{+,\mathcal{R}_{\hat{y}}\mathbf{q}} = (\sigma_y \otimes \sigma_x)\tilde{S}_{-,-\mathbf{q}}(\sigma_y \otimes \sigma_x),$$

$$[M_y, \tilde{H}_g] = 0 \iff \tilde{T}_{\mathcal{R}_{\hat{y}}\mathbf{q}} = -(\sigma_x \otimes \sigma_y)\tilde{T}_\mathbf{q}(\sigma_x \otimes \sigma_y) \quad \text{and} \quad \tilde{S}_{\eta,\mathcal{R}_{\hat{y}}\mathbf{q}} = (\sigma_x \otimes \sigma_y)\tilde{S}_{\eta,\mathbf{q}}(\sigma_x \otimes \sigma_y),$$

$$[\mathcal{T}, \tilde{H}_g] = 0 \iff \tilde{T}_\mathbf{q} = -(\sigma_y \otimes \sigma_y)\tilde{T}_\mathbf{q}^T(\sigma_y \otimes \sigma_y) \quad \text{and} \quad \tilde{S}_{+,\mathbf{q}} = (\sigma_y \otimes \sigma_y)\tilde{S}_{-,-\mathbf{q}}^*(\sigma_y \otimes \sigma_y), \tag{G7}$$

where the newly added second Pauli matrix in each tensor product acts on spin.

As in Appendix F 2, we will always make the assumption that C_{3z} and $\mathcal{T}$ symmetries are preserved. By Eq. (G7), $\mathcal{T}$ symmetry implies

$$\tilde{S}_-(\mathbf{r}) = (\sigma_y \otimes \sigma_y)\tilde{S}_+^*(\mathbf{r})(\sigma_y \otimes \sigma_y) \tag{G8}$$

so it suffices to characterize $\tilde{T}(\mathbf{r})$ and $\tilde{S}_+(\mathbf{r})$. If we expand these potentials to second order as in Eqs. (G4) and (G5), we can use C_{3z}, $\mathcal{T}$, and Hermiticity to write

$$\tilde{T}_{\mathbf{q}_j} = T_{\mathbf{q}_j} \otimes \sigma_0 + \sigma_0 \otimes (\tilde{u}_{1,0x}\boldsymbol{\sigma} \cdot \hat{\mathbf{n}}_{\zeta_j} + \tilde{u}_{1,0y}\boldsymbol{\sigma} \cdot \hat{\mathbf{n}}_{\zeta_j+\pi/2} + \tilde{u}_{1,0z}\sigma_z),$$

$$\tilde{T}_{-2\mathbf{q}_j} = T_{-2\mathbf{q}_j} \otimes \sigma_0 + \sigma_0 \otimes (\tilde{u}_{2,0x}\boldsymbol{\sigma} \cdot \hat{\mathbf{n}}_{\zeta_j} + \tilde{u}_{2,0y}\boldsymbol{\sigma} \cdot \hat{\mathbf{n}}_{\zeta_j+\pi/2} + \tilde{u}_{2,0z}\sigma_z),$$

$$\tilde{S}_{+,\mathbf{0}} = S_{+,\mathbf{0}} \otimes \sigma_0 + \tilde{u}_{0,0z}\sigma_0 \otimes \sigma_z + \tilde{u}_{0,zz}\sigma_z \otimes \sigma_z + \tilde{u}_{0,xx}(\sigma_x \otimes \sigma_x + \sigma_y \otimes \sigma_y) + \tilde{u}_{0,xy}(\sigma_x \otimes \sigma_y - \sigma_y \otimes \sigma_x),$$

$$\tilde{S}_{+,\mathbf{q}_{1+j}-\mathbf{q}_{2+j}} = S_{+,\mathbf{q}_{1+j}-\mathbf{q}_{2+j}} \otimes \sigma_0 + \sigma_0 \otimes (\tilde{u}_{\sqrt{3},0x}\boldsymbol{\sigma} \cdot \hat{\mathbf{n}}_{\zeta_j} + \tilde{u}_{\sqrt{3},0y}\boldsymbol{\sigma} \cdot \hat{\mathbf{n}}_{\zeta_j+\pi/2} + \tilde{u}_{\sqrt{3},0z}\sigma_z)$$

$$+ \boldsymbol{\sigma} \cdot \hat{\mathbf{n}}_{\zeta_j} \otimes (\tilde{u}_{\sqrt{3},xx}\boldsymbol{\sigma} \cdot \hat{\mathbf{n}}_{\zeta_j} + \tilde{u}_{\sqrt{3},xy}\boldsymbol{\sigma} \cdot \hat{\mathbf{n}}_{\zeta_j+\pi/2} + \tilde{u}_{\sqrt{3},xz}\sigma_z)$$

$$+ \boldsymbol{\sigma} \cdot \hat{\mathbf{n}}_{\zeta_j+\pi/2} \otimes (\tilde{u}_{\sqrt{3},yx}\boldsymbol{\sigma} \cdot \hat{\mathbf{n}}_{\zeta_j} + \tilde{u}_{\sqrt{3},yy}\boldsymbol{\sigma} \cdot \hat{\mathbf{n}}_{\zeta_j+\pi/2} + \tilde{u}_{\sqrt{3},yz}\sigma_z)$$

$$+ \sigma_z \otimes (\tilde{u}_{\sqrt{3},zx}\boldsymbol{\sigma} \cdot \hat{\mathbf{n}}_{\zeta_j} + \tilde{u}_{\sqrt{3},zy}\boldsymbol{\sigma} \cdot \hat{\mathbf{n}}_{\zeta_j+\pi/2} + \tilde{u}_{\sqrt{3},zz}\sigma_z),$$

$$\tilde{S}_{+,\mathbf{q}_{2+j}-\mathbf{q}_{1+j}} = \tilde{S}_{+,\mathbf{q}_{1+j}-\mathbf{q}_{2+j}}^\dagger, \tag{G9}$$

where $\tilde{u}_{0,0z}$, $\tilde{u}_{0,zz}$, $\tilde{u}_{0,xx}$, and $\tilde{u}_{0,xy}$ are real parameters, all of the other $\tilde{u}$ parameters are in general complex, and where the forms for the $T_\mathbf{q}$ and $S_{+,\mathbf{q}}$ matrices are given in Eq. (F21). We now consider the symmetry constraints in the same five cases as in Appendix F 2.

(1) The symmetry group is generated by C_{3z} and $\mathcal{T}$. In this case, we have Eq. (F22) and

$$\tilde{u}_{0,0z}, \tilde{u}_{0,zz}, \tilde{u}_{0,xx}, \tilde{u}_{0,xy} \in \mathbb{R}. \tag{G10}$$

(2) The symmetry group is generated by C_{3z}, $\mathcal{T}$, and C_{2z}. In this case, we have Eq. (F23) and

$$\tilde{u}_{0,zz}, \tilde{u}_{0,xx}, \tilde{u}_{0,xy}, \tilde{u}_{1,0x}, \tilde{u}_{1,0y}, \tilde{u}_{2,0x}, \tilde{u}_{2,0y}, \tilde{u}_{\sqrt{3},0x}, \tilde{u}_{\sqrt{3},0y}, \tilde{u}_{\sqrt{3},xx}, \tilde{u}_{\sqrt{3},xy}, \tilde{u}_{\sqrt{3},yx}, \tilde{u}_{\sqrt{3},yy}, \tilde{u}_{\sqrt{3},zz} \in \mathbb{R},$$

$$\tilde{u}_{1,0z}, \tilde{u}_{2,0z}, \tilde{u}_{\sqrt{3},0z}, \tilde{u}_{\sqrt{3},xz}, \tilde{u}_{\sqrt{3},yz}, \tilde{u}_{\sqrt{3},zx}, \tilde{u}_{\sqrt{3},zy} \in i\mathbb{R},$$

$$\tilde{u}_{0,0z} = 0. \tag{G11}$$

(3) The symmetry group is generated by C_{3z}, $\mathcal{T}$, and M_x. In this case, we have Eq. (F24) and

$$\tilde{u}_{0,0z}, \tilde{u}_{0,zz}, \tilde{u}_{0,xy}, \tilde{u}_{1,0x}, \tilde{u}_{2,0x} \in \mathbb{R},$$

$$\tilde{u}_{1,0y}, \tilde{u}_{1,0z}, \tilde{u}_{2,0y}, \tilde{u}_{2,0z} \in i\mathbb{R},$$

$$\tilde{u}_{0,xx} = \tilde{u}_{\sqrt{3},0x} = \tilde{u}_{\sqrt{3},xx} = \tilde{u}_{\sqrt{3},yy} = \tilde{u}_{\sqrt{3},yz} = \tilde{u}_{\sqrt{3},zx} = 0. \tag{G12}$$

(4) The symmetry group is generated by C_{3z}, $\mathcal{T}$, and M_y. In this case, we have Eq. (F25) and

$$\tilde{u}_{0,zz}, \tilde{u}_{0,xy}, \tilde{u}_{\sqrt{3},0y}, \tilde{u}_{\sqrt{3},xy}, \tilde{u}_{\sqrt{3},yx}, \tilde{u}_{\sqrt{3},yz}, \tilde{u}_{\sqrt{3},zx}, \tilde{u}_{\sqrt{3},zz} \in \mathbb{R},$$

$$\tilde{u}_{\sqrt{3},0x}, \tilde{u}_{\sqrt{3},0z}, \tilde{u}_{\sqrt{3},xx}, \tilde{u}_{\sqrt{3},xz}, \tilde{u}_{\sqrt{3},yy}, \tilde{u}_{\sqrt{3},zy} \in i\mathbb{R},$$

$$\tilde{u}_{0,0z} = \tilde{u}_{0,xx} = \tilde{u}_{1,0y} = \tilde{u}_{2,0y} = 0. \tag{G13}$$

(5) The symmetry group is generated by C_{3z}, $\mathcal{T}$, C_{2z}, M_x, and M_y. In this case, we have Eq. (F26) and

$$\tilde{u}_{0,zz}, \tilde{u}_{0,xy}, \tilde{u}_{1,0x}, \tilde{u}_{2,0x}, \tilde{u}_{\sqrt{3},0y}, \tilde{u}_{\sqrt{3},xy}, \tilde{u}_{\sqrt{3},yx}, \tilde{u}_{\sqrt{3},zz} \in \mathbb{R},$$

$$\tilde{u}_{1,0z}, \tilde{u}_{2,0z}, \tilde{u}_{\sqrt{3},0z}, \tilde{u}_{\sqrt{3},xz}, \tilde{u}_{\sqrt{3},zy} \in i\mathbb{R},$$

$$\tilde{u}_{0,0z} = \tilde{u}_{0,xx} = \tilde{u}_{1,0y} = \tilde{u}_{2,0y} = \tilde{u}_{\sqrt{3},0x} = \tilde{u}_{\sqrt{3},xx} = \tilde{u}_{\sqrt{3},yy} = \tilde{u}_{\sqrt{3},yz} = \tilde{u}_{\sqrt{3},zx} = 0. \tag{G14}$$

3. Conservation of z component of spin

In this section we consider the case in which the Hamiltonian commutes with S_z, the generator of spin rotations about the z axis. This operator is defined by

$$S_z|\mathbf{r}\rangle_c = |\mathbf{r}\rangle_c, \quad S_z|s_z\rangle = |s_z\rangle\hbar\sigma_z/2, \tag{G15}$$

and we have

$$[S_z, \tilde{H}_g] = 0 \iff [\tilde{T}_\mathbf{q}, \sigma_0 \otimes \sigma_z] = 0 \quad \text{and} \quad [\tilde{S}_{\eta,\mathbf{q}}, \sigma_0 \otimes \sigma_z] = 0. \tag{G16}$$

When $\tilde{H}_g$ commutes with S_z, we can write

$$\tilde{H}_g = H_{g,\uparrow} \otimes |\uparrow\rangle\langle\uparrow| + H_{g,\downarrow} \otimes |\downarrow\rangle\langle\downarrow| \tag{G17}$$

where $H_{g,\uparrow}$ and $H_{g,\downarrow}$ are spinless Hamiltonians of the form in Eq. (F14). That is to say, we can write

$$H_{g,s} = \int d^2\mathbf{r} |\mathbf{r}\rangle \mathcal{H}_s(\mathbf{r})\langle\mathbf{r}|$$

$$\mathcal{H}_s(\mathbf{r}) = \begin{pmatrix} S_{s,+}(\mathbf{r}) - i\hbar v_F \boldsymbol{\sigma}\cdot\nabla & T_s(\mathbf{r}) \\ T_s^\dagger(\mathbf{r}) & S_{s,-}(\mathbf{r}) - i\hbar v_F \boldsymbol{\sigma}\cdot\nabla \end{pmatrix} \tag{G18}$$

for $s \in \{\uparrow,\downarrow\}$, where

$$\tilde{T}(\mathbf{r}) = T_\uparrow(\mathbf{r}) \otimes \frac{\sigma_0 + \sigma_z}{2} + T_\downarrow(\mathbf{r}) \otimes \frac{\sigma_0 - \sigma_z}{2},$$

$$\tilde{S}_\eta(\mathbf{r}) = S_{\uparrow,\eta}(\mathbf{r}) \otimes \frac{\sigma_0 + \sigma_z}{2} + S_{\downarrow,\eta}(\mathbf{r}) \otimes \frac{\sigma_0 - \sigma_z}{2}. \tag{G19}$$

We expand the T_s and $S_{s,\eta}$ potentials as

$$T_s(\mathbf{r}) = \sum_{\mathbf{q}\in P_M^+} T_{s,\mathbf{q}} e^{i\mathbf{r}\cdot\mathbf{q}}, \quad S_{s,\eta}(\mathbf{r}) = \sum_{\mathbf{q}\in P_M} S_{s,\eta,\mathbf{q}} e^{i\mathbf{r}\cdot\mathbf{q}} \tag{G20}$$

for 2×2 complex matrices $T_{s,\mathbf{q}}$ and $S_{s,\eta,\mathbf{q}}$ with $S_{s,\eta,\mathbf{q}}^\dagger = S_{s,\eta,-\mathbf{q}}$.

Now suppose that $\tilde{H}_g$ commutes with S_z, C_{3z}, and $\mathcal{T}$. By Eq. (G8), $\mathcal{T}$ symmetry implies

$$S_{s,-}(\mathbf{r}) = \sigma_y S_{-s,+}^*(\mathbf{r})\sigma_y \tag{G21}$$

so it suffices to characterize the T_s and $S_{s,+}$ potentials. Additionally, Eq. (G9) holds with

$$\tilde{u}_{1,0x} = \tilde{u}_{1,0y} = \tilde{u}_{2,0x} = \tilde{u}_{2,0y} = \tilde{u}_{0,xx} = \tilde{u}_{0,xy} = \tilde{u}_{\sqrt{3},0x} = \tilde{u}_{\sqrt{3},0y} = \tilde{u}_{\sqrt{3},xx} = \tilde{u}_{\sqrt{3},xy} = \tilde{u}_{\sqrt{3},zx} = \tilde{u}_{\sqrt{3},zy} = 0. \tag{G22}$$

We can then write

$$T_{s,\mathbf{q}_j} = T_{\mathbf{q}_j} + s\tilde{u}_{1,0z}\sigma_0, \quad T_{s,-2\mathbf{q}_j} = T_{-2\mathbf{q}_j} + s\tilde{u}_{2,0z}\sigma_0, \quad S_{s,+,\mathbf{0}} = S_{+,\mathbf{0}} + s\tilde{u}_{0,0z}\sigma_0 + s\tilde{u}_{0,zz}\sigma_z,$$

$$S_{s,+,\mathbf{q}_{1+j}-\mathbf{q}_{2+j}} = S_{+,\mathbf{q}_{1+j}-\mathbf{q}_{2+j}} + s\tilde{u}_{\sqrt{3},0z}\sigma_0 + s\tilde{u}_{\sqrt{3},xz}\boldsymbol{\sigma}\cdot\hat{\mathbf{n}}_{\zeta_j}$$
$$+ s\tilde{u}_{\sqrt{3},yz}\boldsymbol{\sigma}\cdot\hat{\mathbf{n}}_{\zeta_j+\pi/2} + s\tilde{u}_{\sqrt{3},zz}\sigma_z,$$

$$S_{s,+,\mathbf{q}_{2+j}-\mathbf{q}_{1+j}} = S_{s,+,\mathbf{q}_{1+j}-\mathbf{q}_{2+j}}^\dagger, \tag{G23}$$

for $s \in \{\uparrow,\downarrow\}$, where we have made the identification $\uparrow = +$, $\downarrow = -$, and where the $T_\mathbf{q}$ and $S_{+,\mathbf{q}}$ matrices are given by Eq. (F21). In the special case that $\tilde{H}_g$ commutes with S_z, C_{3z}, $\mathcal{T}$, C_{2z}, M_x, and M_y, Eqs. (F27) and (G14) allows us to summarize this more succinctly as

$$T_{s,m\mathbf{q}_j} = s\tilde{w}_{|m|,0}i\sigma_0 + w_{|m|,y}\boldsymbol{\sigma}\cdot\hat{\mathbf{n}}_{\zeta_j+\pi/2} + w_{|m|,z}i\sigma_z,$$

$$S_{s,+,\mathbf{0}} = w_{0,0}\sigma_0 + s\tilde{w}_{0,z}\sigma_z,$$

$$S_{s,+,\gamma(\mathbf{q}_{1+j}-\mathbf{q}_{2+j})} = (w_{\sqrt{3},0} + s\gamma\tilde{w}_{\sqrt{3},0}i)\sigma_0 + (w_{\sqrt{3},x} + s\gamma\tilde{w}_{\sqrt{3},x}i)\boldsymbol{\sigma}\cdot\hat{\mathbf{n}}_{\zeta_j} + (s\tilde{w}_{\sqrt{3},z} + \gamma w_{\sqrt{3},z}i)\sigma_z, \tag{G24}$$

for $m \in \{1,-2\}$, $\gamma \in \{+,-\}$, and $s \in \{\uparrow,\downarrow\}$, where the real $\tilde{w}$ parameters are defined by

$$\tilde{w}_{1,0} = -i\tilde{u}_{1,z}, \quad \tilde{w}_{2,0} = -i\tilde{u}_{2,z}, \quad \tilde{w}_{0,z} = \tilde{u}_{0,zz}, \quad \tilde{w}_{\sqrt{3},0} = -i\tilde{u}_{\sqrt{3},0z}, \quad \tilde{w}_{\sqrt{3},x} = -i\tilde{u}_{\sqrt{3},xz}, \quad \tilde{w}_{\sqrt{3},z} = \tilde{u}_{\sqrt{3},zz}. \tag{G25}$$

4. Transformation to the moiré coordinate system

Since the model for spin $s \in \{\uparrow,\downarrow\}$ described in Appendix G 3 is of the form described in Appendix D 1, we can transform it into the moiré coordinate system defined in Appendix E just as we did in Appendix F 3. Equations (G21) and (G23) imply

$$S_{\xi,s,-}(\mathbf{r}) = \sigma_y S_{\xi,-s,+}^*(\mathbf{r})\sigma_y \tag{G26}$$

and

$$T_{\xi,s,\mathbf{q}_j} = T_{\xi,\mathbf{q}_j} + s\tilde{u}_{1,0z}\sigma_0, \quad T_{\xi,s,-2\mathbf{q}_j} = T_{-2\mathbf{q}_j} + s\tilde{u}_{2,0z}\sigma_0, \quad S_{\xi,s,+,\mathbf{0}} = S_{\xi,+,\mathbf{0}} + s\tilde{u}_{0,0z}\sigma_0 + s\tilde{u}_{0,zz}\sigma_z,$$

$$S_{\xi,s,+,\mathbf{q}_{1+j}-\mathbf{q}_{2+j}} = S_{\xi,+,\mathbf{q}_{1+j}-\mathbf{q}_{2+j}} + s\tilde{u}_{\sqrt{3},0z}\sigma_0 + s\tilde{u}_{\sqrt{3},xz}\boldsymbol{\sigma}\cdot\hat{\mathbf{n}}_{\zeta_j-\xi} + s\tilde{u}_{\sqrt{3},yz}\boldsymbol{\sigma}\cdot\hat{\mathbf{n}}_{\zeta_j+\pi/2-\xi} + s\tilde{u}_{\sqrt{3},zz}\sigma_z,$$

$$S_{\xi,s,+,\mathbf{q}_{2+j}-\mathbf{q}_{1+j}} = S_{\xi,s,+,\mathbf{q}_{1+j}-\mathbf{q}_{2+j}}^\dagger, \tag{G27}$$

where the $T_{\mathbf{q}}$ and $S_{+,\mathbf{q}}$ matrices are given by Eq. (F30). Additionally, Eq. (G24) implies

$$T_{\xi,s,m\mathbf{q}_j} = s\tilde{w}_{|m|,0}i\sigma_0 + w_{|m|,y}\boldsymbol{\sigma}\cdot\hat{\mathbf{n}}_{\zeta_j+\phi_1} + w_{|m|,z}i\sigma_z,$$

$$S_{\xi,s,+,\mathbf{0}} = w_{0,0}\sigma_0 + s\tilde{w}_{0,z}\sigma_z,$$

$$S_{\xi,s,+,\gamma(\mathbf{q}_{1+j}-\mathbf{q}_{2+j})} = (w_{\sqrt{3},0} + s\gamma\tilde{w}_{\sqrt{3},0}i)\sigma_0 + (w_{\sqrt{3},x} + s\gamma\tilde{w}_{\sqrt{3},x}i)\boldsymbol{\sigma}\cdot\hat{\mathbf{n}}_{\zeta_j+\phi_1-\pi/2} + (s\tilde{w}_{\sqrt{3},z} + \gamma w_{\sqrt{3},z}i)\sigma_z. \tag{G28}$$

for $m \in \{1,-2\}$, $\gamma \in \{+,-\}$, and $s \in \{\uparrow,\downarrow\}$, where ϕ_1 is defined by Eq. (F32).

5. Coirrep decomposition for the bottom layer

In this section, we consider the effect of spin on the corepresentation theory analysis in Appendix F 4. We begin by generalizing Eq. (F33) to

$$C_{3z}(|\mathbf{r}\rangle_g \otimes |s_z\rangle) = |R_{2\pi/3}\mathbf{r}\rangle_g(e^{i(2\pi/3)\sigma_z\otimes\sigma_z} \otimes e^{-i(\pi/3)\sigma_z}) \oplus \tilde{C}_{3z,-},$$

$$C_{2z}(|\mathbf{r}\rangle_g \otimes |s_z\rangle) = |-\mathbf{r}\rangle_g(\sigma_x \otimes \sigma_x \otimes e^{-i(\pi/2)\sigma_z}) \oplus \tilde{C}_{2z,-},$$

$$M_x(|\mathbf{r}\rangle_g \otimes |s_z\rangle) = |\mathcal{R}_{\hat{\mathbf{x}}}\mathbf{r}\rangle_g(\sigma_x \otimes \sigma_0 \otimes e^{-i(\pi/2)\sigma_x}) \oplus \tilde{M}_{x,-},$$

$$M_y(|\mathbf{r}\rangle_g \otimes |s_z\rangle) = |\mathcal{R}_{\hat{\mathbf{y}}}\mathbf{r}\rangle_g(\sigma_0 \otimes \sigma_x \otimes e^{-i(\pi/2)\sigma_y}) \oplus \tilde{M}_{y,-},$$

$$\mathcal{T}(|\mathbf{r}\rangle_g \otimes |s_z\rangle) = |\mathbf{r}\rangle_g(\sigma_x \otimes \sigma_0 \otimes \sigma_y) \oplus \tilde{\mathcal{T}}_-, \tag{G29}$$

for some unitary matrices $\tilde{C}_{3z,-}$, $\tilde{C}_{2z,-}$, $\tilde{M}_{x,-}$, $\tilde{M}_{y,-}$, and $\tilde{\mathcal{T}}_-$, which act on the bottom layer including spin. Eq. (F34) then generalizes to

$$[C_{3z}, \tilde{H}_c] = 0 \iff \tilde{T}_{\eta,\mathbf{q}_{j+1}} = (e^{i\eta(2\pi/3)\sigma_z} \otimes e^{-i(\pi/3)\sigma_z})\tilde{T}_{\eta,\mathbf{q}_j}\tilde{C}_{3z,-}^\dagger$$

$$[C_{2z}, \tilde{H}_c] = 0 \iff \tilde{T}_{\eta,\mathbf{q}_j} = (\sigma_x \otimes e^{-i(\pi/2)\sigma_z})\tilde{T}_{-\eta,\mathbf{q}_j}\tilde{C}_{2z,-}^\dagger$$

$$[M_x, \tilde{H}_c] = 0 \iff \tilde{T}_{\eta,\mathbf{q}_1} = (\sigma_0 \otimes e^{-i(\pi/2)\sigma_x})\tilde{T}_{-\eta,\mathbf{q}_1}\tilde{M}_{x,-}^\dagger$$

$$\tilde{T}_{\eta,\mathbf{q}_2} = (\sigma_0 \otimes e^{-i(\pi/2)\sigma_x})\tilde{T}_{-\eta,\mathbf{q}_3}\tilde{M}_{x,-}$$

$$\tilde{T}_{\eta,\mathbf{q}_3} = (\sigma_0 \otimes e^{-i(\pi/2)\sigma_x})\tilde{T}_{-\eta,\mathbf{q}_2}\tilde{M}_{x,-}^\dagger$$

$$[M_y, \tilde{H}_c] = 0 \iff \tilde{T}_{\eta,\mathbf{q}_1} = (\sigma_x \otimes e^{-i(\pi/2)\sigma_y})\tilde{T}_{\eta,\mathbf{q}_1}\tilde{M}_{y,-}^\dagger$$

$$\tilde{T}_{\eta,\mathbf{q}_2} = (\sigma_x \otimes e^{-i(\pi/2)\sigma_y})\tilde{T}_{\eta,\mathbf{q}_3}\tilde{M}_{y,-}^\dagger$$

$$\tilde{T}_{\eta,\mathbf{q}_3} = (\sigma_x \otimes e^{-i(\pi/2)\sigma_y})\tilde{T}_{\eta,\mathbf{q}_2}\tilde{M}_{y,-}^\dagger$$

$$[\mathcal{T}, \tilde{H}_c] = 0 \iff \tilde{T}_{\eta,\mathbf{q}_j} = (\sigma_0 \otimes \sigma_y)\tilde{T}_{-\eta,\mathbf{q}_j}^*\tilde{\mathcal{T}}_-^\dagger. \tag{G30}$$

As in Appendix F 4, in the presence of C_{3z} and $\mathcal{T}$ symmetries, all of the $\tilde{T}_{\eta,\mathbf{q}_j}$ matrices are determined by $\tilde{T}_{+,\mathbf{q}_1}$ through the equations

$$\tilde{T}_{\eta,\mathbf{q}_j} = (e^{i\eta\zeta_j\sigma_z} \otimes e^{-i(\zeta_j/2)\sigma_z})\tilde{T}_{\eta,\mathbf{q}_1}\tilde{C}_{3z,-}^{1-j}$$

$$\tilde{T}_{-,\mathbf{q}_1} = (\sigma_0 \otimes \sigma_y)\tilde{T}_{+,\mathbf{q}_1}^*\tilde{\mathcal{T}}_-^\dagger. \tag{G31}$$

C_{2z}, M_x, and M_y symmetries imply the constraints

$$[C_{2z}, \tilde{H}_c] = 0 \Rightarrow \tilde{T}_{+,\mathbf{q}_1} = -(\sigma_x \otimes \sigma_x)\tilde{T}_{+,\mathbf{q}_1}^*(\tilde{C}_{2z,-}\tilde{\mathcal{T}}_-)^\dagger, \tag{G32}$$

$$[M_x, \tilde{H}_c] = 0 \Rightarrow \tilde{T}_{+,\mathbf{q}_1} = (\sigma_0 \otimes \sigma_z)\tilde{T}_{+,\mathbf{q}_1}^*(\tilde{M}_{x,-}\tilde{\mathcal{T}}_-)^\dagger, \tag{G33}$$

$$[M_y, \tilde{H}_c] = 0 \Rightarrow \tilde{T}_{+,\mathbf{q}_1} = -i(\sigma_x \otimes \sigma_y)\tilde{T}_{+,\mathbf{q}_1}\tilde{M}_{y,-}^\dagger. \tag{G34}$$

By Eqs. (G2) and (G4), we have

$$\tilde{T}(\mathbf{r}) = -\sum_{j,k=1}^3 \tilde{T}_{+,\mathbf{q}_j}\tilde{\mathcal{H}}_-^{-1}\tilde{T}_{-,\mathbf{q}_k}^\dagger(\sigma_y \otimes \sigma_0)e^{-i\mathbf{r}\cdot(\mathbf{q}_k+\mathbf{q}_j)} \tag{G35}$$

$$= -\sum_{j,k=1}^3 (e^{i\zeta_j\sigma_z} \otimes e^{-i(\zeta_j/2)\sigma_z})\tilde{T}_{+,\mathbf{q}_1}\tilde{C}_{3z,-}^{1-j}\tilde{\mathcal{H}}_-^{-1}\tilde{C}_{3z,-}^{k-1}\tilde{\mathcal{T}}_-\tilde{T}_{+,\mathbf{q}_1}^T(\sigma_y \otimes \sigma_y)(e^{-i\zeta_k\sigma_z} \otimes e^{i(\zeta_k/2)\sigma_z})e^{-i\mathbf{r}\cdot(\mathbf{q}_k+\mathbf{q}_j)}, \tag{G36}$$

$$\tilde{S}_+(\mathbf{r}) = -\sum_{j,k=1}^{3} \tilde{T}_{+,\mathbf{q}_j} \tilde{\mathcal{H}}_-^{-1} \tilde{T}_{+,\mathbf{q}_k}^{\dagger} e^{i\mathbf{r}\cdot(\mathbf{q}_k-\mathbf{q}_j)} \tag{G37}$$

$$= -\sum_{j,k=1}^{3} (e^{i\zeta_j\sigma_z} \otimes e^{-i(\zeta_j/2)\sigma_z}) \tilde{T}_{+,\mathbf{q}_1} \tilde{C}_{3z,-}^{1-j} \tilde{\mathcal{H}}_-^{-1} \tilde{C}_{3z,-}^{k-1} \tilde{T}_{+,\mathbf{q}_1}^{\dagger} (e^{-i\zeta_k\sigma_z} \otimes e^{i(\zeta_k/2)\sigma_z}) e^{i\mathbf{r}\cdot(\mathbf{q}_k-\mathbf{q}_j)}. \tag{G38}$$

By the same argument as in Appendix F 4, it is possible to use Eqs. (G36) and (G38) to write $\tilde{T}(\mathbf{r})$ and $\tilde{S}^+(\mathbf{r})$ as a sum over the coirreps present on the bottom layer at $\mathbf{\Gamma}_-$. Note that if we use $\mathcal{T}$ symmetry twice, we find

$$\tilde{T}_{+,\mathbf{q}_1} = (\sigma_0 \otimes \sigma_y)((\sigma_0 \otimes \sigma_y)\tilde{T}_{+,\mathbf{q}_1}^* \tilde{\mathcal{T}}_-^{\dagger})^* \tilde{\mathcal{T}}_-^{\dagger} = \tilde{T}_{+,\mathbf{q}_1}(-\tilde{\mathcal{T}}_-\tilde{\mathcal{T}}_-^*)^{\dagger} \tag{G39}$$

so that either $\tilde{\mathcal{T}}_-\tilde{\mathcal{T}}_-^* = -1$ or $\tilde{T}_{+,\mathbf{q}_1} = 0$. As a result, it suffices to consider only the spinful coirreps in Table III. We could write a straightforward adaptation of Appendices F 4 a–F 4 e to the spinful case, considering coirreps $\overline{EE}$ and $^1\overline{E}^2\overline{E}$ for $31'$, coirreps $^2\overline{E}_1{}^1\overline{E}_1$, $^1\overline{E}_3{}^2\overline{E}_3$, and $^1\overline{E}_2{}^2\overline{E}_2$ for $61'$, coirreps $^2\overline{E}^1\overline{E}$ and $\overline{E}_1$ for $3m1'$, and coirreps $\overline{E}_3$, $\overline{E}_2$, and $\overline{E}_1$ for $6mm1'$. Such an analysis would cover all possibilities including spin-orbit coupling in both the bottom layer and in the interlayer couplings. However, the formulas would contain sixteen complex parameters in the case of the spinful point group $31'$ and would not be particularly illuminating.

For these reasons, we focus instead on the more physically realistic case of weak spin-orbit coupling. Specifically, we make the approximation that spin-orbit coupling affects only the bottom layer Hamiltonian and not the interlayer coupling. We take

$$\tilde{T}_\eta(\mathbf{r}) = T_\eta(\mathbf{r}) \otimes \sigma_0, \quad \tilde{\mathcal{H}}_- = \mathcal{H}_- \otimes \sigma_0 + \mathcal{H}_{SO,-}, \quad \tilde{C}_{3z,-} = C_{3z,-} \otimes e^{-i(\pi/3)\sigma_z}, \quad \tilde{C}_{2z,-} = C_{2z,-} \otimes e^{-i(\pi/2)\sigma_z},$$

$$\tilde{M}_{x,-} = M_{x,-} \otimes e^{-i(\pi/2)\sigma_x}, \quad \tilde{M}_{y,-} = M_{y,-} \otimes e^{-i(\pi/2)\sigma_y}, \quad \tilde{\mathcal{T}}_- = \mathcal{T}_- \otimes \sigma_y, \tag{G40}$$

where $\mathcal{H}_{SO,-}$ is the spin-orbit coupling Hamiltonian at $\mathbf{\Gamma}_-$, which we assume is independent of momentum. As in Appendix F 4, we block diagonalize the spinless part of the corepresentation (i.e., $C_{3z,-}, C_{2z,-}, M_{x,-}, M_{y,-}, \mathcal{T}_-$) along with $\mathcal{H}_-$. Since $\tilde{T}(\mathbf{r})$ and $\tilde{S}_+(\mathbf{r})$ in Eqs. (G36) and (G38) are additive over these spinless coirreps, we now consider each spinless coirrep separately.

We first consider the case of a one-dimensional spinless coirrep. In this case, the full corepresentation in Eq. (G40) is two-dimensional. Kramers' theorem implies that spinful corepresentations cannot be one-dimensional, so the corepresentation must be irreducible. It follows that $\tilde{\mathcal{H}}_0 = E_0\sigma_0$ and $\mathcal{H}_{SO,-} = 0$. Eqs. (G36) and (G38) imply

$$\tilde{T}(\mathbf{r}) = T(\mathbf{r}) \otimes \sigma_0, \quad \tilde{S}_+(\mathbf{r}) = S_+(\mathbf{r}) \otimes \sigma_0, \tag{G41}$$

where $T(\mathbf{r})$ and $S_+(\mathbf{r})$ are given by Eqs. (F40) and (F42) with $\mathcal{H}_- = E_0$.

Next, suppose that the spinless coirrep is $^2E^1E$ for spinless point group $31'_0$. The full corepresentation in Eq. (G40) is then $^2E^1E \otimes {}^1\overline{E}^2\overline{E}$, which decomposes as

$$^2E^1E \otimes {}^1\overline{E}^2\overline{E} \cong \overline{EE} \oplus {}^1\overline{E}^2\overline{E}. \tag{G42}$$

Furthermore, if we take $C_{3z,-} = e^{-i(2\pi/3)\sigma_z}$ as in Appendix F 4 a, then

$$\tilde{C}_{3z,-} = e^{-i(2\pi/3)\sigma_z} \otimes e^{-i(\pi/3)\sigma_z} = \begin{pmatrix} -1 & 0 & 0 & 0 \\ 0 & e^{-i(\pi/3)} & 0 & 0 \\ 0 & 0 & e^{i(\pi/3)} & 0 \\ 0 & 0 & 0 & -1 \end{pmatrix}, \tag{G43}$$

which makes the coirrep decomposition explicit. It follows that we can write

$$\tilde{\mathcal{H}}_-^{-1} = \frac{1}{E_0}\sigma_0 \otimes \sigma_0 + \frac{\lambda}{E_0}\sigma_z \otimes \sigma_z \tag{G44}$$

where E_0 is the harmonic mean of the energies at $\mathbf{\Gamma}_-$ and λ is a real dimensionless parameter that controls the spin-orbit coupling strength. In the case of weak spin-orbit coupling, we will have $|\lambda| \ll 1$ and note that $\lambda = 0$ corresponds to vanishing spin-orbit coupling.

Equations (G36) and (G38) imply

$$\tilde{T}(\mathbf{r}) = T(\mathbf{r}) \otimes \sigma_0 + \lambda T_{SO}(\mathbf{r}) \otimes \sigma_z, \quad \tilde{S}_+(\mathbf{r}) = S_+(\mathbf{r}) \otimes \sigma_0 + \lambda S_{SO,+}(\mathbf{r}) \otimes \sigma_z, \tag{G45}$$

where $T(\mathbf{r})$ and $S_+(\mathbf{r})$ are given by Eqs. (F40) and (F42) with $\mathcal{H}_- = E_0\sigma_0$ while $T_{SO}(\mathbf{r})$ and $S_{SO,+}(\mathbf{r})$ are given by Eqs. (F40) and (F42) with $\mathcal{H}_- = E_0\sigma_z$. It is clear from Eq. (G45) that $[S_z, \tilde{H}_g] = 0$, which is the case that was discussed in Appendix G 3. If we parametrize $T_{+,\mathbf{q}_1}$ as in Eq. (F45) then $\tilde{T}(\mathbf{r})$ and $\tilde{S}_+(\mathbf{r})$ are given by Eqs. (G19), (G20) and (G23) where the $T_\mathbf{q}$ and $S_{+,\mathbf{q}}$ matrices are given in terms of the v_0, v_x, v_y, and v_z parameters by Eqs. (F21) and (F46), and

additionally

$$\tilde{u}_{1,0z} = \frac{i\lambda}{E_0}(v_0^2 + 2v_x^2 + 2v_y^2 - v_z^2), \quad \tilde{u}_{2,0z} = -\frac{i\lambda}{E_0}(v_0^2 - v_x^2 - v_y^2 - v_z^2),$$

$$\tilde{u}_{0,0z} = -\frac{3\lambda}{E_0}(v_0 v_z^* + v_0^* v_z - i(v_x v_y^* - v_x^* v_y)), \quad \tilde{u}_{0,zz} = -\frac{3\lambda}{E_0}(|v_0|^2 - |v_x|^2 - |v_y|^2 + |v_z|^2),$$

$$\tilde{u}_{\sqrt{3},0z} = \frac{\lambda}{2E_0}(v_0 v_z^* + v_0^* v_z + 2i(v_x v_y^* - v_x^* v_y) + i\sqrt{3}(|v_0|^2 + |v_z|^2)),$$

$$\tilde{u}_{\sqrt{3},xz} = \frac{\lambda}{2E_0}(v_x v_z^* + v_x^* v_z - i(v_0 v_y^* - v_0^* v_y) + \sqrt{3}(v_y v_z^* - v_y^* v_z) - i\sqrt{3}(v_0 v_x^* + v_0^* v_x)),$$

$$\tilde{u}_{\sqrt{3},yz} = \frac{\lambda}{2E_0}(v_y v_z^* + v_y^* v_z + i(v_0 v_x^* - v_0^* v_x) - \sqrt{3}(v_x v_z^* - v_x^* v_z) - i\sqrt{3}(v_0 v_y^* + v_0^* v_y)),$$

$$\tilde{u}_{\sqrt{3},zz} = \frac{\lambda}{2E_0}(|v_0|^2 + 2|v_x|^2 + 2|v_y|^2 + |v_z|^2 + i\sqrt{3}(v_0 v_z^* + v_0^* v_z)). \tag{G46}$$

Finally, we consider the other possible spinless coirreps. The spinless coirrep could be $^2E_1{}^1E_1$ or $^2E_2{}^1E_2$ for $61'_0$, E for $3m1'$, or E_2 or E_1 for $6mm1'$. However, the conventions we chose in Appendices F 4 b–F 4 e imply that Eq. (G43) is satisfied in each case, and in fact the above calculation applies for each coirrep. The distinctions are only in the constraints placed on the v_0, v_x, v_y, and v_z parameters, which are listed for each coirrep in Appendices F 4 b–F 4 e.

For the case of spinless point group $6mm1'$, Eq. (G23) simplifies to Eq. (G24) where the w parameters are given by Eq. (F59) and

$$\tilde{w}_{1,0} = \frac{\lambda}{E_0}(v_0^2 + 2v_x^2), \quad \tilde{w}_{2,0} = -\frac{\lambda}{E_0}(v_0^2 - v_x^2), \quad \tilde{w}_{0,z} = -\frac{3\lambda}{E_0}(|v_0|^2 - |v_x|^2),$$

$$\tilde{w}_{\sqrt{3},0} = \frac{\lambda\sqrt{3}}{2E_0}|v_0|^2, \quad \tilde{w}_{\sqrt{3},x} = -\frac{\lambda\sqrt{3}}{2E_0}(v_0 v_x^* + v_0^* v_x), \quad \tilde{w}_{\sqrt{3},z} = \frac{\lambda}{2E_0}(|v_0|^2 + 2|v_x|^2). \tag{G47}$$

Additionally, $v_0, v_x \in \mathbb{R}$ for coirrep E_2 and $v_0, v_x \in i\mathbb{R}$ for coirrep E_1.

APPENDIX H: OPPOSITE-VELOCITY MODEL

We now consider the construction of Appendix D 2 specifically in the case of the type I+ configuration with $\epsilon_0 = 0$, $\theta_0 = 0$. In this case, we have $N_- = 1$ and we can take $\xi_0 = 0$ so that Eq. (D13) implies

$$\mathbf{q}_j = (e^{-\epsilon}R_\theta - 1)R_{\zeta_j}\mathbf{K}_+. \tag{H1}$$

For simplicity, we ignore spin in this Appendix. We do not need to assume that either layer is graphene, though we do require both layers to have triangular Bravais lattices and Dirac cones at their $\mathbf{K}$ and $-\mathbf{K}$ points centered at their Fermi energies. Furthermore, we require that the symmetries C_{3z} (rotation by angle $2\pi/3$ about $\hat{\mathbf{z}}$), C_{2z} (rotation by angle π about $\hat{\mathbf{z}}$), M_x (reflection through the yz plane), M_y (reflection through the xz plane), and $\mathcal{T}$ (antiunitary time-reversal with $\mathcal{T}^2 = 1$) take the same form on the Dirac cones as they do in graphene. As in Appendix D 2, we focus on the valley containing $\mathbf{K}_+$ and $\mathbf{K}_-$, which is preserved by C_{3z}, $C_{2z}\mathcal{T}$, and M_y. Using the states $|\mathbf{r}\rangle$ in Eq. (D25), we then have

$$C_{3z}|\mathbf{r}\rangle = |R_{2\pi/3}\mathbf{r}\rangle\sigma_0 \otimes e^{i(2\pi/3)\sigma_z},$$

$$C_{2z}\mathcal{T}|\mathbf{r}\rangle = |-\mathbf{r}\rangle\sigma_0 \otimes \sigma_x,$$

$$M_y|\mathbf{r}\rangle = |\mathcal{R}_{\hat{\mathbf{y}}}\mathbf{r}\rangle\sigma_0 \otimes \sigma_x. \tag{H2}$$

Here, the first (second) Pauli matrix in each tensor product acts on layer (sublattice).

We now take a unitary change of basis

$$|\mathbf{r}\rangle_o = |\mathbf{r}\rangle\begin{pmatrix} \sigma_0 & 0 \\ 0 & i\sigma_z \end{pmatrix} \tag{H3}$$

under which the Hamiltonian in Eq. (D9) becomes

$$H = \int d^2\mathbf{r}|\mathbf{r}\rangle_o\tilde{\mathcal{H}}(\mathbf{r})\langle\mathbf{r}|_o$$

$$\tilde{\mathcal{H}}(\mathbf{r}) = \begin{pmatrix} \tilde{S}_+(\mathbf{r}) - i\hbar v_+\boldsymbol{\sigma} \cdot \nabla & \tilde{T}(\mathbf{r}) \\ \tilde{T}^\dagger(\mathbf{r}) & \tilde{S}_-(\mathbf{r}) + i\hbar v_-\boldsymbol{\sigma} \cdot \nabla \end{pmatrix} \tag{H4}$$

where

$$\tilde{S}_+(\mathbf{r}) = S_+(\mathbf{r}), \quad \tilde{S}_-(\mathbf{r}) = \sigma_z S_-(\mathbf{r})\sigma_z, \quad \tilde{T}(\mathbf{r}) = iT(\mathbf{r})\sigma_z. \tag{H5}$$

Additionally, Eq. (H2) implies

$$C_{3z}|\mathbf{r}\rangle_o = |R_{2\pi/3}\mathbf{r}\rangle_o\sigma_0 \otimes e^{i(2\pi/3)\sigma_z},$$

$$C_{2z}\mathcal{T}|\mathbf{r}\rangle_o = |-\mathbf{r}\rangle_o\sigma_0 \otimes \sigma_x,$$

$$M_y|\mathbf{r}\rangle_o = |\mathcal{R}_{\hat{\mathbf{y}}}\mathbf{r}\rangle_o\sigma_z \otimes \sigma_x. \tag{H6}$$

Interestingly, this form for the C_{3z}, $C_{2z}\mathcal{T}$, and M_y symmetries is equivalent to that implied by Eq. (F18) for the coupled-valley graphene model. With this motivation, we define the emergent C_{2z} operator

$$\tilde{C}_{2z} = -|-\mathbf{r}\rangle\sigma_y \otimes \sigma_z. \tag{H7}$$

We expand the potentials as

$$\tilde{T}(\mathbf{r}) = \sum_{\mathbf{q} \in P_M^+} \tilde{T}_{\mathbf{q}} e^{i\mathbf{r}\cdot\mathbf{q}}, \quad \tilde{S}_l(\mathbf{r}) = \sum_{\mathbf{q} \in P_M} \tilde{S}_{l,\mathbf{q}} e^{i\mathbf{r}\cdot\mathbf{q}}, \tag{H8}$$

for 2×2 complex matrices $T_{\mathbf{q}}$ and $\tilde{S}_{l,\mathbf{q}}$ with $\tilde{S}_{l,\mathbf{q}}^{\dagger} = \tilde{S}_{l,-\mathbf{q}}$. Applying the arguments of Appendix F 2, we find

$$[C_{3z}, H] = 0 \iff \tilde{T}_{R_{2\pi/3}\mathbf{q}} = e^{i(2\pi/3)\sigma_z} \tilde{T}_{\mathbf{q}} e^{-i(2\pi/3)\sigma_z} \quad \text{and}$$

$$\tilde{S}_{l,R_{2\pi/3}\mathbf{q}} = e^{i(2\pi/3)\sigma_z} \tilde{S}_{l,\mathbf{q}} e^{-i(2\pi/3)\sigma_z},$$

$$[C_{2z}\mathcal{T}, H] = 0 \iff \tilde{T}_{\mathbf{q}} = \sigma_x \tilde{T}_{\mathbf{q}}^* \sigma_x \quad \text{and} \quad \tilde{S}_{l,\mathbf{q}} = \sigma_x \tilde{S}_{l,\mathbf{q}}^* \sigma_x,$$

$$[M_y, H] = 0 \iff \tilde{T}_{\mathcal{R}_{\hat{\mathbf{s}}}\mathbf{q}} = -\sigma_x \tilde{T}_{\mathbf{q}} \sigma_x \quad \text{and}$$

$$\tilde{S}_{l,\mathcal{R}_{\hat{\mathbf{s}}}\mathbf{q}} = \sigma_x \tilde{S}_{l,\mathbf{q}} \sigma_x,$$

$$[\tilde{C}_{2z}, H] = 0 \iff \tilde{T}_{\mathbf{q}} = -\sigma_z \tilde{T}_{\mathbf{q}}^{\dagger} \sigma_z, \tilde{S}_{+,-\mathbf{q}} = \sigma_z \tilde{S}_{-,\mathbf{q}} \sigma_z, \quad \text{and} \quad v_- = -v_+. \tag{H9}$$

To lowest order, we only need to keep terms of the form

$$\tilde{T}_{\mathbf{q}_j}, \quad \tilde{S}_{l,\mathbf{0}}. \tag{H10}$$

Using C_{3z}, $C_{2z}\mathcal{T}$, and Hermiticity, we can then write

$$\tilde{T}_{\mathbf{q}_j} = \tilde{w}_0 \sigma_0 + \tilde{w}_1 \boldsymbol{\sigma} \cdot \hat{\mathbf{n}}_{\zeta_j} + w_1 \boldsymbol{\sigma} \cdot \hat{\mathbf{n}}_{\zeta_j + \pi/2} + i w_0 \sigma_z,$$

$$\tilde{S}_{l,\mathbf{0}} = \left(E_F + \frac{lE_\Delta}{2} \right) \sigma_0, \tag{H11}$$

for real parameters w_0, w_1, $\tilde{w}_0$, $\tilde{w}_1$, E_F, and E_Δ. If M_y is also preserved then additionally $\tilde{w}_0 = \tilde{w}_1 = 0$. If we additionally have $E_\Delta = 0$ and $v_- = -v_+$ then $[\tilde{C}_{2z}, H] = 0$.

Finally, we transform to the moiré coordinate system as described in Appendix E. The $\tilde{T}_{\mathbf{q}_j}$ and $\tilde{S}_{l,\mathbf{0}}$ matrices are then replaced by

$$\tilde{T}_{\xi,\mathbf{q}_j} = \tilde{w}_0 \sigma_0 + \tilde{w}_1 \boldsymbol{\sigma} \cdot \hat{\mathbf{n}}_{\zeta_j + \phi_1 - \pi/2} + w_1 \boldsymbol{\sigma} \cdot \hat{\mathbf{n}}_{\zeta_j + \phi_1} + i w_0 \sigma_z,$$

$$\tilde{S}_{\xi,l,\mathbf{0}} = \left(E_F + \frac{lE_\Delta}{2} \right) \sigma_0, \tag{H12}$$

where

$$\phi_1 = \pi/2 - \xi = \arg(1 - e^{-\delta\epsilon - i\delta\theta}) \tag{H13}$$

since $\xi_0 = 0$.

APPENDIX I: MAGNETIC POINT GROUPS

The spinful magnetic point group $6mm1'$ is generated by three elements C_{6z}, M_y, and $\mathcal{T}$, which satisfy the relations

$$\mathcal{T}^4 = 1, \quad C_{6z}^6 = M_y^2 = (C_{6z}M_y)^2 = \mathcal{T}^2, \quad C_{6z}\mathcal{T} = \mathcal{T}C_{6z},$$

$$M_y\mathcal{T} = \mathcal{T}M_y. \tag{I1}$$

We further define group elements

$$-1 = \mathcal{T}^2, \quad C_{3z} = C_{6z}^2, \quad C_{2z} = C_{6z}^3, \quad M_x = C_{2z}M_y^{-1}, \tag{I2}$$

and subgroups

$$31' = \langle C_{3z}, \mathcal{T} \rangle, \tag{I3}$$

$$61' = \langle C_{6z}, \mathcal{T} \rangle, \tag{I4}$$

$$mm21' = \langle M_x, M_y, \mathcal{T} \rangle, \tag{I5}$$

$$3m1' = \langle C_{3z}, M_x, \mathcal{T} \rangle \text{ or } \langle C_{3z}, M_y, \mathcal{T} \rangle, \tag{I6}$$

where $\langle x_1, \ldots, x_k \rangle$ indicates the subgroup generated by elements $x_1, \ldots, x_k$. Note that Eq. (I6) gives two expressions for $3m1'$, which are different subgroups of $6mm1'$ but are isomorphic. Information about these groups is available on the Bilbao Crystallographic Server [30,43,44,60,61].

For each of these spinful magnetic point groups, we define a corresponding spinless magnetic point group produced by taking the quotient with the normal subgroup $\{1, -1\}$. Equivalently, we replace the condition $\mathcal{T}^4 = 1$ by $\mathcal{T}^2 = 1$. We use a subscript 0 to differentiate the spinless groups from the spinful groups, so that we have defined $31'_0$, $61'_0$, $mm21'_0$, $3m1'_0$, and $6mm1'_0$.

The character tables for the spinful magnetic point groups, enumerating the coirreps in which $\mathcal{T}$ is represented by an antilinear operator, are given in Table III. For the case of $3m1'$, we use M in place of M_x or M_y to emphasize that both definitions yield the same character table. In each coirrep, the element -1 is either represented by 1 or by -1. Coirreps in which -1 is represented by 1 are also coirreps of the corresponding spinless magnetic point group. As a result, Table III also effectively contains the character tables for the spinless magnetic point groups. Additionally, we say that a corepresentation is spinless (spinful) if it represents -1 by 1 (-1).

APPENDIX J: PARAMETER CHOICES FOR THE PHASE DIAGRAM OF LOW-ENERGY BANDS

In this section, we justify the parameter choices that were made to simplify the phase diagram of low-energy bands in Fig. 2(b). We consider the Hamiltonian in Eq. (3) in the case that the moiré potentials arise completely from a single 2D spinless coirrep. We first note that the Hamiltonian is invariant under $\varphi \mapsto \varphi + \pi$ so that for the purpose of computing a phase diagram we can take $\varphi \in [0, \pi)$. Similarly, the transformation $v_0 \mapsto iv_0$, $v_x \mapsto iv_x$ is equivalent to conjugation by $\sigma_z \otimes \sigma_0$ so we can take v_0 and v_x to be real. Additionally, $\phi_1 \mapsto \phi_1 + \pi$ is equivalent to $\varphi \mapsto -\varphi$. Since we assume $\delta\theta = 0$ for the phase diagram, we can take $\delta\epsilon < 0$ and $\phi_1 = 0$. Finally, $E_0 \mapsto -E_0$ is equivalent to $\varphi \mapsto -\varphi$, conjugation by
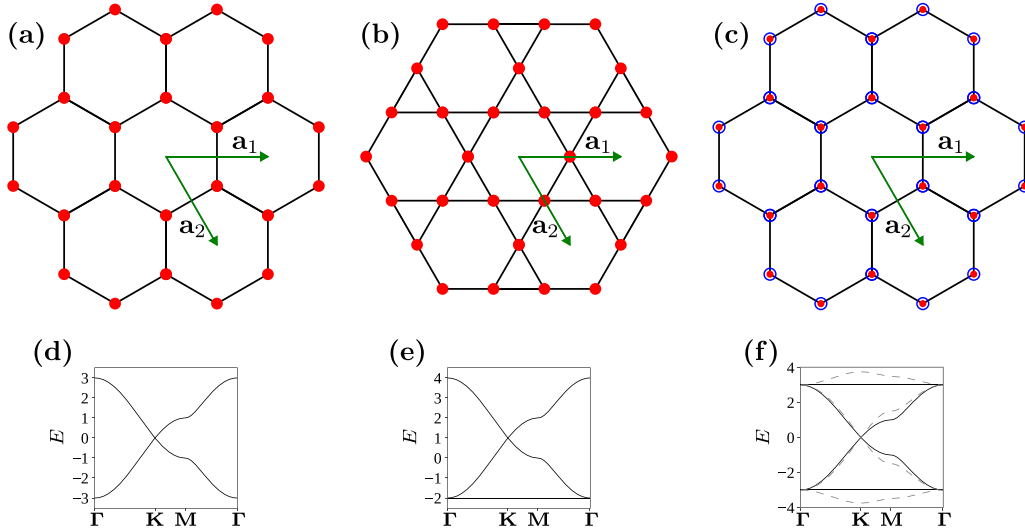
FIG. 7. [(a)–(c)] Illustrations of the tight-binding models in Appendix K. [(d)–(f)] Corresponding example band structures. (a) The honeycomb lattice one-orbital model described in Appendix K 1. (b) The kagome lattice one-orbital model described in Appendix K 2. (c) The honeycomb lattice two-orbital model described in Appendix K 3. (d) Band structure for the Hamiltonian in Eq. (K4) with $s = 0$, $t = 1$. (e) Band structure for the Hamiltonian in Eq. (K8) with $s = 0$, $t = 1$. (f) Band structures for the Hamiltonian in Eq. (K11) with $s = 0$, $t_0 = 1$. In solid black lines we have $t_x = 1$ and in dashed gray lines we have $t_x = 1.25$.

$\sigma_0 \otimes \sigma_z$, and an overall sign change. As a result, we are free to choose $E_0 < 0$.

APPENDIX K: KAGOME AND HONEYCOMB TIGHT-BINDING MODELS

In the following subsections we review three tight-binding models on kagome and honeycomb lattices. We denote the Bravais lattice, reciprocal lattice, and Brillouin zone for each model by L, P, and BZ, respectively. The primitive vectors of L are $\mathbf{a}_1$ and $\mathbf{a}_2$ as given in Eq. (B1) and illustrated in Figs. 7(a)–7(c). The primitive vectors for P are $\mathbf{b}_1$ and $\mathbf{b}_2$ as given in Eq. (B2) and the high-symmetry momenta are

$$\mathbf{\Gamma} = 0, \quad \mathbf{K} = \tfrac{2}{3}\mathbf{b}_1 + \tfrac{1}{3}\mathbf{b}_2, \quad \mathbf{M} = \tfrac{1}{2}\mathbf{b}_1 + \tfrac{1}{2}\mathbf{b}_2. \quad (K1)$$

1. Honeycomb lattice one-orbital model

We first consider a tight-binding model with a single spinless Wannier function on each site of a honeycomb lattice. The Wannier centers and nearest-neighbor bonds are shown in Fig. 7(a) with red circles and black lines, respectively. The Wannier functions are all related by isometries to a single exponentially localized orbital, which carries some 1D spinless coirrep $\rho \in \{A_1, A_2\}$ of $3m1'$ (see Appendix I and Table III). The Wannier functions together transform under the induced corepresentation $(\rho)_{2b}$ of the magnetic space group $P6mm1'$ (No. 183.186 in the BNS setting [30]), which we now describe.

The lattice sites have positions $\mathbf{r} + \alpha\boldsymbol{\tau}$ where $\mathbf{r} \in L$, $\alpha \in \{+, -\}$, and $\boldsymbol{\tau} = \frac{1}{\sqrt{3}}R_{\pi/2}\mathbf{a}_1$. We denote the Wannier function at position $\mathbf{r} + \alpha\boldsymbol{\tau}$ by $|\mathbf{r}, \alpha\rangle$ and define Bloch states

$$|\mathbf{k}, \alpha\rangle = \frac{1}{\sqrt{|\mathrm{BZ}|}} \sum_{\mathbf{r} \in L} e^{i\mathbf{k}\cdot(\mathbf{r}+\alpha\boldsymbol{\tau})}|\mathbf{r}, \alpha\rangle. \quad (K2)$$

Using coset representatives $T_{\mathbf{r}}$ and $T_{\mathbf{r}}C_{2z}$ where $T_{\mathbf{r}}$ denotes translation by $\mathbf{r} \in L$, the induced corepresentation $(\rho)_{2b}$ is determined by

$$T_{\mathbf{r}}|\mathbf{k}, \alpha\rangle = e^{-i\mathbf{k}\cdot\mathbf{r}}|\mathbf{k}, \alpha\rangle,$$
$$C_{3z}|\mathbf{k}, \alpha\rangle = |R_{2\pi/3}\mathbf{k}, \alpha\rangle,$$
$$C_{2z}|\mathbf{k}, \alpha\rangle = |-\mathbf{k}, -\alpha\rangle,$$
$$M_x|\mathbf{k}, \alpha\rangle = \mathrm{tr}(\rho(M_x))|\mathcal{R}_{\hat{\mathbf{x}}}\mathbf{k}, \alpha\rangle,$$
$$M_y|\mathbf{k}, \alpha\rangle = \mathrm{tr}(\rho(M_x))|\mathcal{R}_{\hat{\mathbf{y}}}\mathbf{k}, -\alpha\rangle,$$
$$\mathcal{T}|\mathbf{k}, \alpha\rangle = |-\mathbf{k}, \alpha\rangle. \quad (K3)$$

According to the Bilbao Crystallographic Server [43,44], $(\rho)_{2b}$ is always an elementary band representation [45].

If the Hamiltonian H for this system commutes with $(\rho)_{2b}$ and has at most nearest-neighbor hopping, then H takes the form

$$H|\mathbf{k}, \alpha\rangle = s|\mathbf{k}, \alpha\rangle + t\sum_{j=1}^{3} e^{-i\alpha\mathbf{k}\cdot R_{\zeta_j}\boldsymbol{\tau}}|\mathbf{k}, -\alpha\rangle \quad (K4)$$

for real parameters s and t, where $\zeta_j = \frac{2\pi}{3}(j - 1)$. Figure 7(d) shows the band structure for the Hamiltonian in Eq. (K4) with $s = 0$ and $t = 1$. The band structure has two dispersive bands with at Dirac cone at $\mathbf{K}$, van Hove singularities at $\mathbf{M}$, and extrema at $\mathbf{\Gamma}$. The spectrum is symmetric about s because $H - s$ anticommutes with the chiral symmetry operator

$$C|\mathbf{k}, \alpha\rangle = \alpha|\mathbf{k}, \alpha\rangle. \quad (K5)$$

2. Kagome lattice one-orbital model

We next consider a tight-binding model with a single spinless Wannier function on each site of a kagome lattice. The Wannier centers and nearest-neighbor bonds are shown in Fig. 7(b) with red circles and black lines, respectively. The Wannier functions are all related by isometries to a single

exponentially localized orbital, which carries some spinless coirrep $\rho \in \{A_1, A_2, B_1, B_2\}$ of $mm21'$ (see Appendix I and Table III). The Wannier functions together transform under the induced corepresentation $(\rho)_{3c}$ of $P6mm1'$, which we now describe.

The lattice sites have positions $\mathbf{r} + \boldsymbol{\tau}_j$ where $\mathbf{r} \in L$, $j \in \{1, 2, 3\}$, $\boldsymbol{\tau}_j = \frac{1}{2}R_{\zeta_j}\mathbf{a}_1$, and $\zeta_j = \frac{2\pi}{3}(j-1)$. We denote the Wannier function at position $\mathbf{r} + \boldsymbol{\tau}_j$ by $|\mathbf{r}, j\rangle$ and define Bloch states

$$|\mathbf{k}, j\rangle = \frac{1}{\sqrt{|\mathrm{BZ}|}} \sum_{\mathbf{r} \in L} e^{i\mathbf{k} \cdot (\mathbf{r} + \boldsymbol{\tau}_j)} |\mathbf{r}, j\rangle. \quad (K6)$$

Using coset representatives $T_\mathbf{r}$, $T_\mathbf{r}C_{3z}$, and $T_\mathbf{r}C_{3z}^{-1}$ where $T_\mathbf{r}$ denotes translation by $\mathbf{r} \in L$, the induced corepresentation $(\rho)_{3c}$ is determined by

$$
\begin{aligned}
T_\mathbf{r}|\mathbf{k}, j\rangle &= e^{-i\mathbf{k}\cdot\mathbf{r}}|\mathbf{k}, j\rangle, \\
C_{3z}|\mathbf{k}, j\rangle &= |R_{2\pi/3}\mathbf{k}, j+1\rangle, \\
C_{2z}|\mathbf{k}, j\rangle &= \mathrm{tr}(\rho(C_{2z}))|-\mathbf{k}, j\rangle, \\
M_x|\mathbf{k}, j\rangle &= \mathrm{tr}(\rho(M_x))|\mathcal{R}_{\hat{\mathbf{x}}}\mathbf{k}, 2-j\rangle, \\
M_y|\mathbf{k}, j\rangle &= \mathrm{tr}(\rho(M_y))|\mathcal{R}_{\hat{\mathbf{y}}}\mathbf{k}, 2-j\rangle, \\
\mathcal{T}|\mathbf{k}, j\rangle &= |-\mathbf{k}, j\rangle,
\end{aligned}
\quad (K7)
$$

where the j indices are cyclic modulo 3. According to the Bilbao Crystallographic Server [43,44], $(\rho)_{3c}$ is always an elementary band representation [45].

If the Hamiltonian H for this system commutes with $(\rho)_{3c}$ and has at most nearest-neighbor hopping, then H takes the form

$$
\begin{aligned}
H|\mathbf{k}, j\rangle = s|\mathbf{k}, j\rangle &+ 2t\cos(\mathbf{k}\cdot\boldsymbol{\tau}_{j-1})|\mathbf{k}, j+1\rangle \\
&+ 2t\cos(\mathbf{k}\cdot\boldsymbol{\tau}_{j+1})|\mathbf{k}, j-1\rangle
\end{aligned}
\quad (K8)
$$

for real parameters s and t. Figure 7(e) shows the band structure for the Hamiltonian in Eq. (K8) with $s = 0$ and $t = 1$. The band structure has two dispersive bands with at Dirac cone at $\mathbf{K}$, van Hove singularities at $\mathbf{M}$, and extrema at $\boldsymbol{\Gamma}$. Additionally, there is a flat band that has a quadratic touching with a dispersive band at $\boldsymbol{\Gamma}$. We prove in Appendix L 2 that the Hamiltonian in Eq. (K8) has a perfectly flat band with energy $s - 2t$.

3. Honeycomb lattice two-orbital model

Finally, we consider a tight-binding model with two spinless Wannier functions on each site of a honeycomb lattice. The Wannier centers and nearest-neighbor bonds are shown in Fig. 7(c) with red and blue circles and black lines, respectively. The Wannier functions are all related by isometries to a pair of exponentially localized orbitals, which transform under coirrep E of $3m1'$ (see Appendix I and Table III). The Wannier functions together transform under the induced corepresentation $(E)_{2b}$ of $P6mm1'$, which we now describe.

The lattice sites have positions $\mathbf{r} + \alpha\boldsymbol{\tau}$ where $\mathbf{r} \in L$, $\alpha \in \{+, -\}$, and $\boldsymbol{\tau} = \frac{1}{\sqrt{3}}R_{\pi/2}\mathbf{a}_1$. We denote the two Wannier functions at position $\mathbf{r} + \alpha\boldsymbol{\tau}$ by $|\mathbf{r}, \alpha, \ell\rangle$ where $\ell \in \{+, -\}$ labels

the two orbitals, and we define Bloch states

$$|\mathbf{k}, \alpha, \ell\rangle = \frac{1}{\sqrt{|\mathrm{BZ}|}} \sum_{\mathbf{r} \in L} e^{i\mathbf{k} \cdot (\mathbf{r} + \alpha\boldsymbol{\tau})} |\mathbf{r}, \alpha, \ell\rangle. \quad (K9)$$

For convenience, we choose the two orbitals so that C_{3z}, M_x, and $\mathcal{T}$ are represented by $e^{-i(2\pi/3)\sigma_z}$, $-\sigma_x$, and $\sigma_x\mathcal{K}$, respectively, where $\mathcal{K}$ denotes complex conjugation. This symmetry condition is satisfied, for example, by atomic orbitals $p_x + i\ell p_y$. Using coset representatives $T_\mathbf{r}$ and $T_\mathbf{r}C_{2z}$ where $T_\mathbf{r}$ denotes translation by $\mathbf{r} \in L$, the induced corepresentation $(E)_{2b}$ is determined by

$$
\begin{aligned}
T_\mathbf{r}|\mathbf{k}, \alpha, \ell\rangle &= e^{-i\mathbf{k}\cdot\mathbf{r}}|\mathbf{k}, \alpha, \ell\rangle, \\
C_{3z}|\mathbf{k}, \alpha, \ell\rangle &= e^{-i(2\pi/3)\ell}|R_{2\pi/3}\mathbf{k}, \alpha, \ell\rangle, \\
C_{2z}|\mathbf{k}, \alpha, \ell\rangle &= |-\mathbf{k}, -\alpha, \ell\rangle, \\
M_x|\mathbf{k}, \alpha, \ell\rangle &= -|\mathcal{R}_{\hat{\mathbf{x}}}\mathbf{k}, \alpha, -\ell\rangle, \\
M_y|\mathbf{k}, \alpha, \ell\rangle &= -|\mathcal{R}_{\hat{\mathbf{y}}}\mathbf{k}, -\alpha, -\ell\rangle, \\
\mathcal{T}|\mathbf{k}, \alpha, \ell\rangle &= |-\mathbf{k}, \alpha, -\ell\rangle.
\end{aligned}
\quad (K10)
$$

According to the Bilbao Crystallographic Server [43,44], $(E)_{2b}$ is an elementary band representation [45].

If the Hamiltonian H for this system commutes with $(E)_{2b}$ and has at most nearest-neighbor hopping, then H takes the form

$$
\begin{aligned}
H|\mathbf{k}, \alpha, \ell\rangle = s|\mathbf{k}, \alpha, \ell\rangle &+ \sum_{j=1}^{3} e^{-i\alpha\mathbf{k}\cdot R_{\zeta_j}\boldsymbol{\tau}}(t_0|\mathbf{k}, -\alpha, \ell\rangle \\
&+ t_x e^{-i\ell\zeta_j}|\mathbf{k}, -\alpha, -\ell\rangle)
\end{aligned}
\quad (K11)
$$

for real parameters s, t_0, and t_x, where $\zeta_j = \frac{2\pi}{3}(j-1)$. Figure 7(f) shows band structures for the Hamiltonian in Eq. (K11) with $s = 0$, $t_0 = t_x = 1$ in solid black lines and $s = 0$, $t_0 = 1$, $t_x = 1.25$ in dashed gray lines. The middle two bands in both cases are dispersive and have a Dirac cone at $\mathbf{K}$, van Hove singularities at $\mathbf{M}$, and extrema at $\boldsymbol{\Gamma}$. Additionally, the top and bottom bands have quadratic touchings with the middle two bands at $\boldsymbol{\Gamma}$. The spectrum is symmetric about s because $H - s$ anticommutes with the chiral symmetry operator

$$C|\mathbf{k}, \alpha, \ell\rangle = \alpha|\mathbf{k}, \alpha, \ell\rangle. \quad (K12)$$

When $t_0 = t_x = 1$, the top and bottom bands are flat, but when $t_0 = 1$, $t_x = 1.25$ they are dispersive. We prove in Appendix L 3 that the Hamiltonian in Eq. (K11) has two perfectly flat bands with energies $s \pm 3|t_0|$ when $|t_0| = |t_x|$.

APPENDIX L: KAGOME AND HONEYCOMB FLAT BANDS FROM BIPARTITE CRYSTALLINE LATTICES

In the following subsections we review the bipartite crystalline lattice construction of Ref. [15] and then apply it to prove the existence of flat bands in the models described in Appendices K 2 and K 3.

1. Bipartite crystalline lattice construction

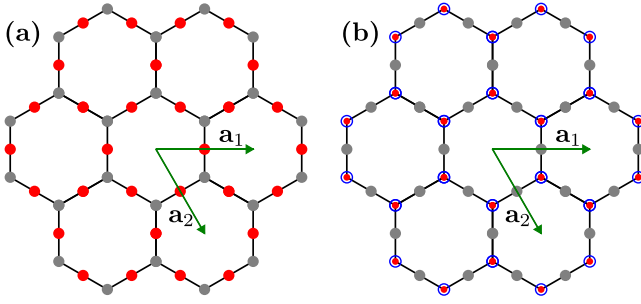As in Appendices K 1 to K 3, we consider a tight-binding model supported on Wannier functions that are formed from

FIG. 8. (a) Bipartite crystalline lattice for Appendix L 2. The $n = 1$ ($n = 2$) Wannier centers are shown with red (gray) circles. (b) Bipartite crystalline lattice for Appendix L 3. The $n = 1$ ($n = 2$) Wannier centers are shown with red and blue (gray) circles. In both diagrams, the black lines indicate nearest-neighbor hoppings.

some set of exponentially localized orbitals. We partition the orbitals into two subsets $\mathcal{O}_1$ and $\mathcal{O}_2$ and denote the Wannier functions arising from subset $\mathcal{O}_n$ by $|\mathbf{r}, n, x\rangle$ for $\mathbf{r} \in L$, $n \in \{1, 2\}$, and $1 \leqslant x \leqslant N_n$, where L is the Bravais lattice and N_n is the number of orbitals from $\mathcal{O}_n$ in each unit cell. The orbital $|\mathbf{r}, n, x\rangle$ has position $\mathbf{r} + \boldsymbol{\tau}_{n,x}$ and we define Bloch states

$$|\mathbf{k}, n, x\rangle = \frac{1}{\sqrt{|\text{BZ}|}} \sum_{\mathbf{r} \in L} e^{i\mathbf{k} \cdot (\mathbf{r} + \boldsymbol{\tau}_{n,x})} |\mathbf{r}, n, x\rangle. \quad (L1)$$

We assume the Hamiltonian H has no hoppings between Wannier functions arising from the same subset $\mathcal{O}_n$, except for a constant chemical potential μ on Wannier functions arising from $\mathcal{O}_2$. A model of this form is called a bipartite crystalline lattice [15]. We assume without loss of generality that $N_1 \geqslant N_2$. For a given crystal momentum $\mathbf{k}$, H is represented on Bloch states $|\mathbf{k}, n, x\rangle$ by the matrix

$$\mathcal{H}(\mathbf{k}) = \begin{pmatrix} 0 & \mathcal{S}(\mathbf{k}) \\ \mathcal{S}^\dagger(\mathbf{k}) & -\mu \end{pmatrix} \quad (L2)$$

for some $N_1 \times N_2$ complex matrix $\mathcal{S}(\mathbf{k})$. The first N_1 (last N_2) rows and columns of $\mathcal{H}(\mathbf{k})$ correspond to $\mathcal{O}_1$ ($\mathcal{O}_2$). By the rank-nullity theorem, the null space of $\mathcal{S}^\dagger(\mathbf{k})$ has dimension at least $N_1 - N_2$. Additionally, if v is in the null space of $\mathcal{S}^\dagger(\mathbf{k})$ then

$$\mathcal{H}(\mathbf{k}) \begin{pmatrix} v \\ 0 \end{pmatrix} = 0. \quad (L3)$$

As a result, H must have at least $N_1 - N_2$ perfectly flat bands with energy 0, which are completely supported on the Wannier functions arising from $\mathcal{O}_1$.

We next apply Schrieffer-Wolff perturbation theory [58,59] to second order in $\mathcal{S}(\mathbf{k})$ to find the low-energy Hamiltonian $\tilde{H}$ for the Wannier functions arising from $\mathcal{O}_1$. For a given crystal momentum $\mathbf{k}$, $\tilde{H}$ is represented on Bloch states $|\mathbf{k}, 1, x\rangle$ by the matrix

$$\tilde{\mathcal{H}}(\mathbf{k}) = \frac{\mathcal{S}(\mathbf{k}) \mathcal{S}^\dagger(\mathbf{k})}{\mu}. \quad (L4)$$

We now send $|\mu|, |\mathcal{S}(\mathbf{k})| \to \infty$ while fixing $\tilde{\mathcal{H}}(\mathbf{k})$. In this limit, the Schrieffer-Wolff perturbation theory at second order becomes exact. The resulting tight-binding model $\tilde{H}$ then has at least $N_1 - N_2$ perfectly flat bands with energy 0.

2. Kagome lattice one-orbital model

We take $|\mathbf{r}, 1, x\rangle$ to be the kagome lattice Wannier functions $|\mathbf{r}, j\rangle$ in Appendix K 2 so that $N_1 = 3$. Additionally, we take $|\mathbf{r}, 2, x\rangle$ to be the honeycomb lattice Wannier functions $|\mathbf{r}, \alpha\rangle$ in Appendix K 1 so that $N_2 = 2$. The Wannier functions and nearest-neighbor hoppings are illustrated in Fig. 8(a) in red ($n = 1$) and gray ($n = 2$) circles, and black lines, respectively. Since the matrix elements of the Hamiltonian in Eq. (K8) do not depend on the choice of corepresentation, we are free to choose corepresentations A_1 of $mm21'$ and A_1 of $3m1'$ to induce the corepresentations of $P6mm1'$, without loss of generality. The full set of Wannier functions transforms under the direct sum of the two induced corepresentations.

If the Hamiltonian H for this system commutes with the direct sum corepresentation, satisfies the requirements in Appendix L 1, and has at most first-order hoppings, then we must have

$$H|\mathbf{k}, j\rangle = \tilde{t} \sum_{\alpha = \pm} e^{i\mathbf{k} \cdot \boldsymbol{\tau}_{j,\alpha}} |\mathbf{k}, \alpha\rangle,$$

$$H|\mathbf{k}, \alpha\rangle = -\mu|\mathbf{k}, \alpha\rangle + \tilde{t} \sum_{j=1}^{3} e^{-i\mathbf{k} \cdot \boldsymbol{\tau}_{j,\alpha}} |\mathbf{k}, j\rangle \quad (L5)$$

for a real parameter $\tilde{t}$, where

$$\boldsymbol{\tau}_{j,\alpha} = \frac{\alpha}{2\sqrt{3}} R_{\zeta_j + \pi/2} \mathbf{a}_1 \quad (L6)$$

with $\zeta_j = \frac{2\pi}{3}(j - 1)$. If we take $\mu = \tilde{t}^2/t$ for some fixed real value t and then send $\tilde{t} \to \infty$, the low-energy Hamiltonian $\tilde{H}$ described in Appendix L 1 takes the form of Eq. (K8) with $s = 2t$. Since $\tilde{H}$ has $N_1 - N_2 = 1$ perfectly flat band with energy 0 for any $t \in \mathbb{R}$, we conclude that the Hamiltonian in Eq. (K8) always has a perfectly flat band with energy $s - 2t$.

3. Honeycomb lattice two-orbital model

Next, we take $|\mathbf{r}, 1, x\rangle$ to be the honeycomb lattice Wannier functions $|\mathbf{r}, \alpha, \ell\rangle$ in Appendix K 3 so that $N_1 = 4$. Additionally, we take $|\mathbf{r}, 2, x\rangle$ to be the kagome lattice Wannier functions $|\mathbf{r}, j\rangle$ in Appendix K 2 so that $N_2 = 3$. The Wannier functions and nearest-neighbor hoppings are illustrated in Fig. 8(b) in red and blue ($n = 1$) and gray ($n = 2$) circles, and black lines, respectively. We choose corepresentations E of $3m1'$ and $\rho \in \{A_1, A_2, B_1, B_2\}$ of $mm21'$ to induce the corepresentations of $P6mm1'$. The full set of Wannier functions transforms under the direct sum of the two induced corepresentations.

If the Hamiltonian H for this system commutes with the direct sum corepresentation, satisfies the requirements in Appendix L 1, and has at most first-order hoppings, then we must have

$$H|\mathbf{k}, \alpha, \ell\rangle = \tilde{t}^* \sum_{j=1}^{3} e^{-i\mathbf{k} \cdot \boldsymbol{\tau}_{j,\alpha}} e^{i\ell \zeta_j} \alpha^{\nu_1} \ell^{\nu_2} |\mathbf{k}, j\rangle,$$

$$H|\mathbf{k}, j\rangle = -\mu|\mathbf{k}, j\rangle + \tilde{t} \sum_{\alpha = \pm} \sum_{\ell = \pm} e^{i\mathbf{k} \cdot \boldsymbol{\tau}_{j,\alpha}} e^{-i\ell \zeta_j} \alpha^{\nu_1} \ell^{\nu_2} |\mathbf{k}, \alpha, \ell\rangle$$

$$(L7)$$

for a real or imaginary parameter $\tilde{t}$, where

$$
\begin{aligned}
\tilde{t} \in \mathbb{R}, \; \nu_1 = 0, \; \nu_2 = 0 \quad &\text{when } \rho = A_2 \\
\tilde{t} \in i\mathbb{R}, \; \nu_1 = 0, \; \nu_2 = 1 \quad &\text{when } \rho = A_1 \\
\tilde{t} \in \mathbb{R}, \; \nu_1 = 1, \; \nu_2 = 0 \quad &\text{when } \rho = B_1 \\
\tilde{t} \in i\mathbb{R}, \; \nu_1 = 1, \; \nu_2 = 1 \quad &\text{when } \rho = B_2
\end{aligned} \tag{L8}
$$

(see Table III), $\tau_{\alpha, j}$ is given by Eq. (L6), and $\zeta_j = \frac{2\pi}{3}(j-1)$. If we take $\mu = |\tilde{t}|^2/t$ for some fixed real value t and then send $|\tilde{t}| \to \infty$, the low-energy Hamiltonian $\tilde{H}$ described in Appendix L 1 takes the form of Eq. (K11) with $s = 3t$, $t_0 = (-1)^{\nu_1} t$, $t_x = (-1)^{\nu_1 + \nu_2} t$. Since $\tilde{H}$ has a perfectly flat band with energy 0 for any $t \in \mathbb{R}$ and $\nu_1, \nu_2 \in \{0, 1\}$, we conclude that the Hamiltonian in Eq. (K11) has two perfectly flat bands with energies $s \pm 3|t_0|$ when $|t_0| = |t_x|$.

[1] R. Bistritzer and A. H. MacDonald, Moiré bands in twisted double-layer graphene, Proc. Natl. Acad. Sci. USA **108**, 12233 (2011).

[2] H. C. Po, L. Zou, T. Senthil, and A. Vishwanath, Faithful tight-binding models and fragile topology of magic-angle bilayer graphene, Phys. Rev. B **99**, 195455 (2019).

[3] J. Ahn, S. Park, and B. J. Yang, Failure of Nielsen-Ninomiya theorem and fragile topology in two-dimensional systems with space-time inversion symmetry: Application to twisted bilayer graphene at magic angle, Phys. Rev. X **9**, 021013 (2019).

[4] Z. Song, Z. Wang, W. Shi, G. Li, C. Fang, and B. A. Bernevig, All magic angles in twisted bilayer graphene are topological, Phys. Rev. Lett. **123**, 036401 (2019).

[5] Z.-D. Song, B. Lian, N. Regnault, and B. A. Bernevig, Twisted bilayer graphene. II. Stable symmetry anomaly, Phys. Rev. B **103**, 205412 (2021).

[6] Y. Cao, V. Fatemi, S. Fang, K. Watanabe, T. Taniguchi, E. Kaxiras, and P. Jarillo-Herrero, Unconventional superconductivity in magic-angle graphene superlattices, Nature (London) **556**, 43 (2018).

[7] Y. Cao, V. Fatemi, A. Demir, S. Fang, S. L. Tomarken, J. Y. Luo, J. D. Sanchez-Yamagishi, K. Watanabe, T. Taniguchi, E. Kaxiras *et al.*, Correlated insulator behaviour at half-filling in magic-angle graphene superlattices, Nature (London) **556**, 80 (2018).

[8] M. Yankowitz, S. Chen, H. Polshyn, Y. Zhang, K. Watanabe, T. Taniguchi, D. Graf, A. F. Young, and C. R. Dean, Tuning superconductivity in twisted bilayer graphene, Science **363**, 1059 (2019).

[9] A. L. Sharpe, E. J. Fox, A. W. Barnard, J. Finney, K. Watanabe, T. Taniguchi, M. A. Kastner, and D. Goldhaber-Gordon, Emergent ferromagnetism near three-quarters filling in twisted bilayer graphene, Science **365**, 605 (2019).

[10] Y. Xie, B. Lian, B. Jäck, X. Liu, C. L. Chiu, K. Watanabe, T. Taniguchi, B. A. Bernevig, and A. Yazdani, Spectroscopic signatures of many-body correlations in magic-angle twisted bilayer graphene, Nature (London) **572**, 101 (2019).

[11] X. Lu, P. Stepanov, W. Yang, M. Xie, M. A. Aamir, I. Das, C. Urgell, K. Watanabe, T. Taniguchi, G. Zhang, A. Bachtold *et al.*, Superconductors, orbital magnets and correlated states in magic-angle bilayer graphene, Nature (London) **574**, 653 (2019).

[12] M. Serlin, C. L. Tschirhart, H. Polshyn, Y. Zhang, J. Zhu, K. Watanabe, T. Taniguchi, L. Balents, and A. F. Young, Intrinsic quantized anomalous Hall effect in a moiré heterostructure, Science **367**, 900 (2020).

[13] E. H. Lieb, Two theorems on the Hubbard model, Phys. Rev. Lett. **62**, 1201 (1989).

[14] A. Mielke, Ferromagnetic ground states for the Hubbard model on line graphs, J. Phys. A: Math. Gen. **24**, L73 (1991).

[15] D. Călugăru, A. Chew, L. Elcoro, Y. Xu, N. Regnault, Z. D. Song, and B. A. Bernevig, General construction and topological classification of crystalline flat bands, Nat. Phys. **18**, 185 (2022).

[16] D. L. Bergman, C. Wu, and L. Balents, Band touching from real-space topology in frustrated hopping models, Phys. Rev. B **78**, 125104 (2008).

[17] G. Xu, B. Lian, and S. C. Zhang, Intrinsic quantum anomalous Hall effect in the kagome lattice $Cs_2LiMn_3F_{12}$, Phys. Rev. Lett. **115**, 186802 (2015).

[18] S. Yan, D. A. Huse, and S. R. White, Spin-liquid ground state of the $S = 1/2$ kagome Heisenberg antiferromagnet, Science **332**, 1173 (2011).

[19] J. X. Yin, B. Lian, and M. Z. Hasan, Topological kagome magnets and superconductors, Nature (London) **612**, 647 (2022).

[20] C. Wu, D. Bergman, L. Balents, and S. Das Sarma, Flat bands and Wigner crystallization in the honeycomb optical lattice, Phys. Rev. Lett. **99**, 070401 (2007).

[21] H. Liu, S. Meng, and F. Liu, Screening two-dimensional materials with topological flat bands, Phys. Rev. Mater. **5**, 084203 (2021).

[22] N. Regnault, Y. Xu, M. R. Li, D. S. Ma, M. Jovanovic, A. Yazdani, S. S. Parkin, C. Felser, L. M. Schoop, N. P. Ong, R. J. Cava, L. Elcoro, Z. D. Song, and B. A. Bernevig, Catalogue of flat-band stoichiometric materials, Nature (London) **603**, 824 (2022).

[23] M. Jovanovic and L. M. Schoop, Simple chemical rules for predicting band structures of kagome materials, J. Am. Chem. Soc. **144**, 10978 (2022).

[24] A. Kokalj, XCrySDen-a new program for displaying crystalline structures and electron densities, J. Mol. Graphics Modell. **17**, 176 (1999).

[25] M. Angeli and A. H. MacDonald, Γ valley transition metal dichalcogenide moiré bands, Proc. Natl. Acad. Sci. USA **118**, e2021826118 (2021).

[26] L. Xian, M. Claassen, D. Kiese, M. M. Scherer, S. Trebst, D. M. Kennes, and A. Rubio, Realization of nearly dispersionless bands with strong orbital anisotropy from destructive interference in twisted bilayer MoS_2, Nat. Commun. **12**, 5644 (2021).

[27] Z. Liu, H. Wang, and J. Wang, Magnetic moiré surface states and flat Chern bands in topological insulators, Phys. Rev. B **106**, 035114 (2022).

[28] H. Wang, Y. Jiang, Z. Liu, and J. Wang, Moiré engineering and topological flat bands in twisted orbital-active bilayers, arXiv:2209.06524.

[29] D. Pei, B. Wang, Z. Zhou, Z. He, L. An, S. He, C. Chen, Y. Li, L. Wei, A. Liang, J. Avila, P. Dudin, V. Kandyba, A. Giampietri, M. Cattelan, A. Barinov, Z. Liu, J. Liu, H. Weng, N. Wang *et al.*, Observation of Γ -valley Mmoiré bands and emergent hexagonal lattice in twisted transition metal dichalcogenides, Phys. Rev. X **12**, 021065 (2022).

[30] S. V. Gallego, E. S. Tasci, G. de la Flor, J. M. Perez-Mato, and M. I. Aroyo, Magnetic symmetry in the Bilbao Crystallographic Server: A computer program to provide systematic absences of magnetic neutron diffraction, J. Appl. Crystallogr. **45**, 1236 (2012).

[31] J. D. Newmarch and R. M. Golding, The character table for the corepresentations of magnetic groups, J. Math. Phys. **23**, 695 (1982).

[32] Z. D. Song, L. Elcoro, and B. Andrei Bernevig, Twisted bulk-boundary correspondence of fragile topology, Science **367**, 794 (2020).

[33] C. L. Kane and E. J. Mele, Z_2 topological order and the quantum spin Hall effect, Phys. Rev. Lett. **95**, 146802 (2005).

[34] B. A. Bernevig, T. L. Hughes, and S. C. Zhang, Quantum spin Hall effect and topological phase transition in HgTe quantum wells, Science **314**, 1757 (2006).

[35] Y. Cai, C. P. Chuu, C. M. Wei, and M. Y. Chou, Stability and electronic properties of two-dimensional silicene and germanene on graphene, Phys. Rev. B **88**, 245408 (2013).

[36] M. A. B. Hamid, K. T. Chan, C. H. Raymond Ooi, H. Zainuddin, N. Mohd Shah, and N. N. Shahrol Nidzam, Structural stability and electronic properties of graphene/germanene heterobilayer, Results Phys. **28**, 104545 (2021).

[37] J. R. Wallbank, M. Mucha-Kruczyński, and V. I. Fal'Ko, Moiré minibands in graphene heterostructures with almost commensurate $\sqrt{3} \times \sqrt{3}$ hexagonal crystals, Phys. Rev. B **88**, 155415 (2013).

[38] A. Dunbrack and J. Cano, Magic angle conditions for twisted three-dimensional topological insulators, Phys. Rev. B **106**, 075142 (2022).

[39] Q. Lu, C. Le, X. Zhang, J. Cook, X. He, M. Zarenia, M. Vaninger, P. F. Miceli, D. J. Singh, C. Liu *et al.*, Dirac fermion cloning, moiré flat bands, and magic lattice constants in epitaxial monolayer graphene, Adv. Mater. **34**, 2200625 (2022).

[40] C. Wu, Q. Wan, C. Peng, S. Mo, R. Li, K. Zhao, Y. Guo, S. Yuan, F. Wu, C. Zhang, and N. Xu, Tailoring Dirac fermions by *in-situ* tunable high-order moiré pattern in graphene-monolayer xenon heterostructure, Phys. Rev. Lett. **129**, 176402 (2022).

[41] M. G. Scheer, K. Gu, and B. Lian, Magic angles in twisted bilayer graphene near commensuration: Towards a hypermagic regime, Phys. Rev. B **106**, 115418 (2022).

[42] These commensurate configurations are fully classified in Appendix C, and Table II lists the first 28 of them. Additionally, Appendix D discusses the form for moiré models near arbitrary commensurate configurations.

[43] L. Elcoro, B. J. Wieder, Z. Song, Y. Xu, B. Bradlyn, and B. A. Bernevig, Magnetic topological quantum chemistry, Nat. Commun. **12**, 5965 (2021).

[44] Y. Xu, L. Elcoro, Z. D. Song, B. J. Wieder, M. G. Vergniory, N. Regnault, Y. Chen, C. Felser, and B. A. Bernevig, High-

[45] throughput calculations of magnetic topological materials, Nature (London) **586**, 702 (2020).

[45] B. Bradlyn, L. Elcoro, J. Cano, M. G. Vergniory, Z. Wang, C. Felser, M. I. Aroyo, and B. A. Bernevig, Topological quantum chemistry, Nature (London) **547**, 298 (2017).

[46] If more than one minimal set of bands exists, we choose the set containing the fewest number of conduction bands.

[47] J. Kruthoff, J. De Boer, J. Van Wezel, C. L. Kane, and R. J. Slager, Topological classification of crystalline insulators through band structure combinatorics, Phys. Rev. X **7**, 041069 (2017).

[48] H. C. Po, H. Watanabe, and A. Vishwanath, Fragile topology and Wannier obstructions, Phys. Rev. Lett. **121**, 126402 (2018).

[49] A. Bouhon, A. M. Black-Schaffer, and R. J. Slager, Wilson loop approach to fragile topology of split elementary band representations and topological crystalline insulators with time-reversal symmetry, Phys. Rev. B **100**, 195135 (2019).

[50] The low-energy band structure is neither guaranteed to be connected nor isolated. For example, in Fig. 3(c) they are isolated but not connected, while in Fig. 5(e) they are connected but not isolated.

[51] Z. D. Song, L. Elcoro, Y. F. Xu, N. Regnault, and B. A. Bernevig, Fragile phases as affine monoids: Classification and material examples, Phys. Rev. X **10**, 031001 (2020).

[52] Although the sign of the Dirac Fermi velocity is basis dependent, it is well defined in the presence of a fixed form for the symmetry operators.

[53] E. Khalaf, A. J. Kruchkov, G. Tarnopolsky, and A. Vishwanath, Magic angle hierarchy in twisted graphene multilayers, Phys. Rev. B **100**, 085109 (2019).

[54] D. Călugăru, F. Xie, Z. D. Song, B. Lian, N. Regnault, and B. A. Bernevig, Twisted symmetric trilayer graphene: Single-particle and many-body Hamiltonians and hidden nonlocal symmetries of trilayer moiré systems with and without displacement field, Phys. Rev. B **103**, 195411 (2021).

[55] Z. Wu and Y. Zheng, Moiré metamaterials and metasurfaces, Adv. Opt. Mater. **6**, 1701057 (2018).

[56] J. C. Slater and G. F. Koster, Simplified LCAO method for the periodic potential problem, Phys. Rev. **94**, 1498 (1954).

[57] A. H. Castro Neto, F. Guinea, N. M. R. Peres, K. S. Novoselov, and A. K. Geim, The electronic properties of graphene, Rev. Mod. Phys. **81**, 109 (2009).

[58] J. R. Schrieffer and P. A. Wolff, Relation between the Anderson and Kondo Hamiltonians, Phys. Rev. **149**, 491 (1966).

[59] S. Bravyi, D. P. DiVincenzo, and D. Loss, Schrieffer-Wolff transformation for quantum many-body systems, Ann. Phys. **326**, 2793 (2011).

[60] M. I. Aroyo, J. M. Perez-Mato, C. Capillas, E. Kroumova, S. Ivantchev, G. Madariaga, A. Kirov, and H. Wondratschek, Bilbao Crystallographic Server: I. Databases and crystallographic computing programs, Z. Kristallographie - Cryst. Mater. **221**, 15 (2006).

[61] M. I. Aroyo, A. Kirov, C. Capillas, J. M. Perez-Mato, and H. Wondratschek, Bilbao Crystallographic Server. II. Representations of crystallographic point groups and space groups, Acta Crystallogr. A: Found Cryst. **62**, 115 (2006).